

Article

Exploring the Integration of Architectural Design and Advanced Structural Analysis for Steel–Glass Structures: A Comparative Study of Different Case Scenarios

Faham Tahmasebinia ^{1,*} , Shaoxiong Jiang ¹ , Sara Shirowzhan ² , Lewis Mann ¹ and Samad M. E. Sepasgozar ² 

¹ School of Civil Engineering, The University of Sydney, Sydney, NSW 2008, Australia; sjia6722@uni.sydney.edu.au (S.J.)

² School of Built Environment, The University of New South Wales, Sydney, NSW 2052, Australia; s.shirowzhan@unsw.edu.au (S.S.)

* Correspondence: faham.tahmasebinia@sydney.edu.au

Abstract: It is well known that finite element analysis (FEA) is a powerful tool when it comes to the design and analysis of complex structures for various load combinations, including light steel curve members. This abstract provides an overview of the FEA simulation process for designing such members (curve members), which involves constructing a 3D model, discretising the member into small elements, assigning material properties, defining boundary conditions, conducting the simulation, analysing the results, and making any necessary modifications to the design. FEA simulations can provide valuable insights into the behaviour of light steel curved members under different load combinations. This enables designers to optimise designs for strength, safety, and cost-effectiveness. This article proposes using two commercial 3D software programs, Rhino 7 and Strand7, to complete the FEA simulation of light steel curved members. The 3D model is created in Rhino 7, and the individual elements are discretised into more minor elements using Strand7 for assigning material properties, defining boundary conditions, running simulations, and analysing the results. The paper presents five case studies of steel–glass façades and applies the proposed methodology to each. Examples include Phoenix International Media Center in Beijing, Kazakhstan Pavilion and Science Museum in Astana, Moynihan Train Hall in New York City, Chadstone Shopping Centre in Melbourne, and the central light rail station in The Hague.

Keywords: steel-glass structures; curved steel members; elastic buckling behaviour of curved members; global structural performance; parametric design; CAD modelling



Citation: Tahmasebinia, F.; Jiang, S.; Shirowzhan, S.; Mann, L.; Sepasgozar, S.M.E. Exploring the Integration of Architectural Design and Advanced Structural Analysis for Steel–Glass Structures: A Comparative Study of Different Case Scenarios. *Buildings* **2023**, *13*, 1369. <https://doi.org/10.3390/buildings13061369>

Academic Editors: Bo Yang, Shan Gao, Hai-Ting Li and Kang Chen

Received: 4 April 2023
Revised: 9 May 2023
Accepted: 16 May 2023
Published: 23 May 2023



Copyright: © 2023 by the authors. Licensee MDPI, Basel, Switzerland. This article is an open access article distributed under the terms and conditions of the Creative Commons Attribution (CC BY) license (<https://creativecommons.org/licenses/by/4.0/>).

1. Introduction

1.1. Steel–Glass Structure

Steel and glass have become increasingly prevalent in architecture due to advancements in design concepts and construction technology. In recent decades, there has been a growing body of research on steel–glass structures, resulting in a significant increase in literature on the topic. With improved material properties, steel and glass have demonstrated excellent mechanical performance, surpassing previous expectations regarding their resistance to buckling and breaking. Steel and glass are often combined for their aesthetic and structural value, particularly in steel–glass façades. In this type of construction, the structural frame is typically made of either steel or aluminium, with glass panels serving as the cladding material [1]. The steel frame is erected first, forming the required shape, and then the glass panels are carefully fitted and connected to the frame using a specific process. The resulting steel–glass structure can replace concrete walls and roofs, offering cost reduction, improved indoor illumination, and enhanced aesthetic appeal.

1.2. Advantageous of Steel–Glass Structures

1.2.1. Cost

Despite its ability to improve indoor illumination and create a distinctive spatial experience, the steel–glass grid shell structure is expensive. Unfortunately, no comprehensive cost comparison has been conducted between brick, timber, concrete, steel, and steel–glass buildings. The practice experience in the industry and relevant feasibility studies are valuable sources of information.

Compared with traditional structures, steel–glass structures are potentially more expensive, but require little maintenance. The glass panels can be cleaned easily, and the steel beams can be prevented from corroding by painting and coating. Further, a complex curved steel–glass façade can be used where both straight and curved steel members can be used. Admittedly, straight members have relatively low prices compared to curved steel structures and are easier to manufacture. The additional cost caused by the curved steel members is minimal compared to the cost of the entire steelwork. Moreover, the extra expenditure can be offset by reduced ridge detail and flashing costs for structure spans less than 25 m [2]. Additionally, the cost of the steel–glass construction can be further minimised by utilising advanced form-finding and structure analysis techniques.

1.2.2. Sustainability

By improving indoor illumination and regulating temperature, steel–glass structures can contribute to energy efficiency. Undoubtedly, the steel–glass structure can improve the quality of indoor lighting. Glass is a material with high transmittance and transparency that allows sunlight access. While the steel structure is the main supporting part, its size is smaller than the glass part. Since traditional buildings are mostly brick, timber, and concrete structures, sunlight can only be accessed through windows and skylights. A glass panel with insulation capacity may also be incorporated into the design, facilitating the control of the building's heating and cooling.

1.2.3. Aesthetic Value

Steel–glass structures can improve the aesthetics of a building. Architects can convey their design concepts with another level of flexibility through structural design. Thus, irregular-shaped structures need to be considered in structural design processes. For irregular-shaped steel–glass structural design, curved members are often used instead of straight members. They are more reliable due to the efficiency of arches and other vertically curved structures [3]. Moreover, in some scenarios, the straight steel members may not be appropriate, and only curved structural members can be used. Moreover, steel–glass structures can provide flexibility in the architectural design process. As a result, it can create a larger open space and satisfy the specific needs of the design.

Steel–glass structures are considered attractive in Japanese architecture. This type of architecture symbolises modernism and vernacular concepts from an aesthetic standpoint. Furthermore, the choice of structural composition significantly impacts the realistic outcomes of the steel–glass structure. Kido et al. [4] provide several examples of typical Japanese practices. Several architectural methods are presented, including those that pertain to railway stations [5], passenger service centres on expressways [6], air terminals [7], and commercial and public buildings [8]. Steel–glass structures were designed to comply with both classical aesthetic values and local cultural traditions. Therefore, the systems can be considered novel art. They [9] also discuss the evaluation criteria of the steel–glass compartment in the building. Dimensions, visual lightness, texture, reflection, transparency, colour, light, translucency, and the design context are all considered. This creates a special visual experience for visitors.

Helbig and Oppe [10] present the roofs and façade design of the United States Institute of Peace, Washington, D.C., and explain the symbolisation of the free-form steel–glass grid shell.

Therefore, the aesthetic value of steel–glass structural design is widely acknowledged in the architectural industry. As a result, it can add a layer of cultural and artistic significance to the building.

1.2.4. Mechanical Performance

With the development of the engineering material manufacturing industry, both materials can have satisfactory mechanical properties, especially glass. Different types of glass panels have been discussed regarding their mechanical performance and design principles [11]. Based on extensive research into the strength and durability of glass material, the safety of its use can be assured [12]. Steel is an unquestionably strong material that is resistant to buckling and breaking. It has a remarkable load-bearing capacity.

1.2.5. Parametric Modelling Method on Irregular Steel–Glass Structures Design

As a result of the development of building information modelling techniques and the development of the relevant modelling software industry, irregular-shaped steel–glass structures can be designed and optimised efficiently. Modifying and iterating the parametric model may be convenient. By employing parametric design, it is possible to increase the efficiency of work since irregular models must be adapted multiple times to meet technical requirements and client requirements. A number of add-ons are available for the parametric design software, which enable the design of irregular structures, as well as form-finding and mechanical simulation functions. Algorithms can be used to analyse structural and energy efficiency, as well as cost-effectiveness. Parametric design can also improve the accuracy of modelling and provide parametric data that can be used to assist in the construction and manufacture of structural members. By enabling easy sharing and modification of the models, collaboration among different specialties can also be facilitated. Parametric design software is widely available in the industry, including Grasshopper (visual programming editor for Rhino) and Dynamo (plug-in for Revit). Design requirements and designers' requirements are considered when selecting software.

1.3. Active Research on Steel–Glass Structures

1.3.1. Materials and Steel–Glass Composition

Building envelopes are usually constructed of glass or metal. Innovative building skin systems can contribute to the evolution of modern architecture [13]. Segura and Feldmann [14] propose that the glass elements are subjected to a combination of wind loads and static loads transferred from the entire structure. This can lead to uncertainty in structural analysis. In this study, the dynamic effects of laminated glass panels as a load-bearing element are examined using basic modal identification techniques. Netusil and Eliasova [15] investigate a composite steel–glass structure, and the ultimate load of such a hybrid structure is predicted. The study presented by Grenier et al. [16] provides guidelines for the design of hybrid steel–glass beams and steel–glass façade systems. In addition to steel flanges, the beams are composed of a glass web. The steel and glass members adhere together to achieve the required structural performance. Rao et al. [17] examine the potential effects of nanotechnology on civil engineering materials, including steel and glass, and their properties, including improved durability, strength, and energy efficiency. According to Netusil and Eliasova [18], adhesively bonded steel–glass composite I-section beams, as well as the possible factors that may affect their performance, have been statically evaluated. According to Pravdova et al. [19], the initial imperfections in hybrid steel–glass beams can contribute to their instability.

1.3.2. Steel–Glass Connection

A steel–glass composite system can be assembled using adhesive junctions. The overall performance can satisfy the technical, aesthetic, and energetic requirements [13]. Kruijs et al. [20] describe the design of a glass bearing connection that is associated with an acceptable level of stress, as defined by Eurocode EN1990 CC2. A study by Nhamoinesu

and Overend [21] examines the mechanical performance of adhesives used in a steel–glass composite façade. The adhesive joints are simulated, and the stress states are determined by an analytical and a viscoelastic-plastic numerical model. A series of recommendations can be made based on the results for the selection and application of adhesives for steel–glass composite façade systems. Using finite element analysis (FEA), Richter et al. [22] investigate the stress state of adhesives in multi-side bonding under varying loading conditions. According to the experimental results, as glass thickness increases, a decrease in the impact of the non-linear adhesive characteristics on the total structural behaviour of the glass can be observed. A series of experiments were also conducted by them [23] concerning multi-sided bonded joints on steel–glass façades. Steel frames with L and U shapes support the glass panels between 6 and 15 mm thick. During this test, two types of adhesives were used, 2C silicone (SI) and 1C polyurethane (PU). As a result of this experiment, essential information about safe design procedures for such bonded joints is provided. A multi-span bridge welding technique is proposed by Musalev et al. [24], along with the welding parameters for steel–glass liners. According to Tutunchi et al. [25], the addition of Al₂O₃ nanoparticles to a two-part structural acrylic adhesive can enhance the bond strength and durability between steel and glass. As part of their study [26], silica nanoparticles were also added. An investigation by Van Lancker et al. [27] examined the strength behaviour of adhesive bonds under extreme environmental conditions. The study by Odenbreit and Dias [28] shows that adhesive jointing can increase the load-bearing capacity of steel–glass beams. Ligaj et al. [29] investigate the value of stresses in glued aluminium alloy and glass joints in vehicles under conditions of four-point bending. During the testing process, the stress is related to damage that is initiated in the joint being tested. In a study by Chavooshian et al. [30], silicon carbide nanoparticles were added to steel–glass/epoxy composite joints bonded with two-part structural acrylic adhesives in order to enhance adhesive strength. An investigation of steel–glass orthogonal lap joints with silicone adhesive was undertaken by Wang et al. [31]. According to the study, failure is related to the thickness of the adhesive and the overlapping length of the composition. Using this analytical formula, the shear strength of the bond is then determined based on the equilibrium of strain and force. In Amstutz et al. [32], digital image correlation is used to measure a polyurethane adhesive’s local multiaxial deformation behaviour. These outcomes can be used to identify a constitutive material parameter and to formulate hyperelastic materials models. In this way, the non-linear elastic behaviour under multi-axial loading conditions can be predicted using finite element analysis. A study by Katsivalis et al. [33] investigated the stress states and failure behaviour of adhesives used in the connection between mild steel and tempered glass. The researchers conducted a numerical simulation in order to determine the adhesive pressure-sensitivity, plasticity, and failure mechanisms, as well as to determine how the adhesive will behave overall over time. A study by Biolzi et al. [34] examines the behaviour of silicone-bonded joints for steel–glass structures at high temperatures. Various structural adhesives are evaluated based on their mechanical properties. As a result, we can provide possible guidelines for choosing a finite model and calibrating it.

1.3.3. Analysing Methods and Industry Standards

Architects are constantly striving to create transparent and delicate structural elements. In recent years, glass has become an increasingly popular alternative to concrete walls and roofs. The use of it in the façade is also an example of this. As a result, glass is gradually becoming a mainstream element of space enclosing, but it is also receiving greater attention for its capacity to bear loads. Special-shaped buildings with complex curved façades and roofs are often constructed with steel–glass structures. The shapes can be intuitively expressed as a part of the original design concepts from the architects. Thus, an analysis of the structural integrity of this building structure is required. In the industry, however, the relevant design standards need to be present. Moreover, due to the complexity of the curved surface shape, each case has an entirely different shape and structure. In terms of

precedents, a few can be used as examples. Among other things, Adriaenssen et al. [35] describe a method used to determine the adhesive properties for non-linear numerical simulations of structural steel–glass connections and present the mechanical behaviour under different loading conditions. After proving the feasibility of the method, they offer a real-life case.

The study by Richter et al. [36] examines the nonlinear stress–strain behaviour of steel–glass façade panels with multi-side bonding under complex loading scenarios and provides guidelines for designing such boards. Dias et al. [37] describe the development of constitutive hyper-elastic material law and implementation of the law for numerical simulations using the finite element software Abaqus. Through this method, the structural silicone for steel–glass connections is simulated, and the results are in agreement with those obtained during the experiments. According to Espinha et al. [38], the geometry and structure of the terminal building at Baku Airport in Azerbaijan were designed during the design process. In addition, they describe the impact that construction and seismic considerations have on the design concept. In Pravdova and Eliasova [39], the lateral and torsional stability of the steel flanges and glass web connection is examined. Based on Wang et al. [40], laminated glass webs with steel flanges may have a higher ductility than glass panels. The authors conduct an experimental analysis of the behaviour of the hybrid beams under in-plane shear compression and assess the influence of adhesive on their behaviour. It is evident from the results that the test sample has higher strength, and the mechanism proposed gives a better prediction of strength than the formulas referred to. Hoffmeister et al. [13] demonstrate the possible application of glass panels having hyperbolic paraboloid shapes to steel–glass structures. In the late 1990s, Adriaenssens [41] described an approach to form-finding and structural analysis developed by Michael Barnes. Numerous architectural designs have been created using this technique, including the steel–glass dome of the Dutch Marine Museum. As an extension of Grasshopper in Rhino, a program that provides parametric modelling, the concept is also utilised in Kangaroo, a mechanical analysis plug-in for Grasshopper. As a result of lateral torsional buckling of glass beams with lateral restraint, Adriaenssens [41] investigates its mechanisms. To complete the research, they resort to finite element simulations and apply the theory of buckling curves and non-dimensional slenderness factors. Moreover, Eliasova and Pravdova [42] studied the lateral torsional buckling of steel–glass beams. In this beam, glass webs are connected by steel flanges. A study conducted by Firmo et al. [43] examined the composition details of an I-shaped hybrid steel–glass beam (HB) and the safety of the design. A comparative analysis is performed of four prototypes in order to examine the global deformation behaviour, as well as the distribution of strain and cracks. Using such a technique can aid in the development of relative design concepts and assembling strategies. The study by Tahmasebinia et al. [1] examines the load performance of a steel–glass spindle torus shape structure utilising Strand7 (R2.4.6) and ABAQUS (6.14), referring to the Jewel Changi Airport in Singapore as an example. On models with straight and curved steel members, there seems to be a divergence in the structural analysis results. Beam buckling behaviour can be affected by boundary conditions, L/R ratios, and boundary conditions. Using a tensegrity floor design, Scoccia et al. [44] examine the structural performance of this innovative concept. A specific steel–glass joint adhesive technique is used in this technique, which facilitates the combination of different materials. As a result of their investigation of the nodes and joints of steel–glass lightweight floors, Marchione et al. [45] constructed a prototype based on the tensegrity floor technique and investigated the application of adhesive. Verification of the structure’s actual behaviour is conducted.

1.3.4. Industry Application of Steel–Glass Structures

A case study of the glass canopies at the Lincoln Center is presented by Knippers et al. [46], which discusses the structural and architectural features of the steel–glass structures. Several factors must be considered when designing the hybrid steel–glass building skins and their connections, as highlighted by Silvestru et al. [47].

Heimbig et al. [48] introduce the free-form steel-and-glass canopy covering the atrium of “Casas hopping,” a luxury home furnishings centre in Rio de Janeiro, Brazil. Prefabrication of the high-precision node–beam system was used in this project, which posed a challenge to the construction team. Defalco et al. [49] propose the use of external hybrid steel–glass frameworks to consolidate reinforced concrete structures in social housing. The numerical calculations and design considerations of the insulated glazing units used in this project are presented by Heinze et al. [50]. Maier et al. [51] propose an extension project for the university’s central refectory. A spannable entrance yard is achieved through the use of the steel–glass structure. By combining the design of the renovation of existing facilities, underground engineering, reinforced concrete structures, and other fundamental fields, the BIM technique is used in this project. One of the steel and glass structures that can be found at Kazakhstan Expo is the Sphere. This bridge was built to connect two adjacent buildings in Germany, which became the headquarters of one corporation. Mahl et al. [52] described this bridge as having a complex crystalline-like shape. It is known as Capricorn Bridge and is made up of polygonal elements of glazing. Building axes, circulation patterns, and existing building circumstances contribute to the complex shape of the glass surface. During the design of the new science building of the University of Basel, a skylight was designed to cover the central atrium. As a result of the grid shell structure, the atrium was able to achieve the required amount of indoor illumination. An approach called form-finding was used to model the shape [53]. According to Adriaenssens [54], Laurent Ney is well-versed in digital and numerical methods of shape-finding and optimisation, as well as providing construction guidelines as a structural designer. As an architect, he was involved in the design processes of the Dutch Maritime Museum and the Knokke Lichtenlijn footbridge. There were two types of steel–glass structures designed by him for the two cases, namely, a grid shell and a hanging steel shell.

1.3.5. The Application of Building Information Modelling (BIM)

A BIM system allows the application of prefabricated building modules in a missive manner [55]. The system is capable of realising the entire design concept. In addition, it can provide the capability to manage and evaluate a plurality of significant aspects of the building process. Design stages can be communicated more effectively, and designers’ workload can be reduced as a result. As well as optimising structural efficiency or cost, it can also be utilised for other purposes. Based on algorithms, Nazar and Slyk [55] developed structural control modules and computational methods that are applicable to masonry, steel, glass, and timber structures. The authors argue that the systematic application of BIM and efficient project management methods contributes to the success of their study. A steel–glass system is being constructed using extended reality (XR), a visualisation technique, as part of the construction process. Furthermore, they explore the relevant wireless networking technologies and optimise the interaction between different software modules. Afterward, a discussion of how the industrial internet of things and augmented reality technologies will develop in the future is presented.

Over the past decade, it is evident that there has been an increased level of research activity in the steel–glass structure field. As a consequence of the literature mentioned earlier, valuable information can be gained regarding steel and glass materials and composition, steel–glass structure connections, advanced structural design and analysis techniques, and their application in various industries. In the present study, methods of parametric modelling and structural numerical analysis will be investigated in more detail for irregular-shaped steel–glass structures with straight and curved structural members with straight and curved constituents. Additionally, the entire working flow will be demonstrated from the modelling to the structural analysis phases.

2. Creating Grasshopper Script

The purpose of this section is to describe how Grasshopper, Rhino 7’s internal visual programming engine, is used to create and edit 3D models of each structure in Rhino 7.

With the Container feature, script segments can be grouped for easy workflow organisation in Grasshopper.

2.1. Phoenix International Media Center in Beijing

An irregular torus-shaped building, the Phoenix International Media Center stands 55 m high. The area of the building is approximately 135 m by 135 m, or 18,000 m². It is apparent upon closer inspection that the structure consists of two main beam members that wrap around the façade in opposite directions, crossing over each other and connecting. There is no internal support system modelled in this study. As a result, the structure has been reduced to 50% of its original volume, resulting in a height of approximately 22 m. It takes up only 67 by 67 m. Figure 1 shows the final Rhino 7 model.

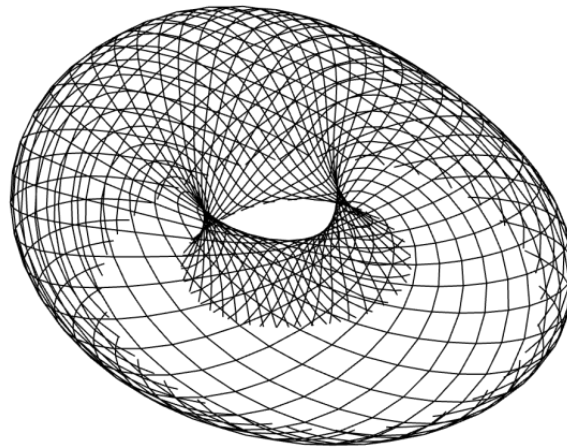


Figure 1. Phoenix International Media Center model created using Rhino 7's internal visual programming editor, Grasshopper.

Process of Creating the Rhino 7 Model Using Grasshopper

The overview step-by-step process shown in Figure 2 includes creating the underlying shape with Elliptical Torus, transposing it such that its base aligns with $z = 0$, then extracting a frame from the surface created using Surface to Frame, and finally extracting individual beams from this frame using Frame to Curve.



Figure 2. Overview of the Grasshopper script used to create the Phoenix Center.

The Elliptical Torus container is where the base shape is created. Shown in Figure 3, a guideline circle is made with the Circle function, with its radius controlled by a Number Slider. Along this circle, planes are created, aligned perpendicular to the circle's tangent. The number of planes is controlled by a Number slider. On each plane, an ellipse is created using Ellipse. The major and minor axes of these ellipses are controlled by Number sliders. These ellipses are then rotated about the planes they were created on, based on a range of angles created with Range. The range of angles is created such that all the ellipses when viewed together make a full 360 turn about the circle. The result can be seen in Figure 4.

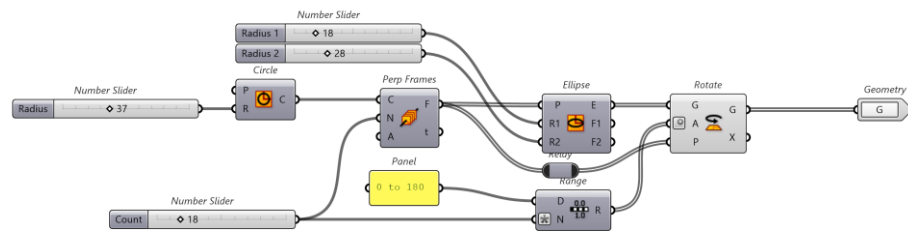


Figure 3. Elliptical Torus container. Note that the A input for Rotate has a dot symbol next to it, indicating that the input is converted to degrees.

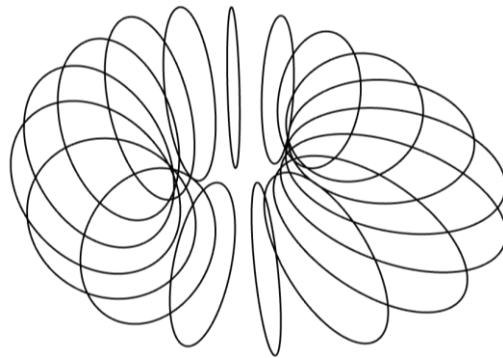


Figure 4. Elliptical Torus output.

The Level with Ground container does exactly that, it adjusts each ellipse created by Elliptical Torus such that its bases is level with 0,0,0. Shown in Figure 5, the container first gets the minimum Z height of each ellipse. Bounding Rectangle will create rectangles on a defined plane (in this case, the XY plane) and outline the extent of an object (in this case, every ellipse). When applied to the ellipses, Bounding Rectangle outputs a list of rectangles, defining where the rectangle is and how large it is. The Area function can then be used to extract the centroid of these rectangles, essentially outputting the bottom of each ellipse. Curves defined in Rhino 7 require a seam, which, for the purposes of this study, they simply define the start and/or end. It is important to have the seam at the bottom of the ellipse before moving it. To accomplish this, the centroid from Area outputs to the XY Plane, which creates an XY plane at the location of the input. These planes are then used by Curve | Plane to extract the curve parameters of the intersected ellipses. For context, when resolving intersection events for curves (like that of the ellipses), one of the parameter outputs, t, describes where along the curve the intersection takes place. We can then use this parameter to transfer the seam to the intersection point. Essentially, Curve | Plane and Seam work together to move the seam to the bottom of the ellipses. Now, using Deconstruct and unit Z, a vector for each ellipse can be created, which indicates its distance from z = 0. Using Move, each ellipse is moved to be level with 0,0,0. The output can be seen in Figure 6.

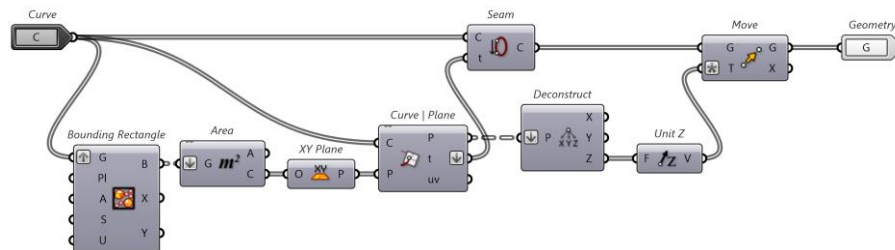


Figure 5. Level with ground container. Note that the down arrow means the input list has been flattened.

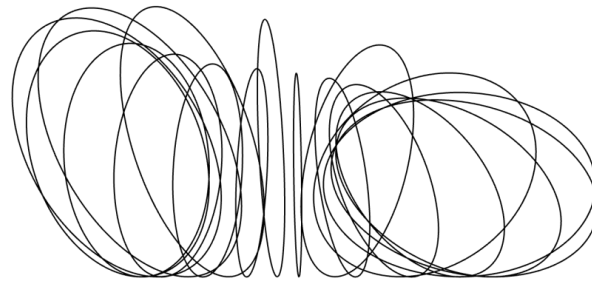


Figure 6. Level with ground output.

Surface to Frame takes these ellipses and creates the diamond pattern frame from it. The container is shown in Figure 7; it first uses the ellipses to create a surface with Loft. Loft is a function that takes a group of curves and attempts to draw a surface connecting each of them. This surface is then used by Diamond Tiling to create the diamond pattern. This pattern is controlled by a couple of Number Sliders, which define how many diamonds in each direction. The pattern is then scaled using Scale, controlled by another Number slider. It is important to understand that the Diamond Tiling is a mesh, not a list of curves, with each diamond panel being a mesh face. These mesh faces are then converted to surfaces with SubD from Mesh. So, now each diamond is an individual surface. The wireframe, basically the outline, is extracted from each surface using Brep wireframe. The bottom section of the entire structure is cut away to create the anchor points of the structure. This is achieved with Trim with Brep, the brep in this case being a rectangular box made with the Big Box container. The entire structure must then be transferred to be level with 0,0,0 again. The result is similar to what can be seen in Figure 1.

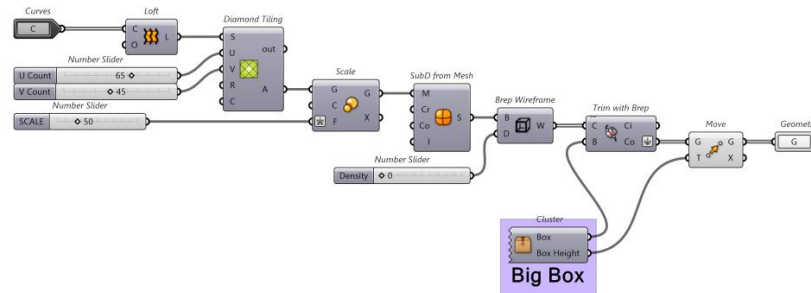


Figure 7. Surface to Frame container. Note that the Diamond Tiling function comes from the M+ plugin for Grasshopper.

The Big Box container simply creates a rectangular surface that is used to trim the curves with. Seen in Figure 8, it does this using Domain Box, Construct Point, and Construct Domain controlled by Number slides.

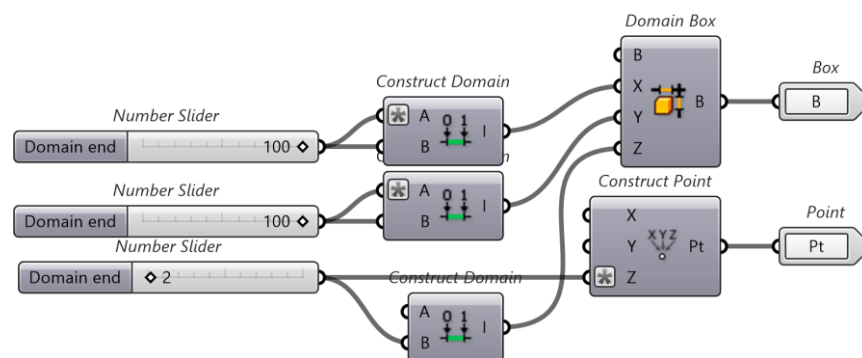


Figure 8. Big Box container.

The final container, Frame to Curve, simply divides the curves up into several segments using Divide Curve, controlled by a Number slider. The points for each segment are imported to Polyline, which creates a series of lines between each point for each curve segmented. The polyline is then broken up by Explode. To ensure that there are no duplicates, removeDuplicateLines is used. To export the results, simply select removeDuplicateLines, right click, and select bake. This should generate the model in the Rhino 7 workspace, which can be exported to a dxf file. Figure 9 shows the Frame to curves container.

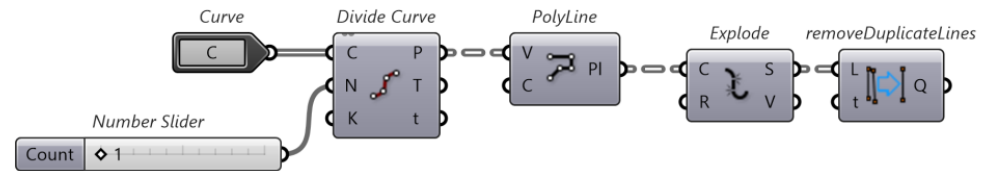


Figure 9. Frame to Curves container.

Note that removeDuplicateLines comes from the Kangaroo2 plugin for Grasshopper.

2.2. CAD Model of the Kazakhstan Pavilion and Science Museum (Rhino 7)

The Kazakhstan Pavilion and Science Museum is a 100-metre-tall building, with a spherical steel–glass façade, located in Astana, Kazakhstan. Upon close inspection, the major beam members spiral up the surface of the façade, with a minor beam member providing lateral support at certain intersections. At the top of the pavilion, there is also a section removed from the façade to make way for solar panels and wind turbines. For the purposes of this report, only the spherical steel–glass façade section was modelled in Rhino 7. This section is roughly 80 m in diameter, with a tubular section cut out of it at the top. This report does not consider the weight of the solar panels and wind turbine located at the top of the structure. As compensation, this report also assumes that the steel–glass façade is entirely supported by itself, with no added internal support structure. The final Rhino 7 model is shown in Figure 10.

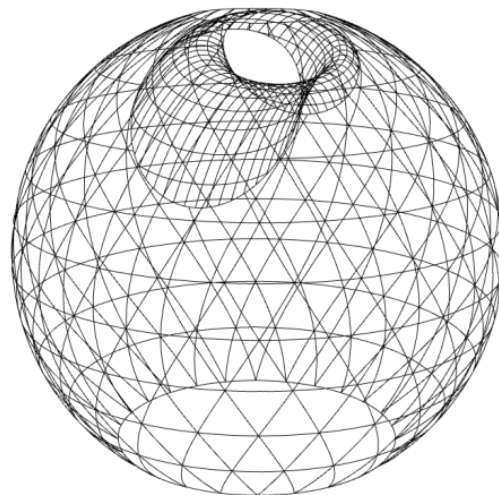


Figure 10. Final model of the Kazakhstan Pavilion using Rhino 7.

Process of Creating the Rhino 7 Model Using Grasshopper

This section is a step-by-step process on creating the Grasshopper script that creates the structure shown in Figure 10. The overall layout of the Grasshopper script is shown in Figure 11, below.

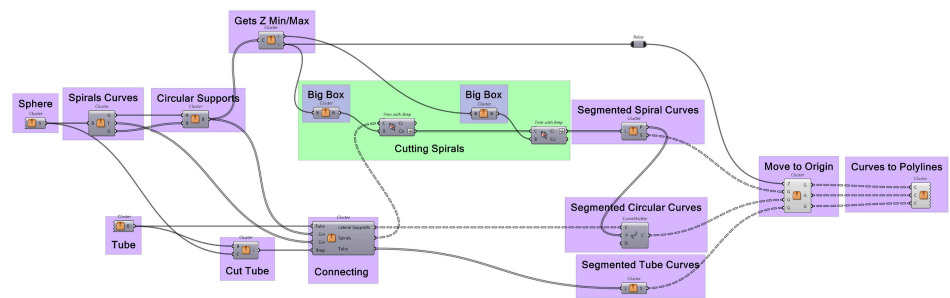


Figure 11. Capture of entire Grasshopper script for creating the Kazakhstan Pavilion.

We start with the basic shapes of the Kazakhstan Pavilion, which is a sphere with a tubular section cut from the top of it. Creating the sphere is accomplished by specifying the base plane and radius, shown in Figure 12.

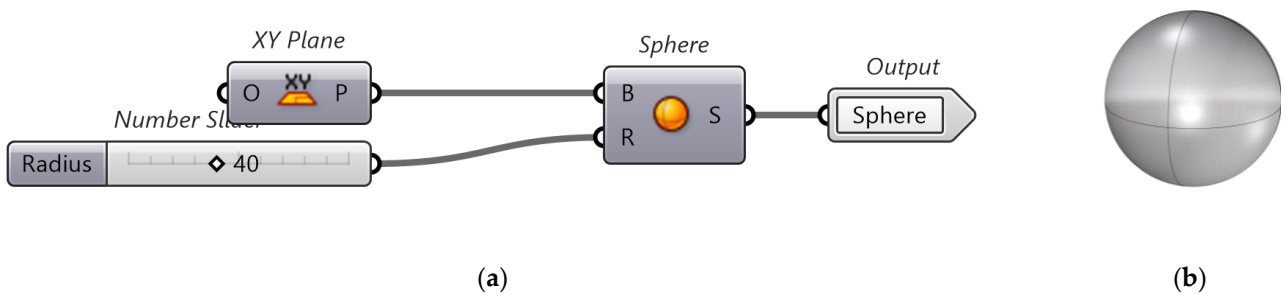


Figure 12. (a) The ‘sphere’ container that defines the base plane and radius of a sphere. (b) The resultant sphere.

The tube is created by extruding an ellipse along an elliptical curve. Shown in Figure 13, the cross-section of the curve is defined by the ellipse with a XZ base plane, such that it coincides with the extruded path. It is then extruded along this path to create a ring-like structure. This ring is then cut in half with the Plane Trim Surface function to ensure the tube intersects with the sphere only once. It is important to offset this trim by a unit to ensure the holes of the resultant tube can be capped.

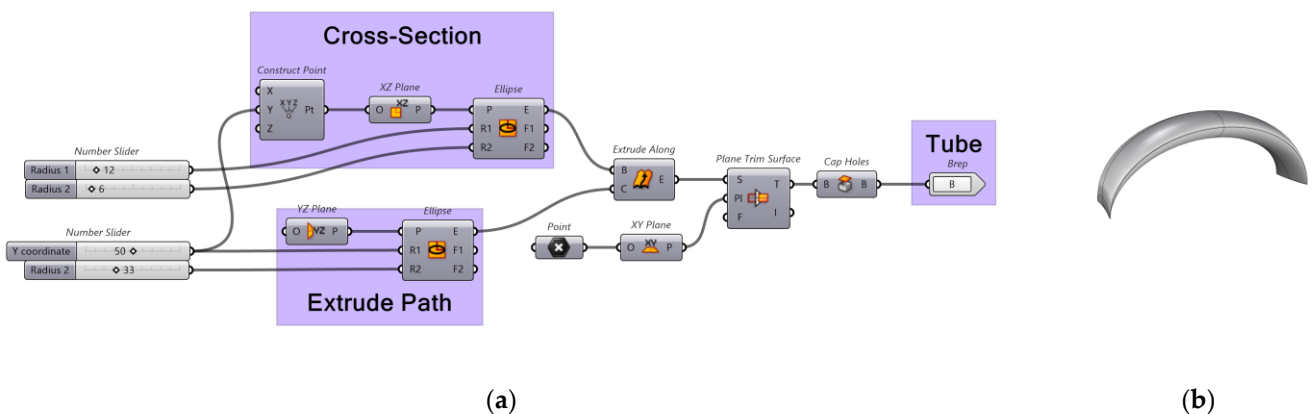


Figure 13. (a) Capture of Tube container. (b) Resultant surface in Rhino 7 port view.

The sphere and tube are then used to cut each other with. The Tube Cut container uses B (shape to split) and C (shape to split with) variables to output the section of the tube encapsulated by the sphere. Shown in Figure 14, the Tube Cut container uses the Split brep function to segment the tube into three parts. List item then selects for the section of the tube encapsulated by the sphere, in this case at index 2. Afterward, the middle tube section is transformed into a mesh of curves using the Brep wireframe function, with an integer slider determining its density.

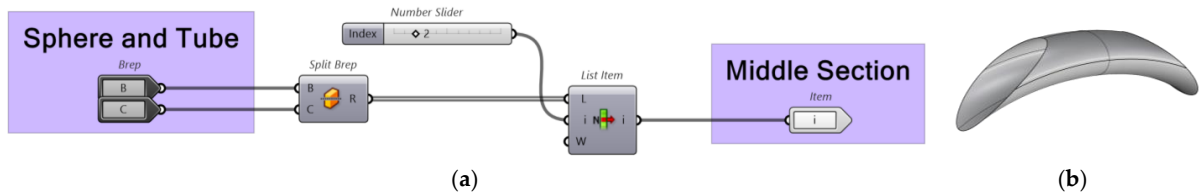


Figure 14. (a) Grasshopper Cut Tube container. (b) Port view of resultant surface.

The sphere surface is imported into the Spiral Curves container, shown in Figure 15, which outputs a single spiral, all the spirals, and half the spirals. It does this by extracting the Interior edge curves from the imported sphere surface (basically a line from the top to the bottom, along the surface of the sphere). From this edge, a straight line is constructed connecting the top and bottom of the sphere. This line is used in the Twist function to transform the edge line into a spiral that lies on the surface of the sphere. The twist is controlled by the Angle slider. The twist is performed twice, once clockwise and another anti-clockwise. These twists are then duplicated with duplicate data and are rotated about the straight line passing through the top and bottom of the sphere. The Steps number slider controls the number of times the twist is copied. The number of copies is used to create a range of numbers from 0 to $2 \times \pi$, which is used in the Rotate function to ensure that the twists are evenly spaced apart from each other. Before outputting the spirals, the original twisted lines are removed from the list by use of the Split list function as index 1. These lists from clockwise and anti-clockwise twisting are merged to output all of the spirals together, while a single spiral and half of the spirals are output separately for future use. It should be noted that the single spiral and half of the spirals twist in different directions, such that they intersect, as shown in Figure 16.

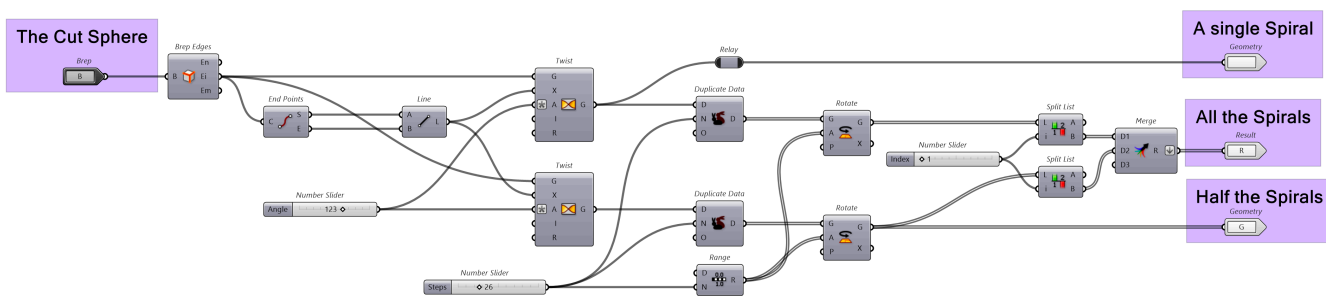


Figure 15. Grasshopper Spiral Curves container. Note that the merge output has a down arrow, meaning that it is flattened. Similarly, the Angle input of the twist transformations has an asterisk, meaning that there is a custom expression that alters the angle input to something else based upon what equation was input. In this case, the expression is the function for converting degrees to radians.

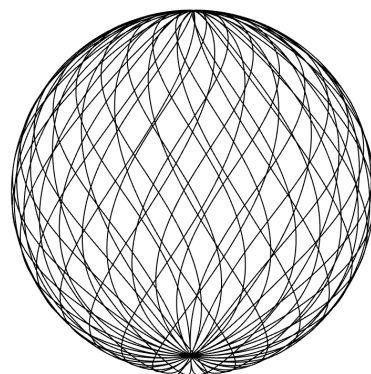


Figure 16. Port view of curves generated from the container shown in Figure 15.

The single spiral and half the spirals are used within the Circular supports container, shown in Figure 17, to create the lateral supports. Using the Curve | Curve function to determine all intersection points between the single spiral and half the spirals. The intersection points are deconstructed into their constituent coordinates. These coordinates are used to create circles, with the Z coordinate determining the plane offset from 0,0,0, and the X and Y coordinates are used to calculate the radius of each circle. To ensure that only non-zero-length circles are output, the Includes function can be used to measure the length of each circle and output a key list. This key list is used by the Dispatch function to separate the non-zero circles and output them. The result can be seen in Figure 18.

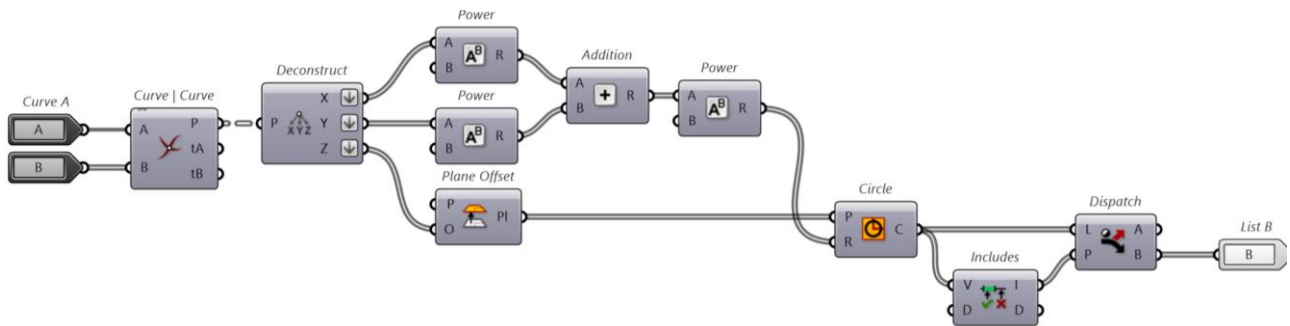


Figure 17. Grasshopper Circular Supports Container.

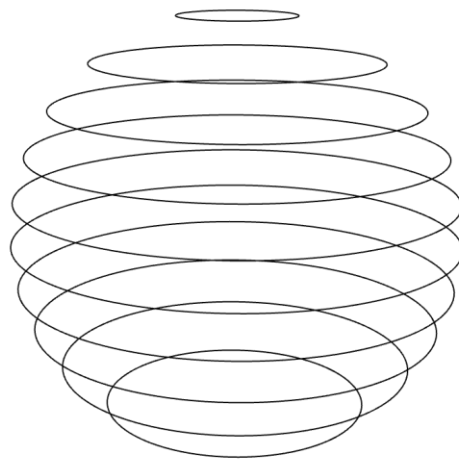


Figure 18. Port view of resultant curves from container depicted in Figure 17.

Because the spirals and circular supports were created from the same surface, they will be joined at intersections. Connecting the tubular curves to everything else will be more difficult. The Connecting container, shown in Figure 19, takes the circular supports, spiral curves, middle section of tube, and the entire tube as inputs and outputs the Lateral supports, Spirals, and Tube wireframe, all connected as separate lists of curves. First, a wireframe of the tube cut out is made with Brep wireframe, with the density being controlled by a number slider. This wireframe is essentially a collection of curves: closed, open, elliptical, etc. The tube only connects with the spiral and lateral supports at its edges. The dispatch and closed functions are used to test for closed curves and separate them out from the rest of the wireframe collection. There are several closed curves, but fortunately, the first two are always the edge cases. Using split list and list item, each edge curve of the tube wireframe can be used to test for intersections points with the spiral and lateral curves. This is accomplished with the Curve | curve function, with the Spiral and support curves being merged into one list and flattened. The Curve | curve function outputs all the intersection points between the tube wireframe and the other curves. These points are then used to shatter the edge case curves of the tube wireframe. The wireframe collection is then merged back together and flattened. This ensures that the tube wireframe will always

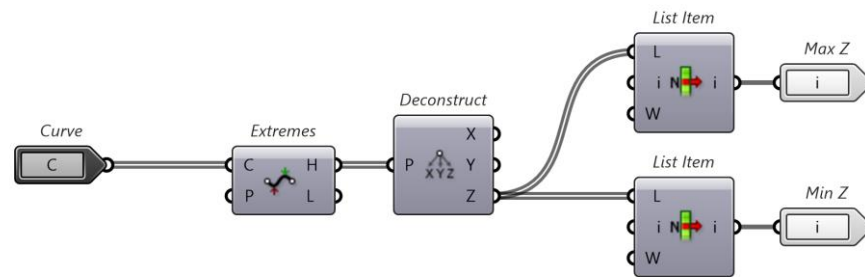


Figure 21. Get Z max/min container. Note that the top List Item has a defined value of -1 , because the function interprets this as the end of the list it is reading. You can change this by right clicking on the 'i'.

Using the max and min from this, giant rectangular boxes are made to trim off the excess spiral curves. Figure 22 shows the container that creates these boxes. For a given Z input, a giant box will be made.

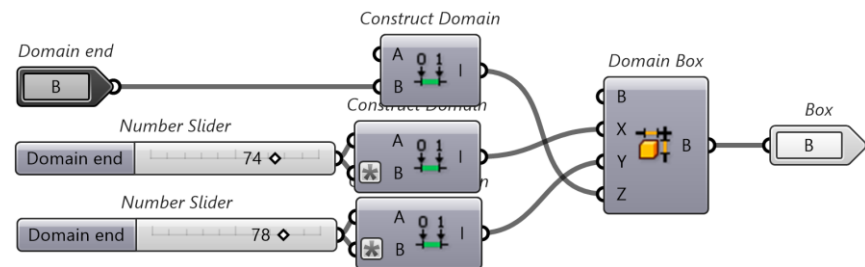


Figure 22. Big Box container. Note the Asterix, where the expression is $-X$.

Using a pair of boxes, one with the minimum input and another with the maximum input, the entire model can be sandwiched between two boxes, from which a Trim with brep function is used to separate the excess spiral curves. Figure 23 shows the result.

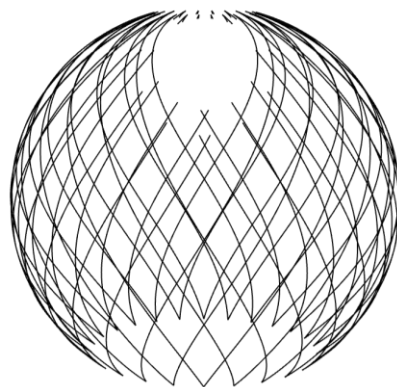


Figure 23. View port of the excess spiral curves cut off.

All the curves in the spirals, circular supports, and tube must be broken up into smaller segments at points of intersection with one another. To accomplish this, the Segment spiral/tube Curves container, shown in Figure 24, takes a collection of curves and outputs another collection of curves, such that they are split at points of intersection. The multiple curves' function outputs are bundled into two groups: iA and iB , and tA and tB . iA and iB list which curves are intersecting with each other, while tA and tB list how far along these intersection points are along the curves. These groups start unorganised; using the create set and member index, the correct pairs of curves can be correlated with the correct intersection points. These points are then used to split the original big curves into smaller ones.

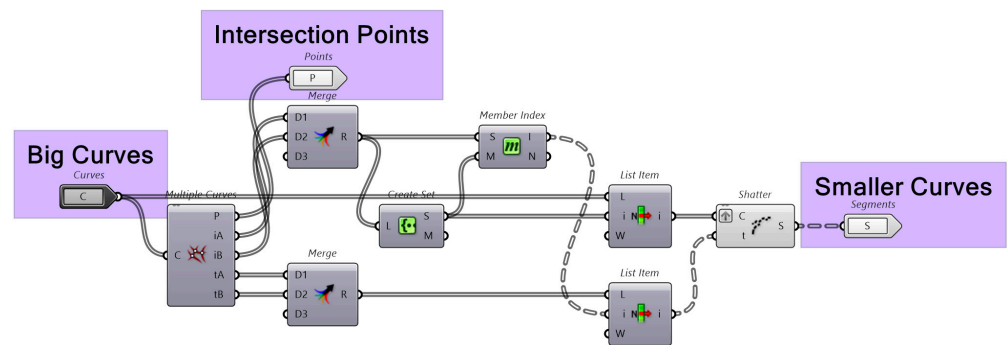


Figure 24. Segment Curves container. Note that the only difference between the ‘Segment Spiral Curves’ container and the ‘Segment Tube Curves’ container is that the intersection points are an additional output for the ‘Segment Spiral Curves’ container.

For simplicity, the entire model is moved, such that the lowest point is at the origin. This is accomplished in the Move to Origin container shown in Figure 25. The minimum point from get z max/min container is used for the transformation. The Vector XYZ function creates a vector from the origin to the specified X, Y, Z input. This vector is used by the Move function to translate the entire model.

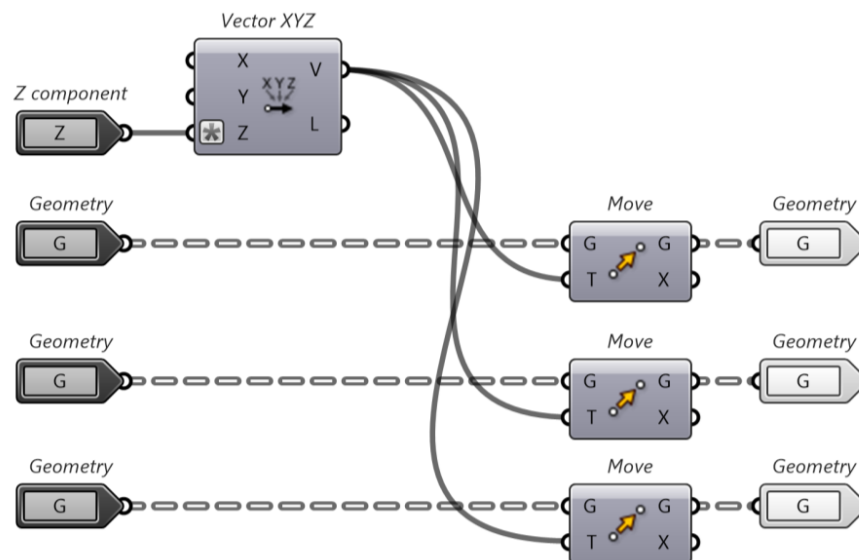


Figure 25. Move to Origin container.

The final step is transforming the segmented curves into polylines and cleaning up any duplicates. The Curves to Polylines container, shown in Figure 26, accomplishes this by using the divide curve function, which outputs points along a curve, controlled by a number slider. These points are fed into the polyline function, which connects these points together as straight lines. The Explode function then separates these polylines into their segmented pieces between points. Finally, the removeDuplicateLines function removes any duplicate lines that were created.

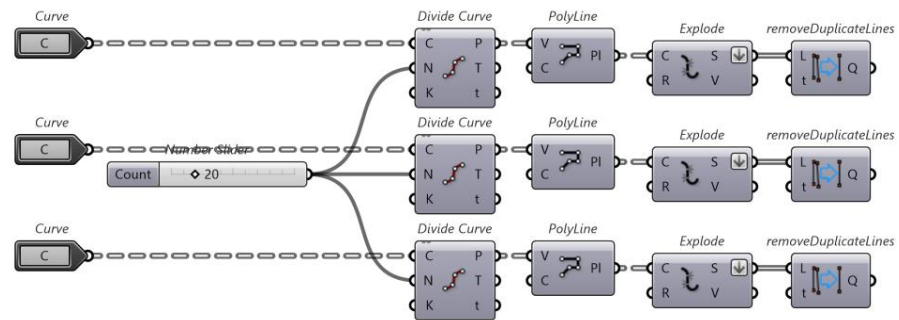


Figure 26. Curves to Polyline container. Note that the removeDuplicateLines function comes from the Kangaroo2 plugin for Grasshopper.

2.3. Moynihan Train Hall

After renovations and extensions, Moynihan Train Hall reopened in 2021. This project is a great instance of combining historical architectural elements with modern architecture. Moreover, the design of the whole project considered the sustainable development of the building [55–57]. The building was originally designed by McKim, Mead & White in 1910.

The renovation project was designed by Skidmore, Owings & Merrill (SOM), and the dome-like glazing system over the train hall was designed by Schlaich Bergermann Partner [58]. There are four steel–glass structural skylights sitting on three steel trusses over the train hall. The structural design of the skylight utilised lightweight grid shell, reducing the overall load on the building from the structure. In addition, the outwardly protruding skylight enhances the illumination in the train hall. The wavy-shaped structure also endows lightness to the structure. The structure uses diagonal cables to provide in-plane and shell support in the actual project; however, the simplified model was used for structural analysis in this project.

2.3.1. Process of Creating the Rhino 7 Model Using Grasshopper

This project only focuses on a simplified shape of the skylight structure. Thus, the analysis is based on the following model shown in Figure 27.

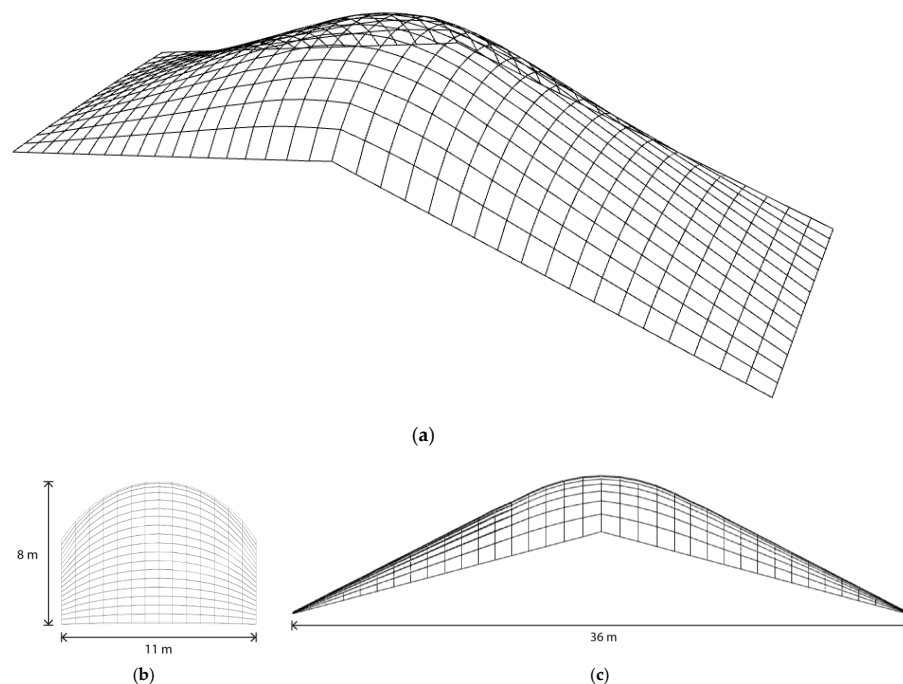


Figure 27. Schematic design of the model. (a) Prospective view; (b) Short elevation view; (c) Long elevation view.

Rhino with Grasshopper is used to create the overall shape and generate the wireframe model. The basic logic to model is the property of the control points curve. The difference between the polyline and control points curve is shown in Figure 28.

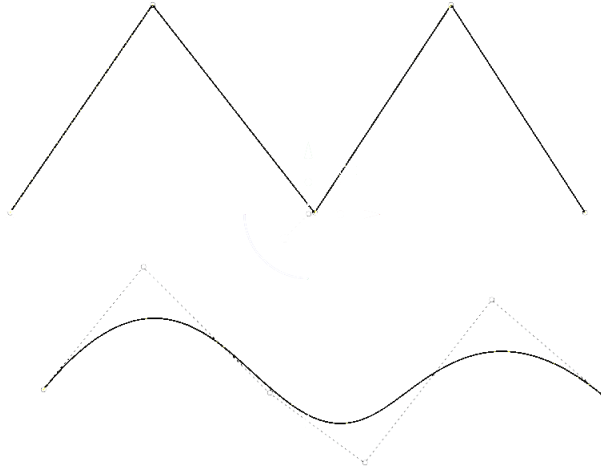


Figure 28. Polyline and Control Points Curve.

2.3.2. Create Base Line

The first step is to create a base line, and the following modelling steps are derived from it. The base line length is assumed to be equal to the short span (11 m). The direction is set along the x axis. Thus, two points are constructed with the same y and z coordinates and distinct x coordinates. The difference between the x value of the 2 points is 11. The line is created by connecting the start and end points, as shown in Figure 29.

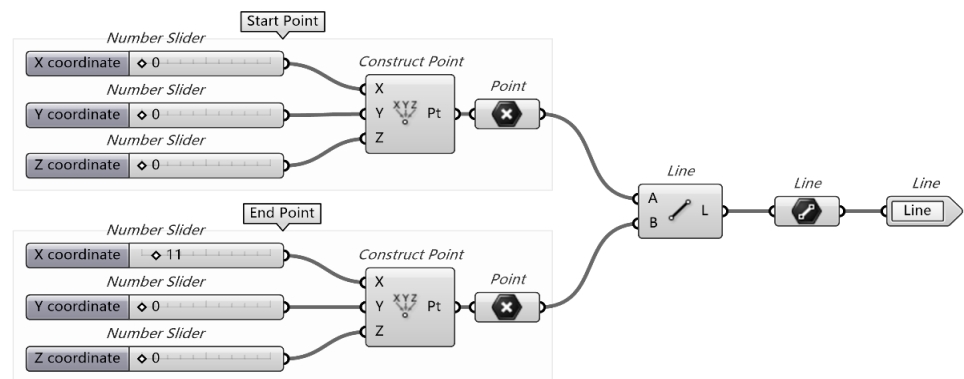


Figure 29. Create Base Line.

2.3.3. Create Base Control Points

The modelling of a surface in Grasshopper is to edit its parametric properties. Thus, setting up the initial control points is crucial. The points can be generated by setting up the lines. The base line needs to be copied and moved to suitable positions, as shown in Figure 30. Since the interval between each horizontal and vertical structural curve is assumed to be same, a series can be used to setup the y coordinate for each line.

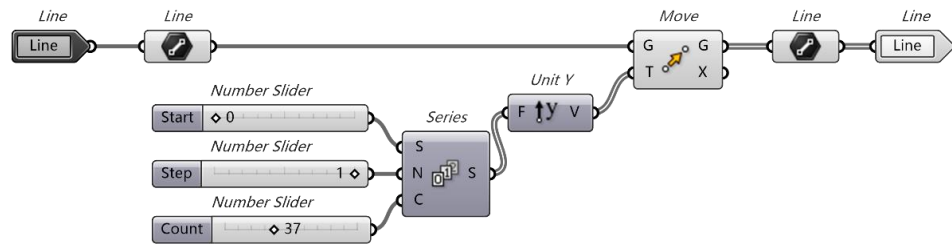


Figure 30. Move and Copy the Base Line.

The step size for the series is 1 m, and the number of steps is 37, which means the total length is 36 m. Then, divide curve battery is used to derive the control points. The number of points created on one line can be adjusted by the number slider. The number of control points depends on the modelling accuracy required. Six points are chosen in this case, as shown in Figure 31.

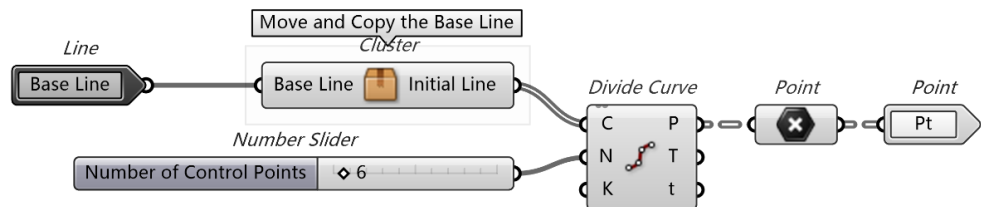


Figure 31. Create Control Points.

2.3.4. Adjust Control Points

The adjusting processes is related to the complexity of the surface and the number of base control points. After editing the control points, a control points curve can be generated.

Therefore, the points should be adjusted and form a similar arrangement to the shape of the reference model. Moreover, the points with the same x coordinate are considered as in one group. Since the points are in the same plane ($z = 0$), the z coordinate should be modified to form the target shape. The operations are based on groups. For each operation, the specific group of points is extracted from the dataset of the base control points, as shown in Figure 32.

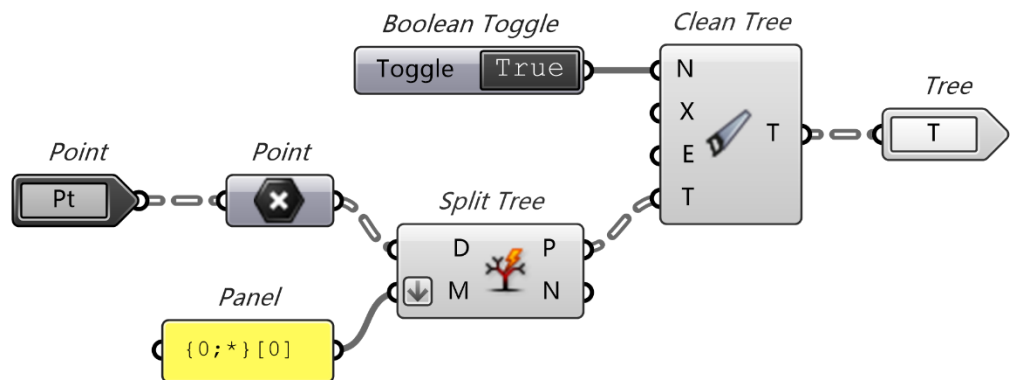


Figure 32. Select the Interested Line of Points.

Then, as shown in Figure 33, the extracted points are further divided into subgroups and manipulated separately based on the needs.

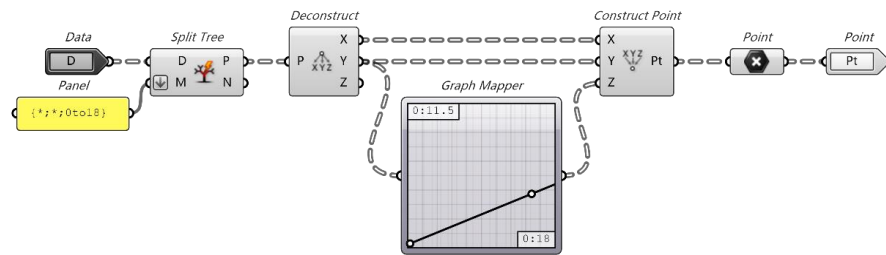


Figure 33. Adjust Points' Position.

This step can be repeated several times until the overall shape formed by the control points is similar to the reference model.

2.3.5. Create Control Points Curves from Adjusted Points

As shown in Figure 34, since the points are adjusted separately, merge battery can be used to create a completed dataset including all the control points. Then, the points can be used to generate curves, and the curves are in the x direction.

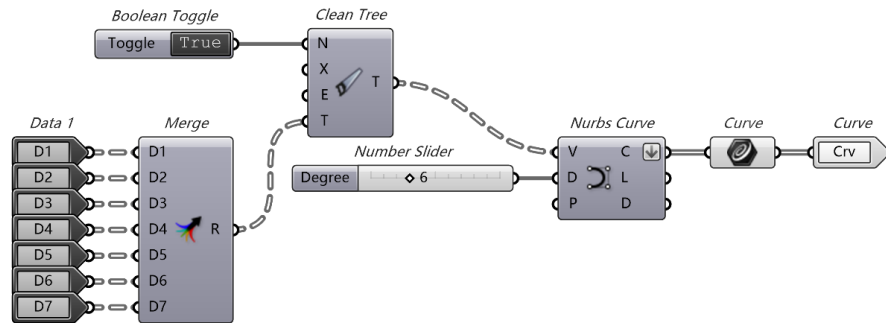


Figure 34. Create Control Points Curves from Adjusted Points.

2.3.6. Create Surface and Wireframe

The curves can be lofted to generate a surface, and the surface can be turned into a grid shell. Subsequently, the wireframe can be extracted. The operation is shown in Figure 35.

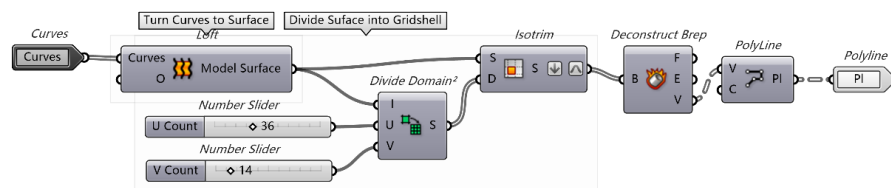


Figure 35. Create Surface and Wireframe.

2.3.7. Create Surface and Wireframe

As shown in Figure 36, since the wireframe is generated from the subsurface edges, duplicated curves need to be cleaned. Moreover, to study the curved member, the subdivision on the straight member is also included.

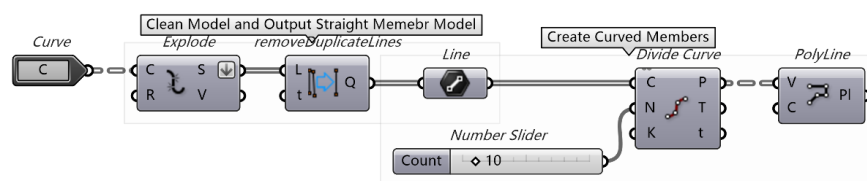


Figure 36. Model Cleaning and Output.

2.4. Chadstone Shopping Centre

2.4.1. Overview

The glass–steel roof analysed in this case is part of the expansion project of Chadstone Shopping Centre in Melbourne, Australia [59]. It is the largest shopping centre in the Southern Hemisphere. The roof is composed of steel framework and glass panels with double curvature [60]. The structure forms a seamless cover to the building's body. It replaces the solid concrete roof and improves the indoor illumination. The complicated curved shape also creates a special atmosphere for the shopping space.

2.4.2. Process of Creating the Rhino 7 Model Using Grasshopper

The grid shell roof is modelled using the combination of Rhino 7 and Grasshopper and analysed using Strand7. Since it is in a complicated curved shape, the simplified model can be handmade in Rhino 7 initially. Then, Grasshopper can be used to generate the wireframe model based on the model. Subsequently, the analysis is based on the following model.

As shown in Figure 37, there are two legs for this structure. The angle between the legs is about 30 degrees. The length of the bottom leg is 103 m, and the upper leg is 75 m with a dome, 20 m in length, and 18 m in width. There is also a dome-like structure on the bottom end with a length of 30 m. The width for the bottom leg is 19 m, and the upper leg is 18 m. The width for the corner is about 35 m, and the height of the whole structure is about 17 m.

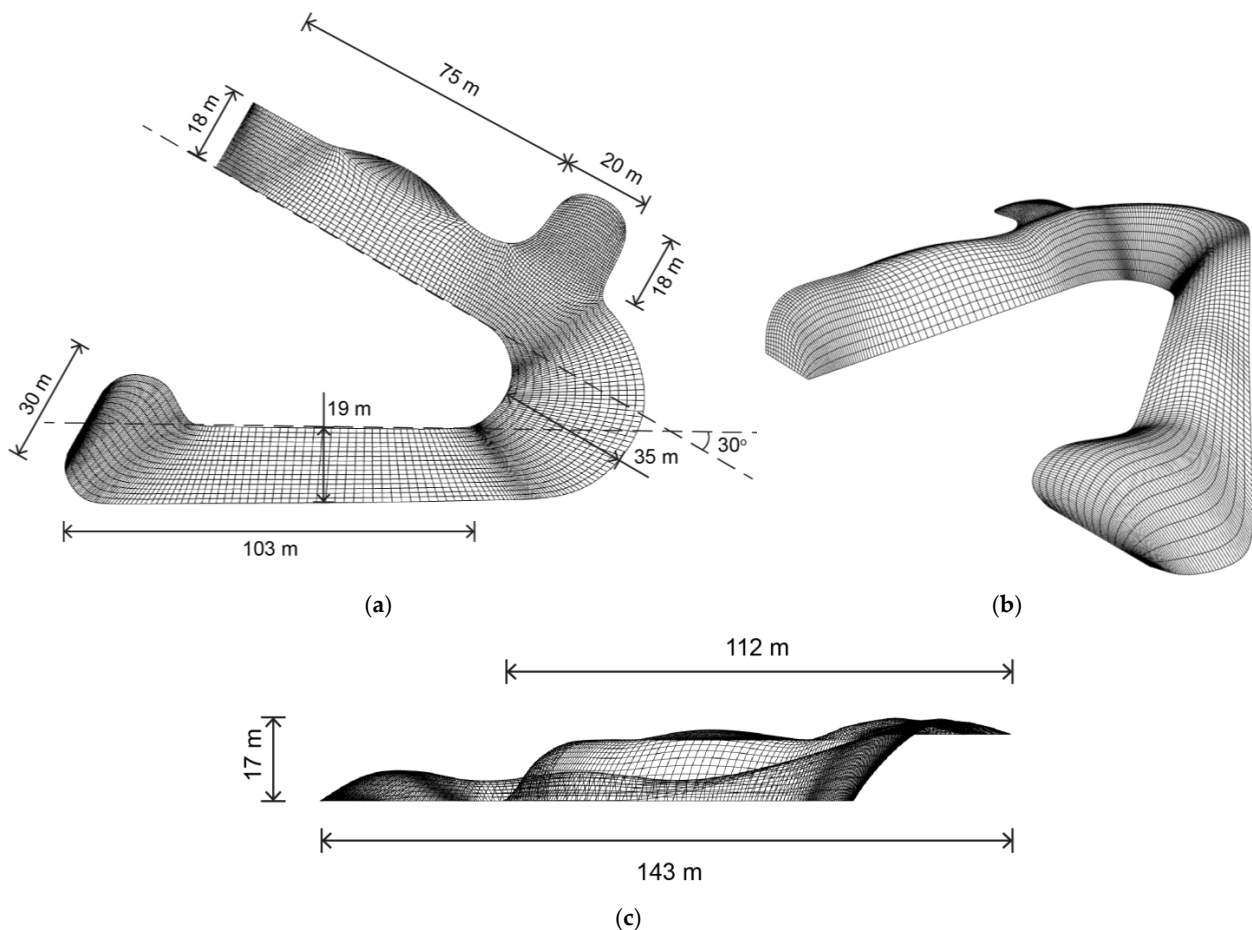


Figure 37. Schematic design of the Chadstone Model: (a) Plan view; (b) Isometric view; (c) Elevation view.

2.4.3. Initial Modelling in Rhino 7

For complicated curved surface, it could be difficult to use Grasshopper to generate the model directly. Therefore, by using the SubD (Subdivision Surface Modelling) function, it

can be easier to manipulate the surface shapes. By editing the control points and structural lines on the SubD plane, the curved shape can be modelled directly. This feature provides more flexibility in complex surface modelling.

In this case, first, referring to the plan and section drawing of the case, a general shape can be created using the “Create SubD plane” function and moving the edges of the planes to the desired positions, as shown in Figure 38. There are two display modes, which are flat and smooth. The modes can be changed by “Tab” key. It can be beneficial to the SubD surface adjustment.

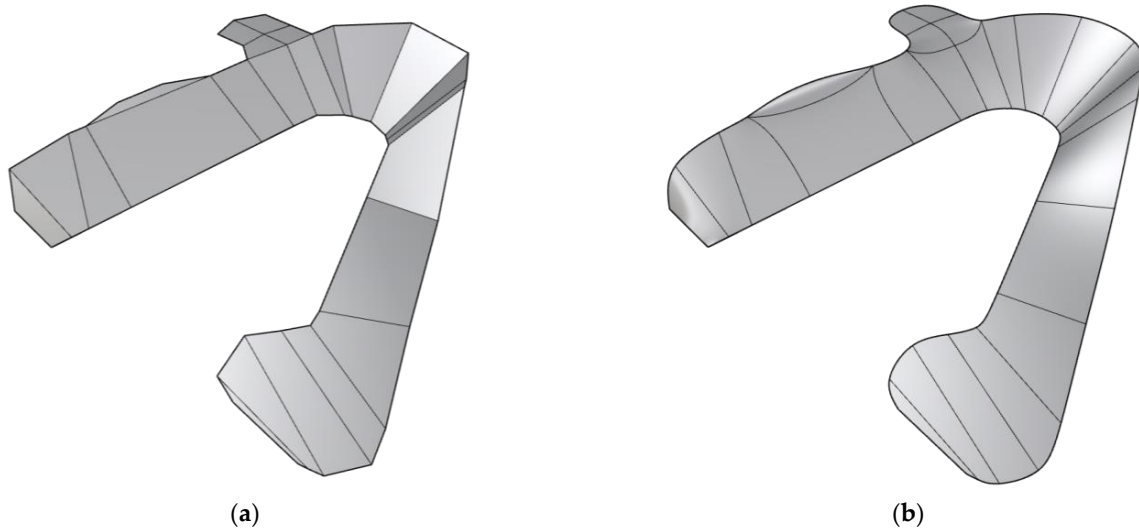


Figure 38. General shape of the Chadstone model: (a) Flat display mode; (b) Smooth display mode.

Then, by adding more structural lines, the model can be adjusted with higher accuracy. The finalised SubD model is shown in Figure 39.

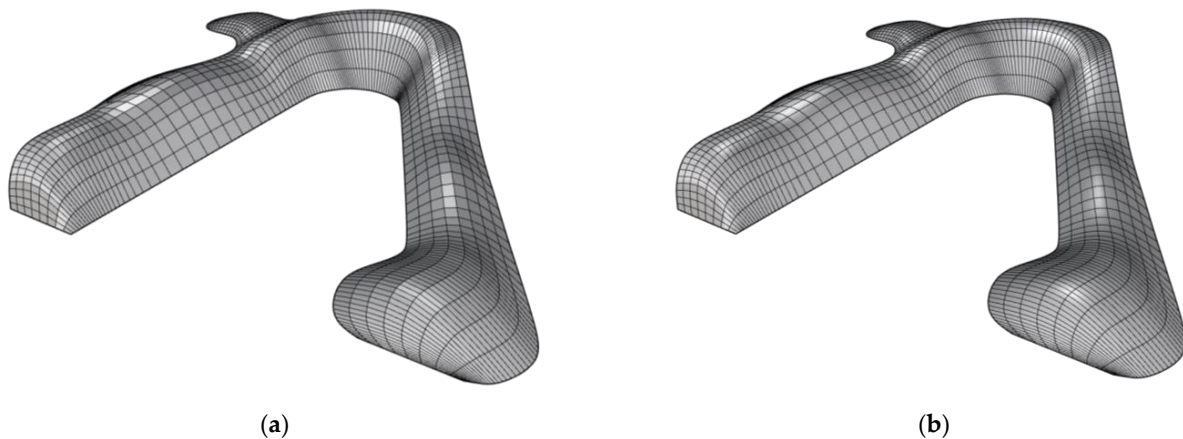


Figure 39. Finalised Shape of Chadstone Model: (a) Flat display mode; (b) Smooth display mode.

2.4.4. Convert the SubD Model to Mesh in Grasshopper

In order to extract the wireframe of this model, it should be converted to mesh surface. This can be realised in Grasshopper. The procedure is shown in Figure 40.

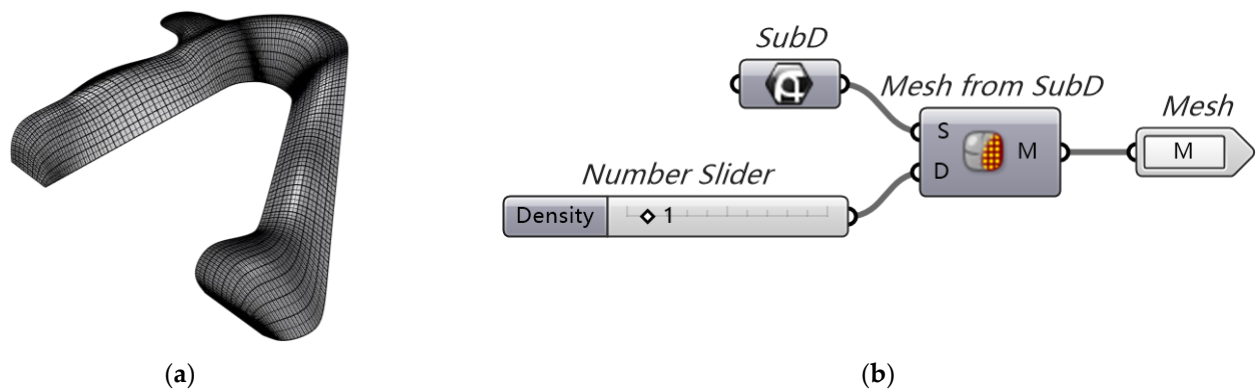


Figure 40. Chadstone model converted from SubD surface to a Mesh surface: (a) Mesh; (b) Grasshopper container.

2.4.5. Convert the Mesh Model to Subdivided Surfaces

To obtain the wireframe model, the mesh surfaces should be subdivided and converted to geometry surfaces based on the structure line. Then, the edges of the surfaces can be extracted to form a wireframe. The geometry surfaces can be created by connecting four known points, obtained from the mesh surface. Thus, the mesh model should be deconstructed and the vertices and faces parameters extracted. The vertices are the intersection of the structural lines, and the faces are the surrounding surfaces. The detailed procedure is shown in Figure 41.

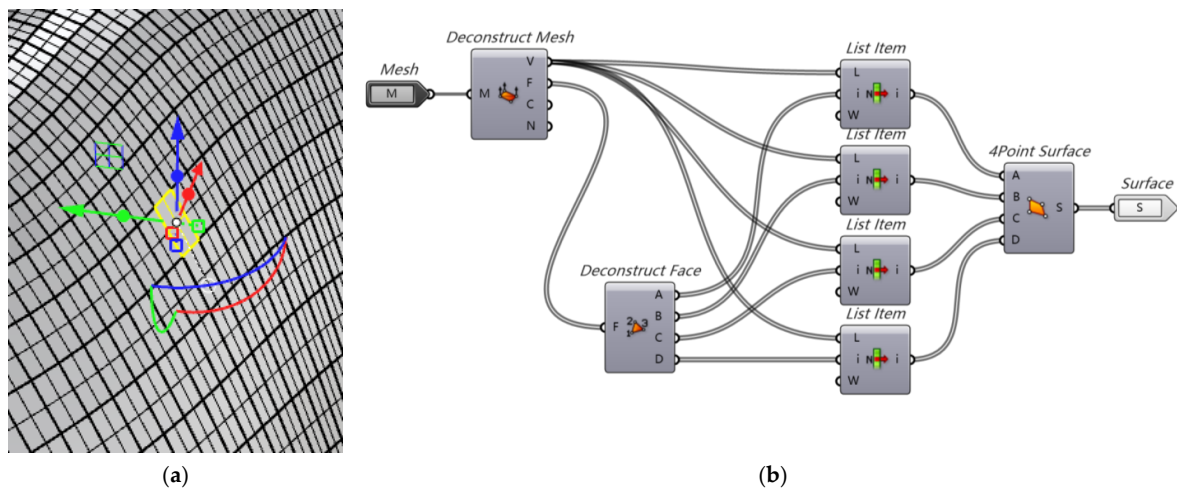


Figure 41. Convert from mesh to subdivided surfaces: (a) Model divided into smaller surfaces; (b) Grasshopper container.

2.4.6. Extract Wireframe from the Surfaces and Clean the Model

As shown in Figure 42, the edges of the subdivided surfaces are extracted and used to form a wireframe.

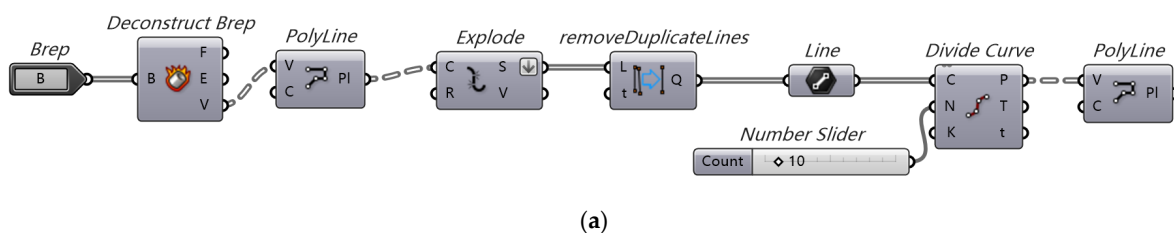
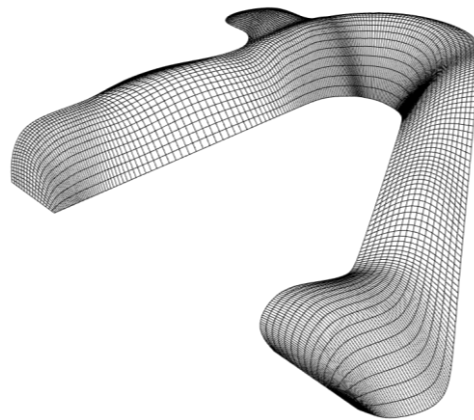


Figure 42. Cont.



(b)

Figure 42. Wireframe extraction and model cleaning: (a) Grasshopper container outlining the modelling procedure; (b) Resultant wireframe model.

2.5. CAD Model of a Light Rail Station in The Hague (Rhino 7)

The central station in The Hague has a light rail station located outside the main building. Its cross-section is elliptical in shape, roughly 16 m in length along its major axis, and 12 m in length along its minor axis. The total structure is approximately 75 m long, with the last 12.5 m rounded to a point. The façade is lined with glass, with steel members crossing diagonally across its face. The live structure has a section of glass cut away from the centre of the structure, but for the purpose of simplification, the entire structure is considered to have glass panels covering it. The final Rhino 7 model is shown in Figure 43.

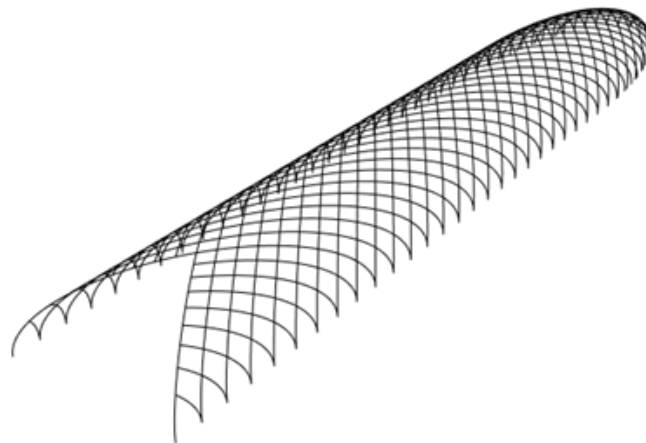


Figure 43. Entire light rail central station in The Hague.

Process of Creating the Rhino 7 Model Using Grasshopper

This section is a step-by-step process on creating the Grasshopper script that creates the structure shown in Figure 43. The entire script is shown in Figure 44.

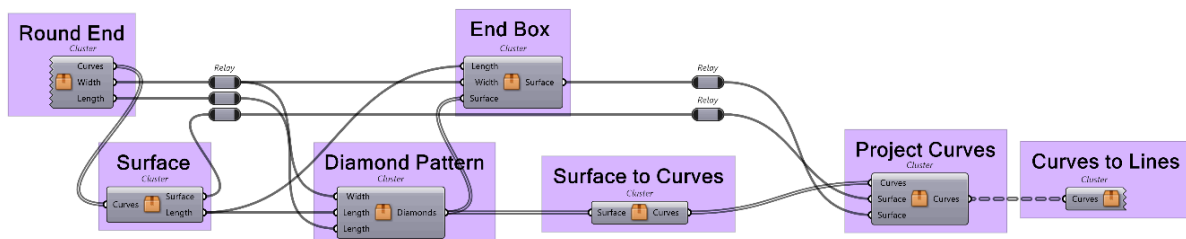


Figure 44. Entire The Hague light rail script.

The first step is creating the rounded end of the station. The container Round End, shown in Figure 45, does this by first creating a pair of ellipses to define the cross-section, grouped under Cross-Section. The length and width are made an output for later use. A line from the origin to the end of the ellipses is created using the Construct point and Line functions. Along this line, a number of planes are created with the Prep Frames function, controlled by a number slider. The container Intersection Points takes the two ellipses, defining the cross-section and the planes as inputs and outputs points correlating to where on these planes the ellipses intersect; the result can be seen in Figure 46. These points are used to create a series of ellipses that round to a point at the end; this can be seen in Figure 47.

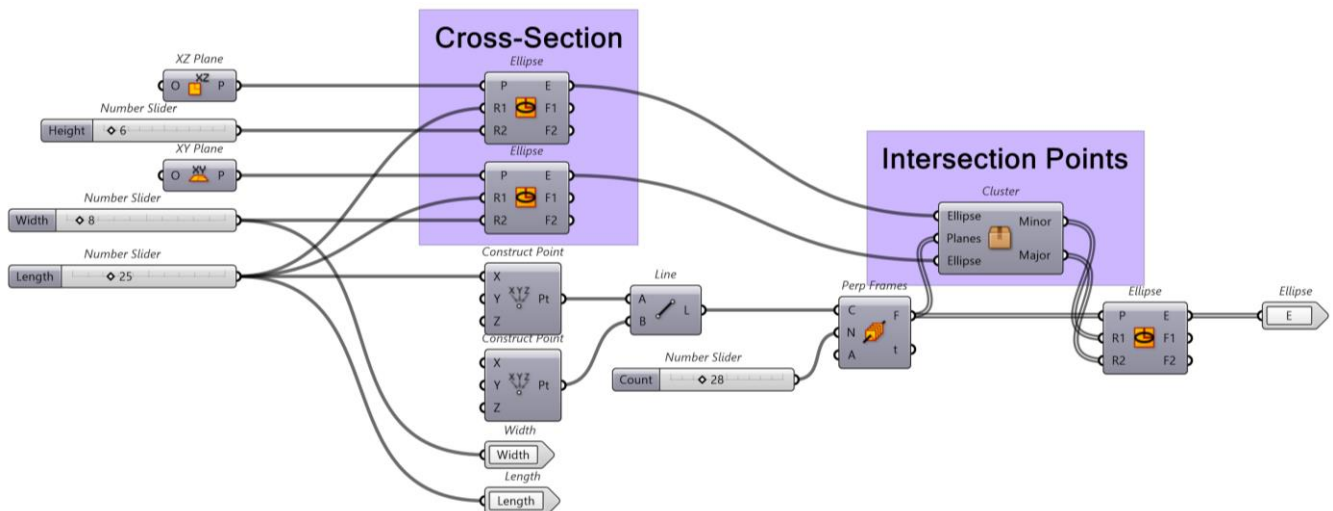


Figure 45. Round End container.

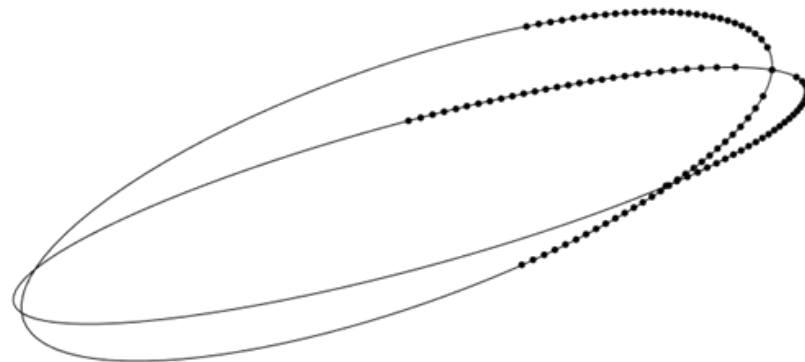


Figure 46. Intersection Points container.

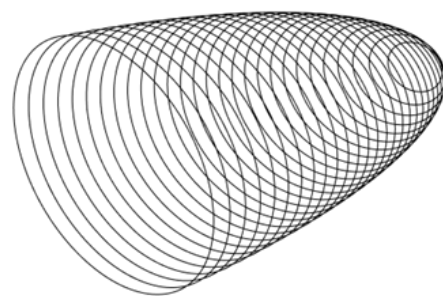


Figure 47. Resultant series of ellipses, rounding to a point from Intersection Points.

The Intersection Points container, shown in Figure 48, uses the Curve | curve function to identify where along the two elliptical curves the plane intersects. These points are then

deconstructed, where upon the Z coordinates become the minor axis lengths, and the Y coordinates become the major axis lengths. These lengths are made positive, sorted, and any duplicates deleted with the use of the Absolut and Create Set functions.

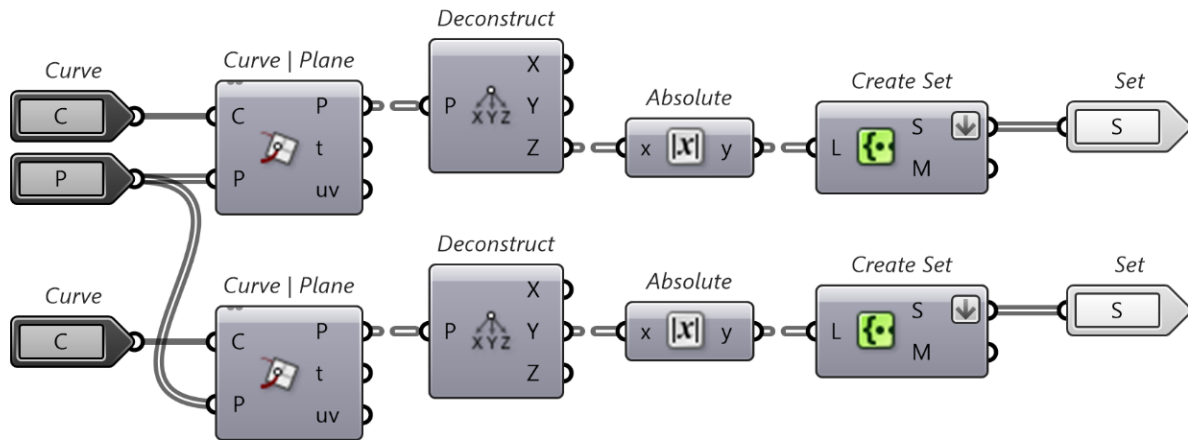


Figure 48. Intersection Points container.

The curves outputted from Round End are imported into the Surface container, shown in Figure 49, where upon the largest curve is extruded along a vector 65 m in length. All the curves are lofted using the Loft function, which essentially creates a surface connecting the curves together. The resultant curves are merged and joined with Merge and Brep Join. This container outputs the resultant surface, along with the length of the extrude. The final product can be seen in Figure 50.

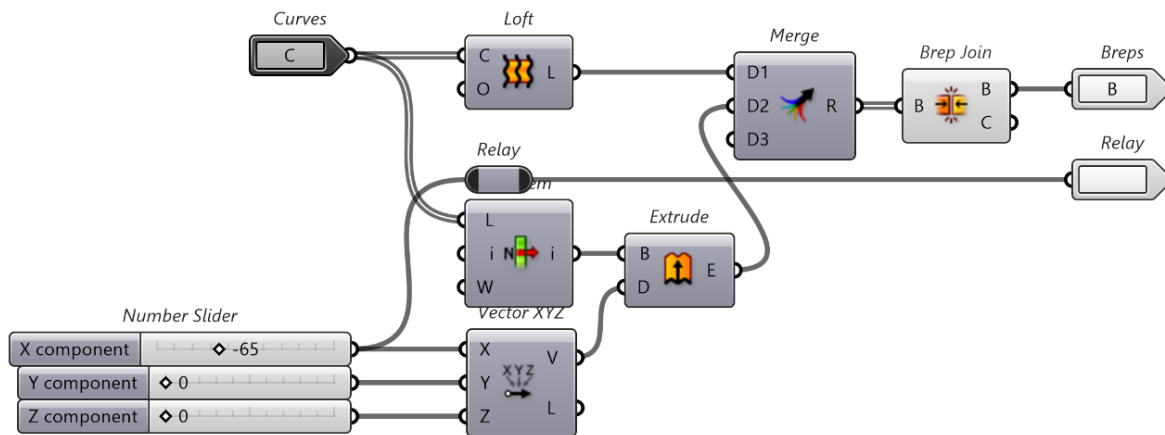


Figure 49. Surface container. Note that the List Item function extracts the last index.



Figure 50. Resultant surface from the Surface container.

The Diamond Pattern container, shown in Figure 51, creates a cross pattern of curves using the lengths of the round end. The extruded ellipse length and the width of the ellipses are used to define a planar surface in the XY plane. The Plane Surface function constructs this planar surface, with the domain defined by the Construct Domain function. Note that the asterisk in Construct Domain indicates a transformed input, in this case, the flipping the sign of the width. The surface is then used to create the pattern of diamonds using the Diamond Panels function. It should be noted that Diamond Panels is a function of the LunchBox plugin. This container outputs a series of surfaces, each defining a diamond panel. The output of all these diamonds can be seen in Figure 52.

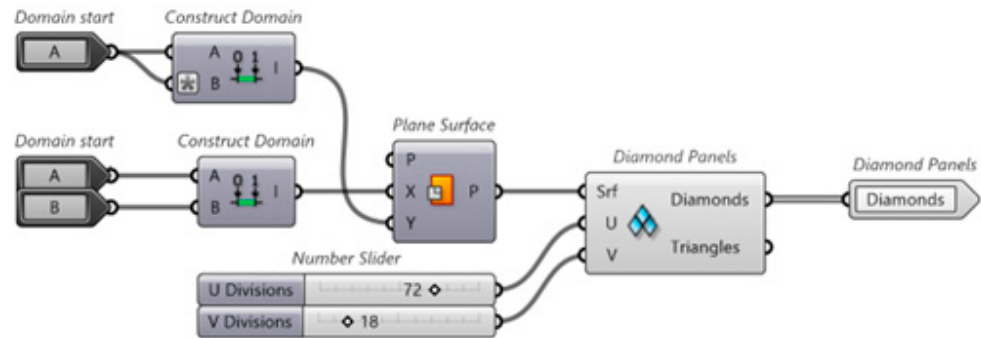


Figure 51. Diamond Pattern container. Note that the Diamond Panels is a function of the LunchBox plugin.

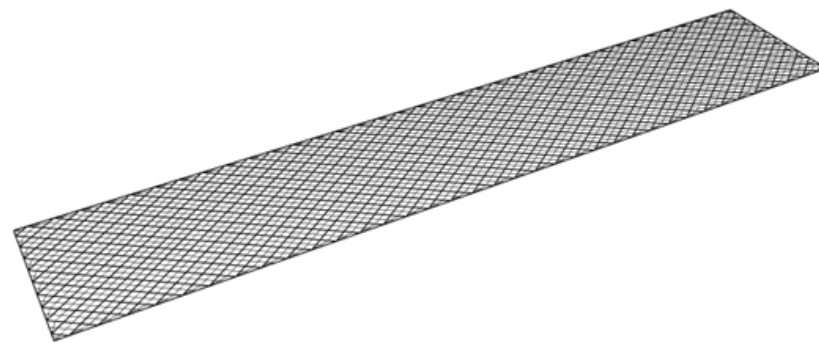


Figure 52. Diamond Pattern container output.

To create the cut out at the end of the light rail station, the length, width, and all the surfaces of the diamond pattern are imported into the End Box container, shown in Figure 53. The End Box container first locates a point and two lines at the end of the diamond pattern using the Point and direction subcontainer.



Figure 53. End Box container, responsible for creating the end shape of the model. Note that it is solely made up of subcontainers, namely, Point and Direction, 2 Surfaces, and Closed Surface.

The Point and Direction subcontainer, shown in Figure 54, works by first identifying three points at the end of the diamond pattern using the List item and Surface Points functions. From Figure 55, the distance between the red and blue points is calculated with the Distance function. This distance is used to move the yellow point to where the orange point is, using the construct point, deconstruct, and addition functions. The Deconstruct, Construct Point, and Line functions are used to create the pink lines from the orange, blue,

and green points. Since the diamond pattern is symmetric about the Y axis, the blue point can have its Y coordinate flipped to create the second pink line using the orange point.

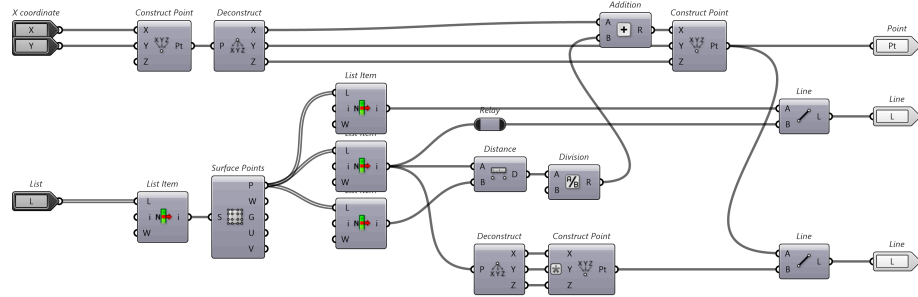


Figure 54. Point and Direction subcontainer.

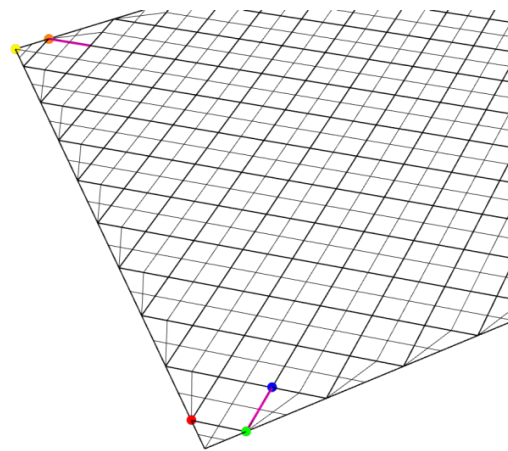


Figure 55. Diagram of diamond pattern in Point and Direction container, where the yellow, orange, red, green, and blue points are used to create the pink lines.

The point and lines are then exported to the 2 Surfaces subcontainer, which creates two surfaces that intersect on the diamond pattern where the two lines would intersect, shown in Figure 56. It accomplishes this by first identifying the point of intersection with the Line | line function, then deconstructing this point into its constituent coordinates to create a line perpendicular to the diamond pattern at the point of intersection. This line, along with the two lines imported from Point and Direction, are used in the Line + Line function to create two planes. These planes are then used by the Plane Surface function to create the surfaces, with a major and minor axis domain larger than that of the light rail station structure. Figure 57 shows the entire subcontainer in Grasshopper.

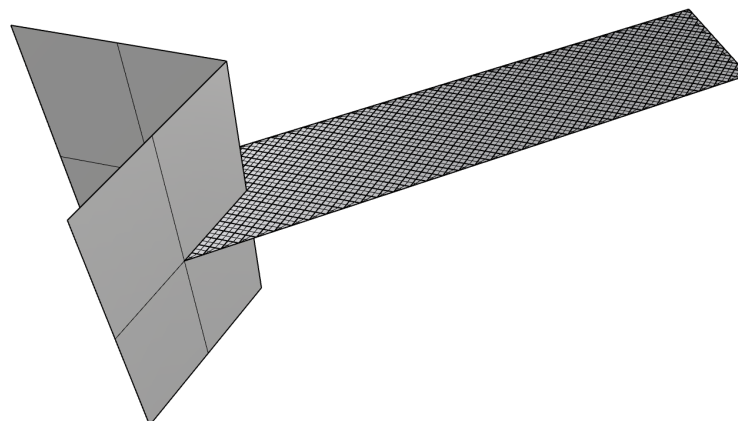


Figure 56. The 2 surfaces container output.

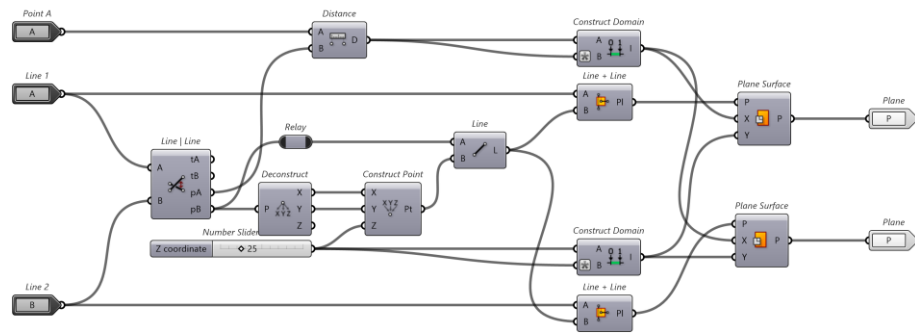


Figure 57. The 2 Surfaces subcontainer.

The two surfaces are exported to the Closed Surface subcontainer, shown in Figure 58, which creates an enclosed surface with the two surfaces; the result can be seen in Figure 59. It achieves this by extracting the corner points of each surface with the Surface Points function and then selecting the correct points with the List Item function to be used in the 4Point Surface function, which creates a surface from four points. The two old surfaces and the new surface at the back are merged and joined together with the Merge and Brep Join functions. Finally, the Cap Holes function creates a surface at the top and bottom to enclose the entire surface.

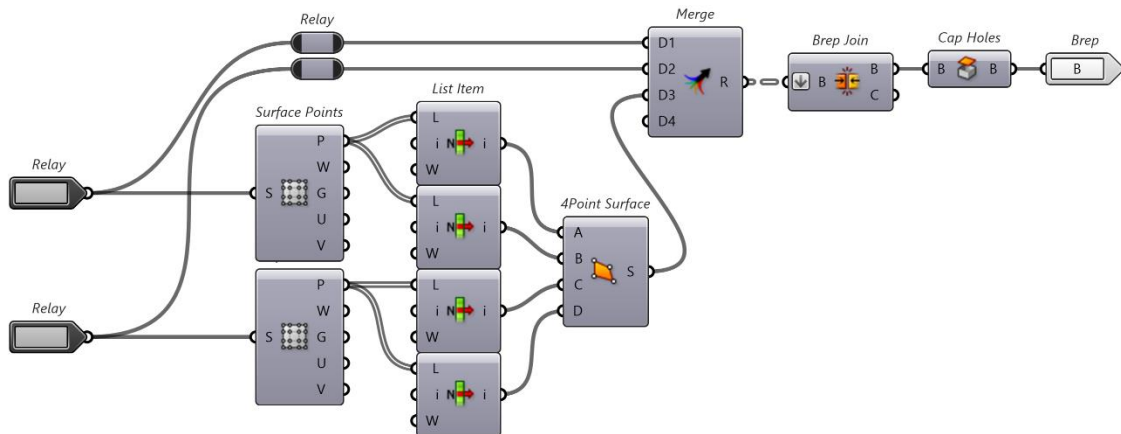


Figure 58. Closed Surfaces container. Note that the down arrow indicates that the input has been flattened.

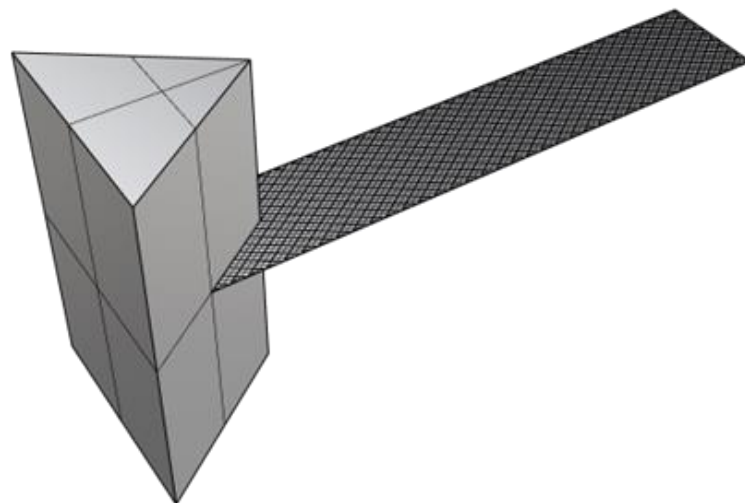


Figure 59. Results from Closed Surfaces container.

The surfaces from Diamond Pattern are then exported to the Surface to Curves container, shown in Figure 60, to extract their edge curves. It does this by converting all the surfaces to curves with the Brep wireframe function, extracting the midpoint of each curve using Point on Curve, then creating a key list by culling all duplicate points from the midpoints list using Cull Duplicates. The key list is then used by List Item to extract all non-duplicate curves. The result is shown in Figure 61.

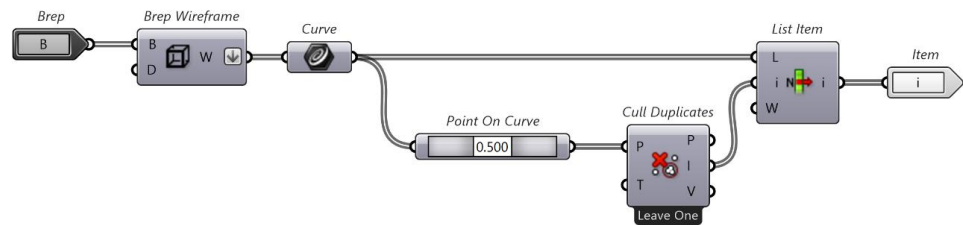


Figure 60. Surface to Curves container. Note that the down arrow implies that the output list has been flattened.

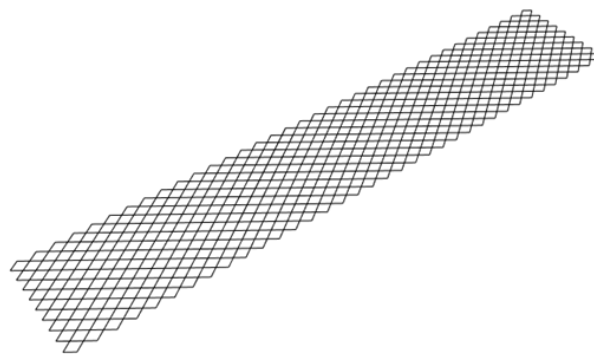


Figure 61. Surface to Curves output.

The diamond pattern, end box surface, and the surface of the light rail station are imported into the Project Curves container. The Project Curves container, shown in Figure 62, first creates a big box using the Construct Point and Box 2Pt functions, which create a point and a rectangular prism, respectively, from two points. The Trim Solid function is used to trim the light rail station surface with the end box and rectangular prism just created. The resultant surface can be seen in Figure 63. The Project function is then used to project the curves from the diamond pattern onto the surface. The results are shown in Figure 64.

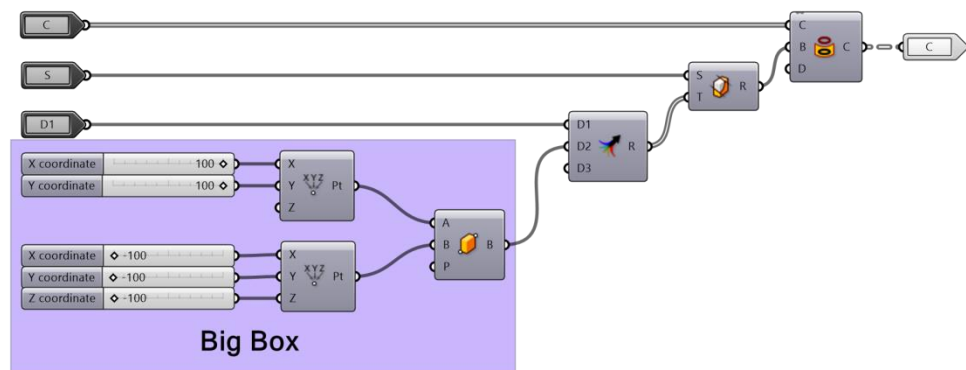


Figure 62. Project Curves container.



Figure 63. Trimmed surface approximating the light rail station.

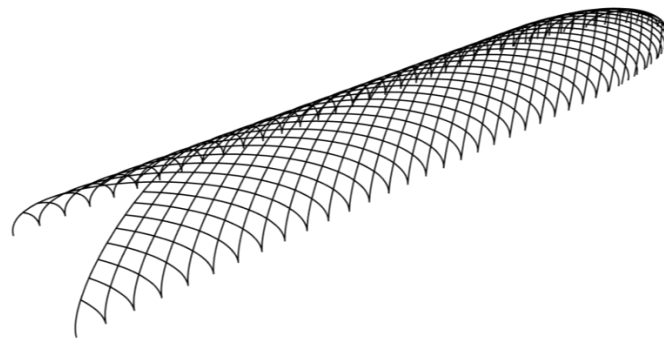


Figure 64. Project Curves result.

The curves shown in Figure 64 are imported to the Curves to Lines container, shown in Figure 65, where they are divided into smaller segments with the Divide Curve, Polyline, and Explode functions. The number of segments is controlled by a number slider. Any duplicates are removed with the removeDuplicateLines function.

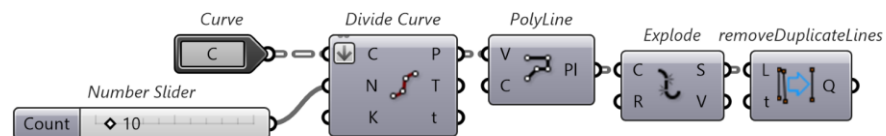


Figure 65. Curves to Lines container. Note the down arrow that indicates the list has been flattened.

3. Exporting the Rhino 7 Models to Strand7

Once the structure has been modelled in Rhino 7, separate the model segments into preferred groups. It will be too difficult to separate beams into groups once inside Strand7, which is why it is accomplished in Rhino 7. An easy way to separate beams into groups would be to bake each group in Grasshopper to a new layer in Rhino 7. Using the Kazakhstan Pavilion as an example, first create a layer for each group (in this case 3); Figure 66 gives an example.

For each layer, bake a different group into it, as shown in Figure 67; each colour represents a different layer and a different beam grouping.

In Strand7, each layer will be a different group, and each colour will be a different property. To export to Strand7, simply save the file as a dxf file type. In Strand7, in a new file, select file > import > your file and make sure to select 'Import Layers as Groups' and 'Import Colours as Properties'. Now the model should be in Strand7 separated by group and properties; Figure 68 gives an example.

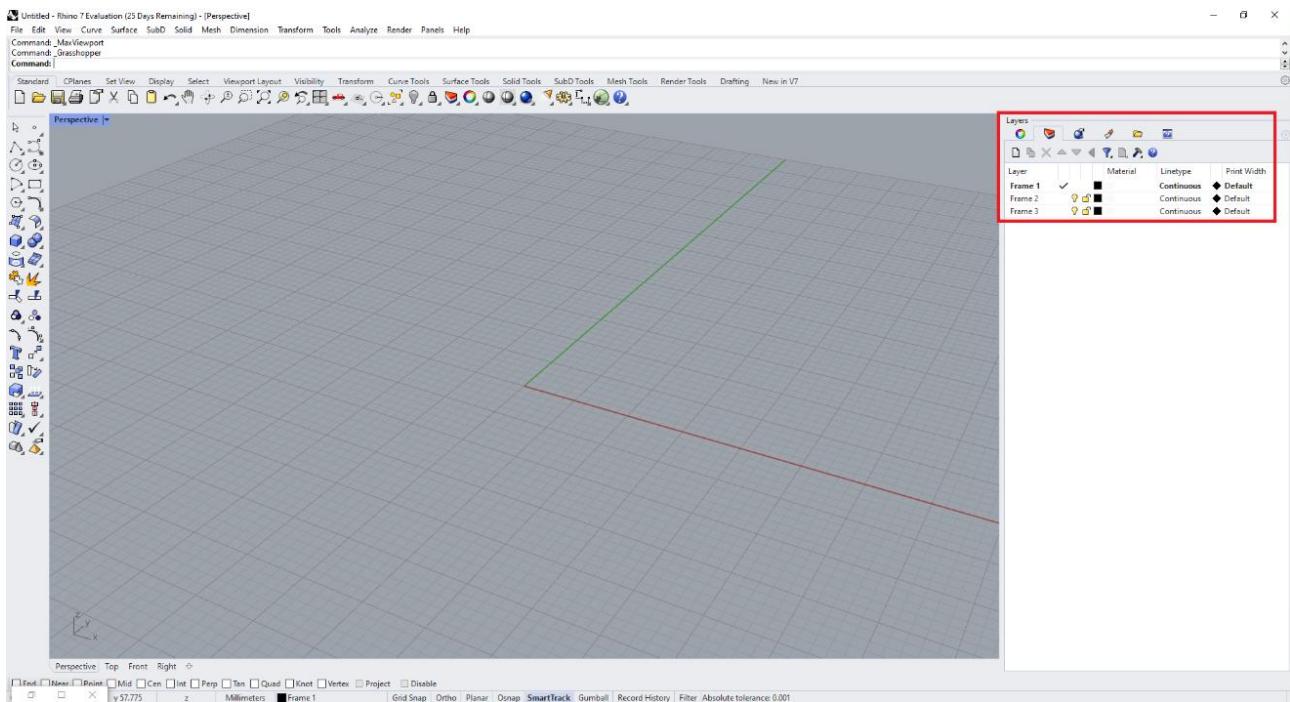


Figure 66. Rhino 7 user interface, with the layers tab highlighted. The red box highlights where in Rhino 7 new layers can be created and selected.

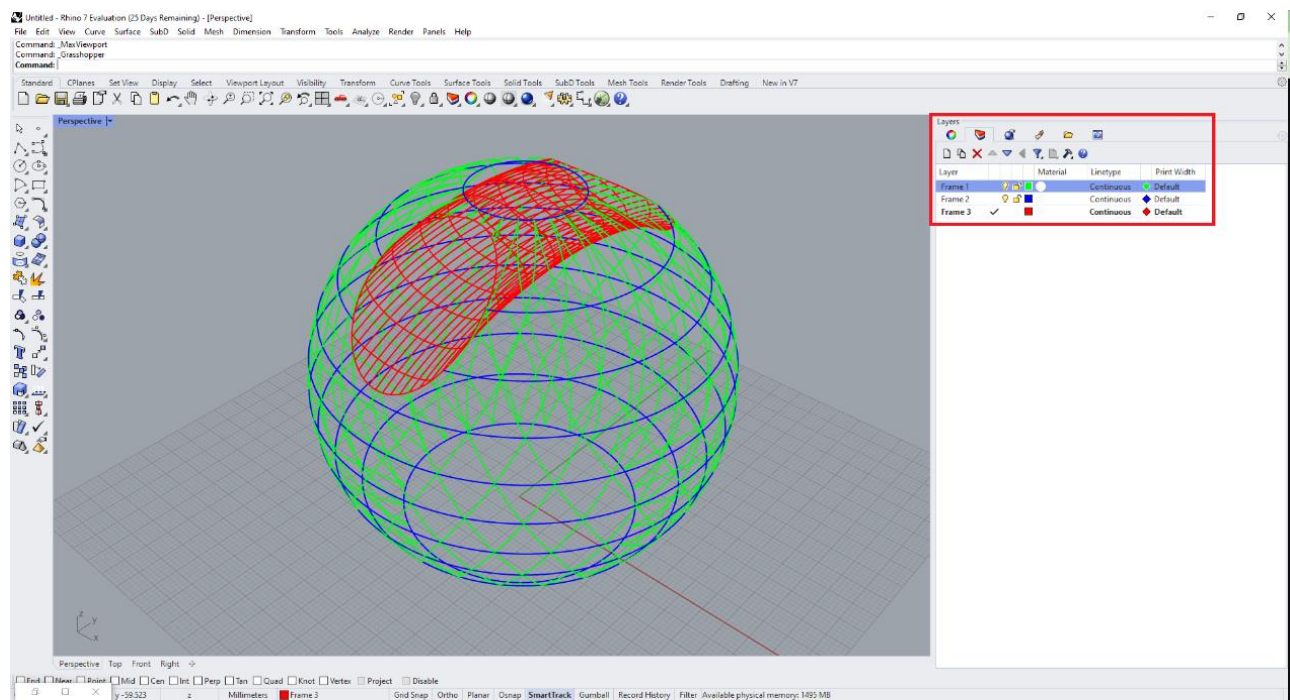


Figure 67. Rhino 7 user interface showcasing the layer tab using the Kazakhstan Pavilion as an example. Note that the beams will bake into whichever layer is selected at the time.

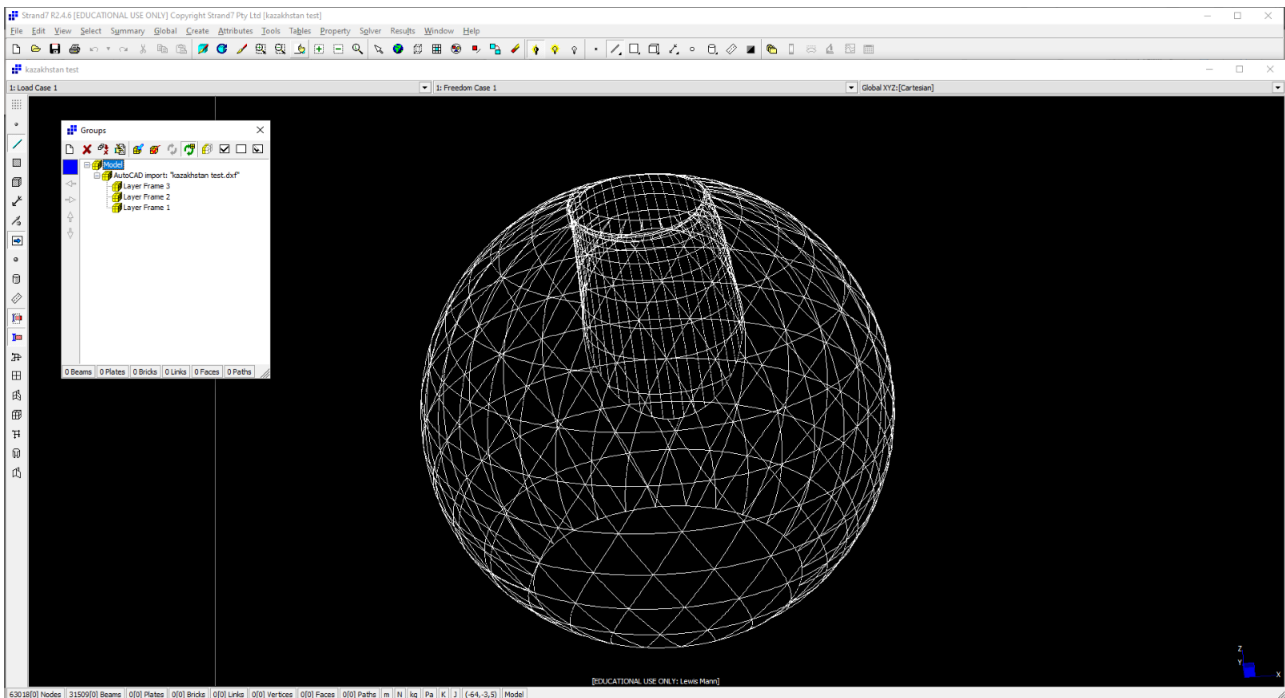


Figure 68. Strand7 model of Kazakhstan Pavilion imported from Rhino 7.

Now, this is a very basic way to export to Strand7; it does not consider boundary properties or local beam axis orientation, which will be discussed later in this paper. For some models, selecting and allocating the boundaries conditions will be too difficult. Indeed, some boundary beams may be unnecessary to import, as they are restricted on both ends by constraints.

Using the Chadstone mall as an example, this section will show how to define the boundary condition for irregular complex structures in Strand7. There is some extra Grasshopper script that is required to output the boundary nodes and/or boundary beams. The scrip shown in Figure 69 will output the Chadstone beam frame, without the boundary beams, alongside the points where the beams meet the boundary.

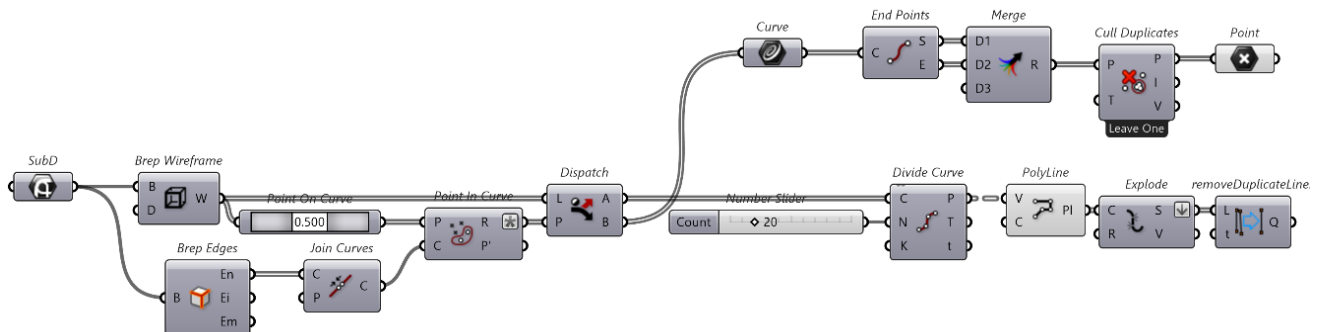


Figure 69. Chadstone Boundary Grasshopper script.

Starting with the SubD surface of the Chadstone mall, the edges are extracted with Brep Edges, which are then joined together and used to find all the points that coincide with it. Brep wireframe and Point on Curve are used to extract a point on each curve to use to check if said curve is on the edge of the surface or not. Point In Curve outputs a list of integers for every point, which indicate if the point is inside, outside, or coincides with the edge curves. A key can be created with this list and used in Dispatch to separate out the curves that are on the edge and that are not. The curves not on the edge can be processed as normal, being segmented up and exploded. The edge curves are not exported

to Strand7, but are instead used to find the free ends of all the other curves. Since the free ends of all over curves are at either the start or end of the edge curves, these points are extracted with End Points, merged, and any duplicates culled. These points can now be exported to Strand7; Figure 70 gives an example of boundary points.

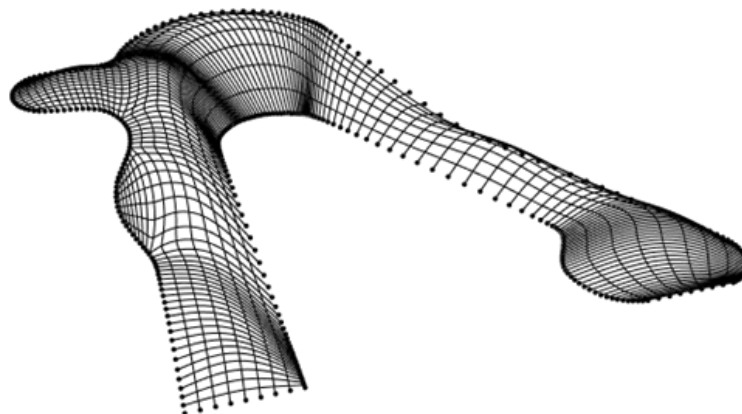


Figure 70. Chadstone mall in Rhino 7 with edge nodes.

It is important to note that the boundary nodes/points must be imported into Strand7 first and have their attributes set before importing the rest of the model. Finally, once the model is in Strand7, be sure to clean it by selecting tools > clean > mesh, and leave all the default options. Figure 71 shows the edge points in Chadstone being assigned restraints.

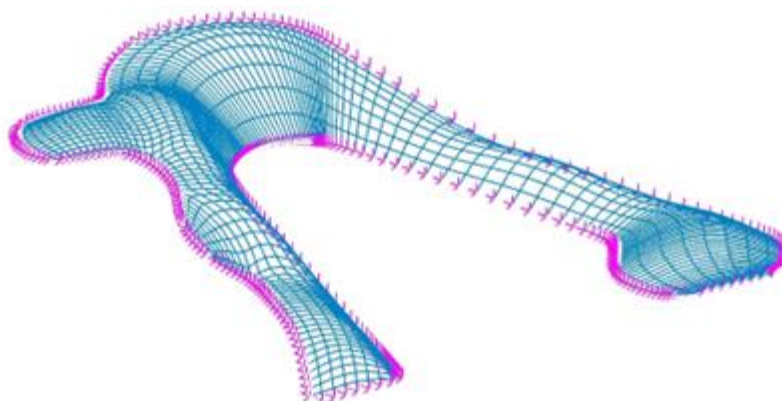


Figure 71. Chadstone mall model in Strand7 with restricted boundary nodes.

4. Numerical Analysis of All Models (Strand7)

4.1. Load Cases

Each model is expected to experience three types of loads, which include dead load, live load, and wind load, according to AS1170.1 [61]. It is assumed that in each model, roof access is unavailable to users of the structure.

4.1.1. Dead Load, G

Dead load accounts for all steel members that provide structural support. For simplification, the glass panels are accounted for in the live load. In all models, the density of each steel member is 7850 kg/m^3 . Gravity is acting in the Z direction of each Strand7 model, with an acceleration of -9.80665 m/s^2 .

4.1.2. Live Load, Q

The live load in each model accounts for the self-weight of the glass panels. It is assumed that the glass panels apply a face pressure of 0.25 kPa on the steel structure of

each model, referring to AS1170.1 [61]. For each model, the total area and total length of supporting beams were calculated from Grasshopper. These would then be used to calculate the effective live UDL on the members supporting the glass façade. Table 1 summarises the total areas and lengths of each model and the effective live UDL.

Table 1. Summary of Live UDL for each model.

Model	Total Area (m ²)	Total Support Beam Length (m)	Tributary Area (m ² /m)	Live UDL (kN/m)
Chadstone	7086	7083	1.000	0.250
Moynihan	474	939	0.505	0.126
Kazakhstan Sphere	18,131	4686	3.869	0.967
Kazakhstan Tube	2980	2890	1.031	0.258
The Hague	1758	2050	0.858	0.214
Phoenix	6779	5978	1.134	0.283

4.1.3. Wind Load, W

The wind load applied to the models was calculated in accordance with AS1170.2 [62]. For each model, the design wind speed was assumed to be 30 m/s, except for the Chadstone Shopping Centre, which was assumed to survive a 1 in 100-year wind speed event. Each model had simplifications to its geometry to comply with AS1170.2 [62]. It is assumed that the glass on the surface is smooth enough to ignore the effects of wind friction.

Note that for some models, the UDL acts normal to the beams, whereas in others, it acts at an angle along the global axis. This is because for some models, it was not possible to maintain consistent orientation of the beam's local axis. This is most likely due to file transferring.

Phoenix International Media Center

The Phoenix Center in Beijing was assumed to have a dome-like structure, with the central section having a negative wind action applied to it (away from the roof). The pressure coefficients were taken from Table A.3 from AS1170.2 [62]. Like the Kazakhstan Pavilion, the central sides were assumed to have the same negative wind action imposed upon them. It is assumed that the roof "springs from the ground" and that its r/d ratio is 0.5. Figure 72 shows the wind loads applied in Strand7.

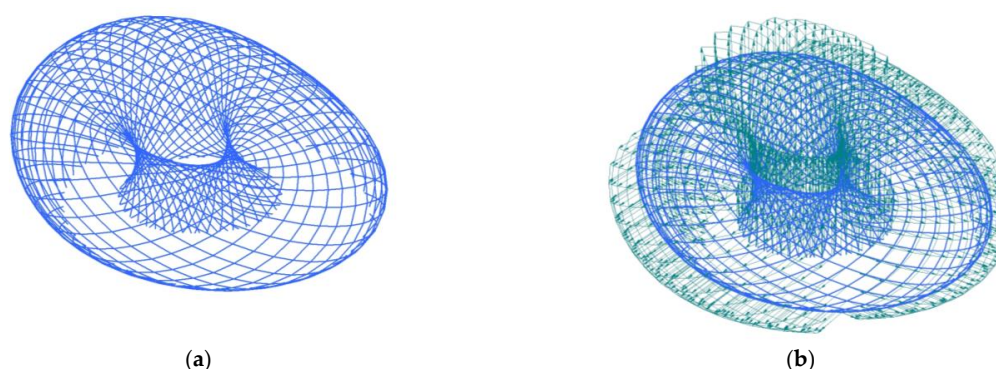


Figure 72. (a) Phoenix International Media Center Strand7 model with straight beams; (b) Phoenix International Media Center Strand7 model with applied critical wind load to straight beams.

Kazakhstan Pavilion and Science Museum

The Kazakhstan Pavilion was simplified to a sphere. The external pressure coefficients were taken from Table A.3 from AS1170.2 [62], the assumption being that like section 7.11 of the Eurocode [63], the central half of the roof applies to the central sides. It is assumed that the roof "springs from ground" and that its r/d ratio is 0.5. Frictional wind loads were applied to the tube section of the model. Figure 73 shows the wind loads applied in Strand7.

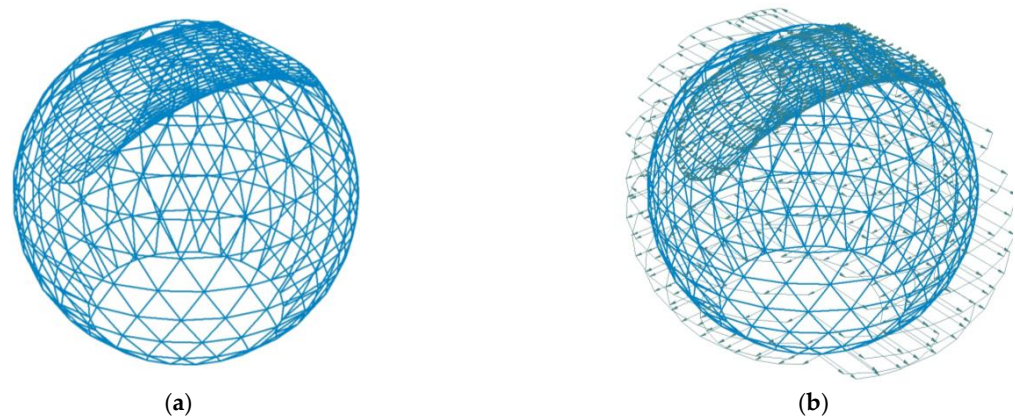


Figure 73. (a) Kazakhstan Pavilion and Science Museum Strand7 model with straight beams; (b) Kazakhstan Pavilion and Science Museum Strand7 model with applied critical wind loads.

Moynihan Train Hall

Moynihan Train Hall, although surrounded on all four sides by two stories, was assumed to be that of a gable roof, with each side of the roof being windward or leeward. The external pressure coefficients were taken from Table 5.3(B) and Table 5.3(C), with a height-on-depth ratio of 0.5 from AS1170.2 [62]. Figure 74 shows the wind loads applied in Strand7.

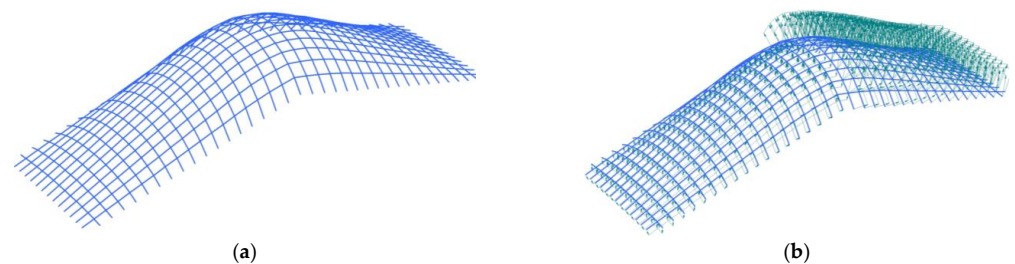


Figure 74. (a) Moynihan Train Hall Strand7 model with straight beams; (b) Moynihan Train Hall Strand7 model with applied critical wind loads.

Chadstone Shopping Centre

The Chadstone shopping mall was assumed to be either entirely crosswind or entirely upwind. The external pressure coefficients were taken from Table 5.3(B) and Table 5.3(C), with an average roof slope of roughly 30 degrees and a height-over-depth ratio of 0.5 from AS1170.2 [62]. Figure 75 shows the wind loads applied in Strand7.

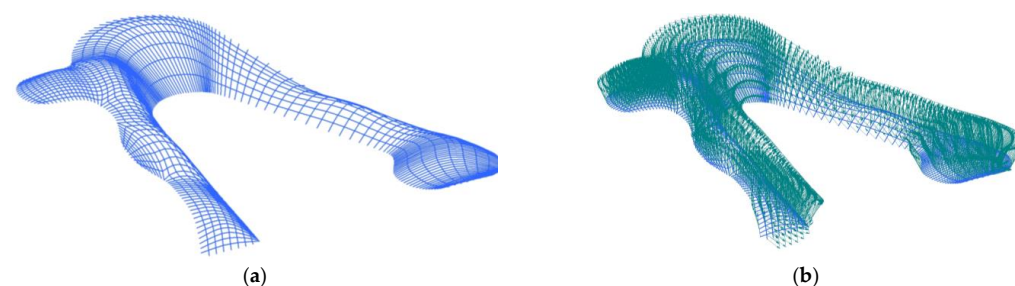


Figure 75. (a) Chadstone Shopping Centre Strand7 model with straight beams; (b) Chadstone Shopping Mall Strand7 Model with applied critical wind loads.

The Hague Central Station Light Rail Station

The Hague light rail station was assumed to be a free-standing roof, as there are large openings for trains and pedestrians to exit the station. The pressure coefficients were taken from Table B.5 of AS1170.2 [62]. It was assumed that it was empty underneath the roof,

with a roof pitch of less than 15 degrees. Figure 76 shows the wind loads applied in Strand7.

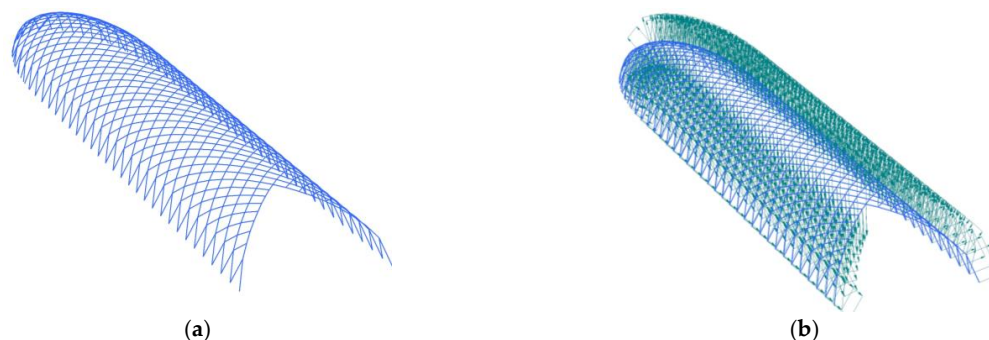


Figure 76. (a) The Hague Central Station light rail station Strand7 model with straight beams; (b) The Hague Central Station light rail station Strand7 model with applied critical wind loads.

4.2. Load Case Combinations

In addition to the load cases described above, the structure of each model is expected to follow load case combinations outlined in AS1170.1 [61]. Since users of these buildings do not have access to the roof, the steel–glass façades are not designed for floor-type activities. Thus, the combination factor (ϕ_c) is zero. The load combinations consider strength limit and serviceability limit states, shown in Table 2.

Table 2. Linear Load Case Combinations.

	Strength Limit State	Serviceability Limit State
Load Combinations	$1.2G + 1.5Q$ $1.35G$ $1.2G + W$	$G + 0.7Q$ $G + 0.7Q + W$

5. Structural Behaviours under Strength Limit State

Each of the five models' performance is analysed under the strength limit state for each load combination case described in Table 2, for both straight and curved member model variations. The total fibre stress and load factor are the main criteria used to evaluate the performance of each model/structure. Total fibre stress is a measurement within Strand7, which indicates the stress experienced by fibres within a beam/column/plate member. The load factor represents the ratio between a structure's ultimate strength limit state and its current loading condition. Strand7 offers several solvers; in this study, linear static and nonlinear static solvers were used to obtain conservative results. In the case of the nonlinear static solver, material and geometric nonlinearities were considered. It was assumed that the material remained isotropic until yield stress, having the same strength in both tension and compression. The yield stress of all members in every model was 350 MPa, under an assumption of grade 350 steel being used. An important assumption made by the Strand7 solvers is that the resultant displacement caused by deformation is relatively small.

Structural behaviour variations between straight and curved members were investigated. The intention is to show how the method proposed in this paper can be used to conduct more in-depth research into curved façade structures. This is the main reason for using nonlinear static solvers, as the nonlinear geometric shape of some of these models is too complex to be estimated by a linear solver.

In addition, the buckling behaviour of each model is investigated by Strand7's linear buckling solver. The non-zero load factor of the first mode to converge is the critical buckling load factor for the structure. This is performed for each load combination case described in Table 2.

5.1. Phoenix International Media Center

The Phoenix International Media Center was modelled in Strand7 with full restraint at its base, with C350LO 457.0x12.7 CHS beam members. The curved modelled has 20 times more nodes along beam paths than the straight model, effectively making curved beam members.

The Phoenix models for both straight and curved members perform well under the strength limit states outlined in AS1170.0 [64], with the fibre stress of members never exceeding the yield limit of 350 MPa. The maximum fibre stress was 112 MPa, experienced by the curved member model under the load combination 1.2G + 1.5Q using nonlinear static analysis. The ultimate load factor was 3.07, experienced by the curved member model under nonlinear static analysis and the load combination 1.2G + 1.5Q. The results are highly dependent on the accuracy of the model, with the straight and curved member model performances deviating as much as nearly 20% under the load condition 1.2G + W.

5.1.1. Load Combination 1.2G + 1.5Q

Table 3 summarises the total fibres stress in beams for both the straight and curved models for both linear and nonlinear analysis, under the load combination 1.2G + 1.5Q, while Table 4 summarises their displacements.

Table 3. Fibre stresses under 1.2G + 1.5Q load combination.

Solver	Maximum Fibre Stress (MPa)		Difference (%)
	Straight Members	Curved Members	
Linear Static	−89.80	−111.80	19.7
Nonlinear Static	−89.98	−112.46	20.0
Nonlinear Static Load Factor	3.87	3.07	20.7

Table 4. Displacements under 1.2G + 1.5Q load combination.

Solver	Straight Member Model Maximum Displacements (mm)			
	D _X	D _Y	D _Z	D _{XYZ}
Linear Static	13.05	14.97	−36.94	37.40
Nonlinear Static	13.09	15.01	−37.07	37.53
Solver	Curved Member Model Maximum Displacements (mm)			
	D _X	D _Y	D _Z	D _{XYZ}
Linear Static	20.99	22.99	−57.69	58.40
Nonlinear Static	21.09	23.07	−58.02	58.73

As shown in Table 3, the maximum fibre stress was 112 MPa, which came from non-linear static analysis of the curved model and was less than the 350 MPa yield limit. The difference in maximum fibre stress experienced by the 2 models was as much as 20 percent, suggesting that the outcome is highly dependent on the accuracy with which the structure is modelled. The maximum displacements in Table 4 are relatively small compared to the span, suggesting that the linear and nonlinear static analysis results are valid with the assumptions made.

Figure 77 depicts the fibre stresses experienced by the members for straight and curved models. It is important to note that the members shown are represented by a line, and thus, the fibre stress of each member cannot be fully shown. The homogeneity of colour mapping suggests that the clockwise and anticlockwise wrapping of the structural members does not significantly contribute to the fibre stress experienced by each member.

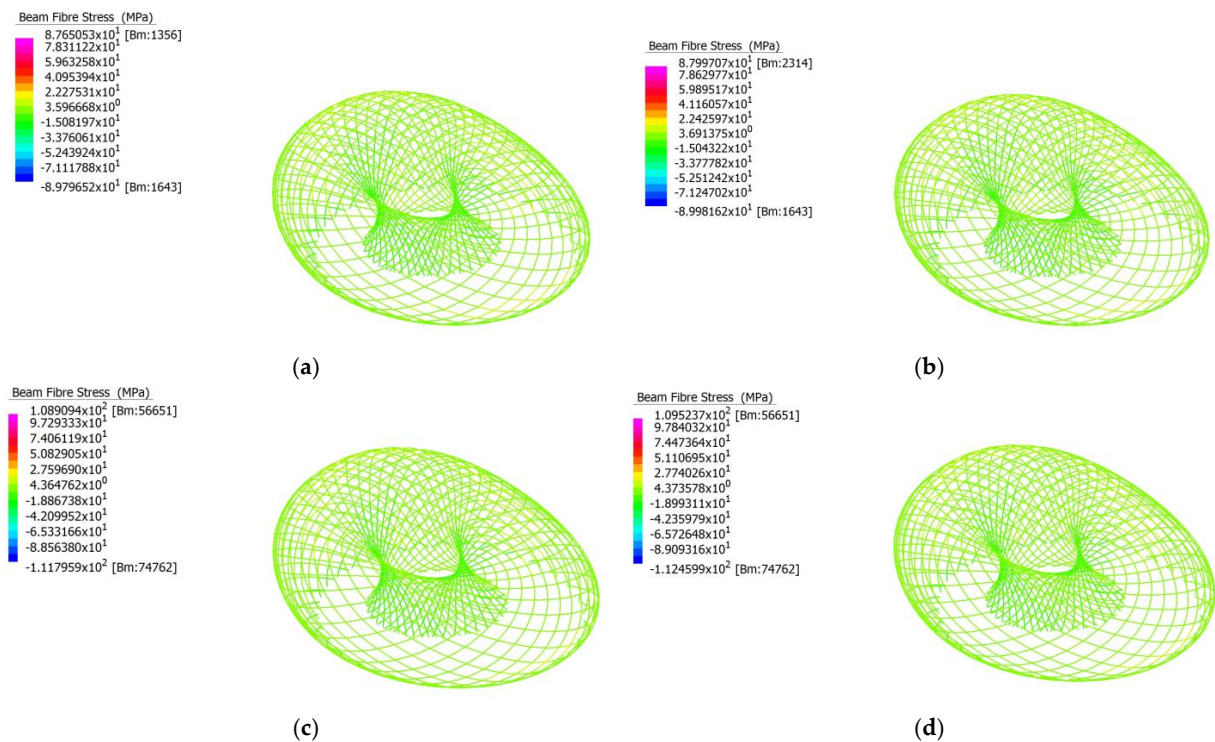


Figure 77. (a) Linear analysis of total fibre stress of straight member model under load combination 1.2G + 1.5Q; (b) Nonlinear analysis of total fibre stress of straight member model under load combination 1.2G + 1.5Q; (c) Linear analysis of total fibre stress of curved member model under load combination 1.2G + 1.5Q; (d) Non-linear analysis of total fibre stress of curved member model under load combination 1.2G + 1.5Q.

Figure 78 depicts the difference in the linear buckling behaviour of the straight and curved models. For the straight model, the exterior members buckle radially outward, most likely as a result of axial and lateral loading due to the geometry of the structure, whereas for the curved model, buckling occurs at the top of the structure, where there should be the least amount of axial force. A possible answer for this is that due to the more accurate modelling, the axial deviation of the applied load nearer the supports is less than that of the straight model, meaning it would require more axial load to buckle, while the top of the structure maintains a similar lateral and axial load path for the members. For both models, the linear buckling failure factor is well above the load factors outlined in Table 3. The maximum load factor for the load combination 1.2G + 1.5Q is therefore 3.07, from nonlinear static analysis of the curved member model.

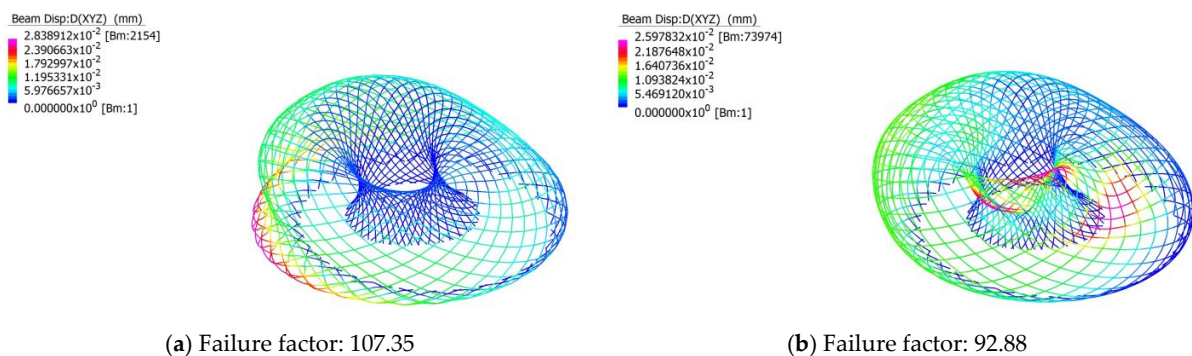


Figure 78. (a) Linear buckling analysis of straight member model under load combination 1.2G + 1.5Q with D_{XYZ} displacement contour; (b) Linear buckling analysis of curved member model under load combination 1.2G + 1.5Q with D_{XYZ} displacement contour.

5.1.2. Load Combination 1.35G

As shown in Table 5, the maximum fibre stress was 100 MPa, which came from non-linear static analysis of the curved model and was less than the 350 MPa yield limit. The difference in maximum fibre stress experienced by the 2 models was as much as 18 percent, which supports the idea that the outcome is highly dependent on the accuracy with which the Phoenix structure is modelled. The maximum displacements in Table 6 are relatively small compared to the span, suggesting that the linear and nonlinear static analysis results are valid with the assumptions made. From Figure 79, there is no significant difference between the clockwise and anticlockwise wrapping of steel members in terms of fibre stress.

Table 5. Fibre stresses under 1.35G load combination.

Solver	Maximum Fibre Stress (MPa)		Difference (%)
	Straight Members	Curved Members	
Linear Static	−81.64	−99.41	17.9
Nonlinear Static	−81.79	−99.94	18.2
Nonlinear Static Load Factor	4.25	3.46	18.6

Table 6. Displacements under 1.35G load combination.

Solver	Straight Member Model Maximum Displacements (mm)			
	D _X	D _Y	D _Z	D _{XYZ}
Linear Static	11.86	13.61	−33.58	34.00
Nonlinear Static	11.90	13.64	−33.69	34.10
Solver	Curved Member Model Maximum Displacements (mm)			
	D _X	D _Y	D _Z	D _{XYZ}
Linear Static	18.67	20.44	−51.30	51.93
Nonlinear Static	18.75	20.51	−51.65	52.19

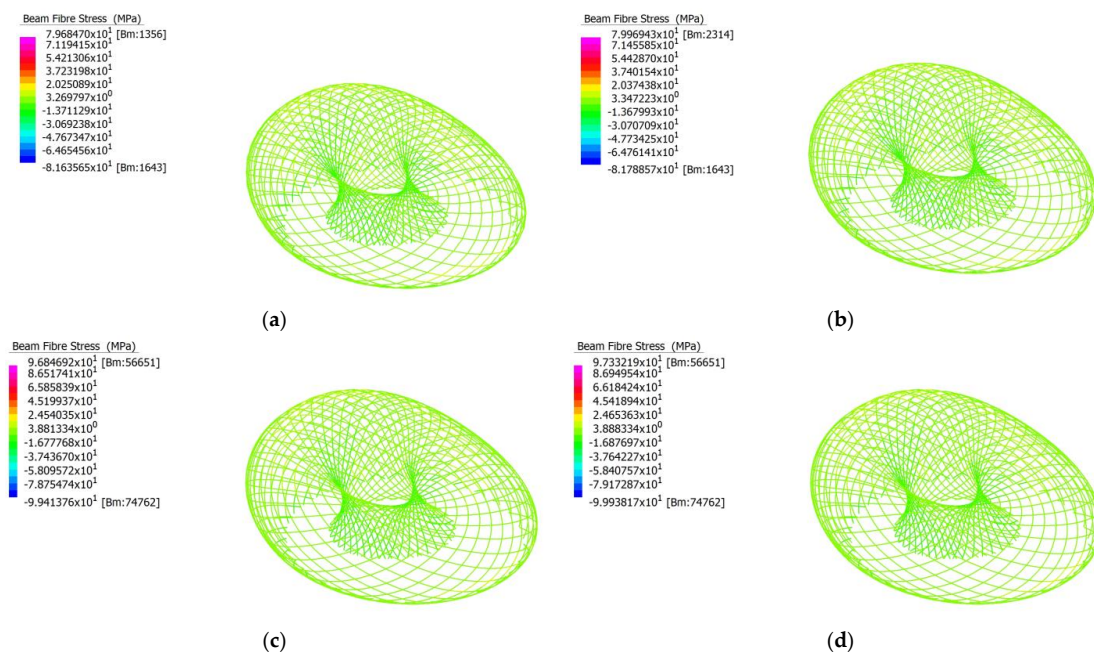


Figure 79. (a) Linear analysis of total fibre stress of straight member model under load combination 1.35G; (b) Nonlinear analysis of total fibre stress of straight member model under load combination 1.35G; (c) Linear analysis of total fibre stress of curved member model under load combination 1.35G; (d) Nonlinear analysis of total fibre stress of curved member model under load combination 1.35G.

Figure 80 depicts the difference in linear buckling behaviour of straight and curved models. As with the load combination 1.2G + 1.5Q, the straight model experiences local buckling near the base of the structure, most likely as a result of high axial and lateral loading.

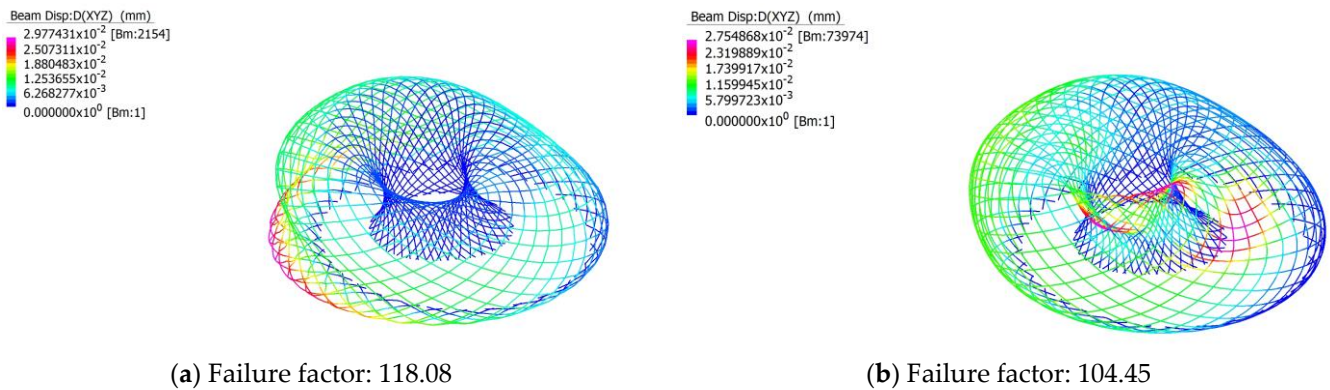


Figure 80. (a) Linear buckling analysis of the straight member model under load combination 1.35G with D_{XYZ} displacement contour; (b) Linear buckling analysis of the curved member model under load combination 1.35G with D_{XYZ} displacement contour.

For the curved model, however, buckling occurs at the top of the structure, where there should be the least amount of axial force. For both models, the linear buckling failure factor is well above the load factors outlined in Table 5. The maximum load factor for the load combination 1.35G is therefore 3.46, from nonlinear static analysis of the curved member model.

5.1.3. Load Combination 1.2G + W

As shown in Table 7, the maximum fibre stress was 88 MPa, which came from non-linear static analysis of the curved model and was less than the 350 MPa yield limit. The difference in maximum fibre stress experienced by the 2 models was as much as 15 percent, which supports the idea that the outcome is highly dependent on the accuracy with which the Phoenix structure is modelled. The maximum displacements in Table 8 are relatively small compared to the span, suggesting that the linear and nonlinear static analysis results are valid with the assumptions made. From Figure 81, there is no significant difference between the clockwise and anticlockwise wrapping of steel members in terms of fibre stress.

Table 7. Fibre stresses under 1.2G + W load combination.

Solver	Maximum Fibre Stress (MPa)		Difference (%)
	Straight Members	Curved Members	
Linear Static	73.97	87.41	15.4
Nonlinear Static	74.10	87.73	15.5
Nonlinear Static Load Factor	4.69	3.94	16.0

Table 8. Displacements under 1.2G + W load combination.

Solver	Straight Member Model Maximum Displacements (mm)			
	D_X	D_Y	D_Z	D_{XYZ}
Linear Static	9.54	12.90	-31.91	32.37
Nonlinear Static	9.57	12.91	-31.99	32.45
Solver	Curved Member Model Maximum Displacements (mm)			
	D_X	D_Y	D_Z	D_{XYZ}
Linear Static	14.91	19.14	-48.09	48.74
Nonlinear Static	14.81	19.18	-46.61	47.44

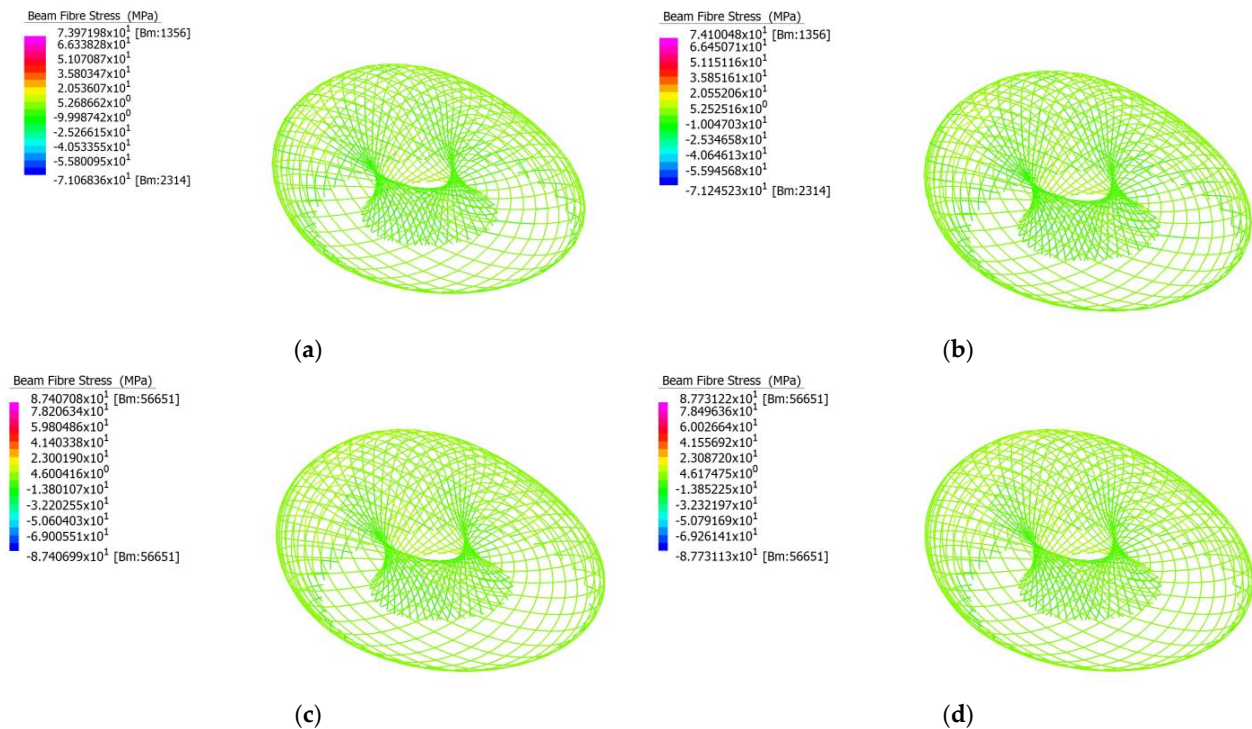


Figure 81. (a) Linear analysis of total fibre stress of straight member model under load combination 1.2G + W; (b) Nonlinear analysis of total fibre stress of straight member model under load combination 1.2G + W; (c) Linear analysis of total fibre stress of curved member model under load combination 1.2G + W; (d) Nonlinear analysis of total fibre stress of curved member model under load combination 1.2G + W.

Figure 82 depicts the difference in linear buckling behaviour of the straight and curved models. As with the load combination 1.2G + 1.5Q, the straight model experiences local buckling near the base of the structure, but at a slightly higher elevation.

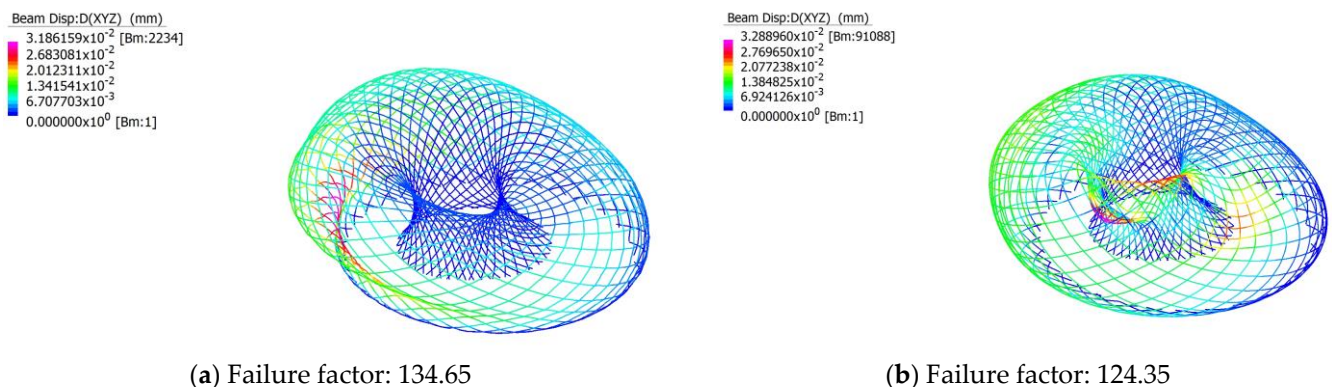


Figure 82. (a) Linear buckling analysis of the straight member model under load combination 1.2G + W with D_{XYZ} displacement contour; (b) Linear buckling analysis of the curved member model under load combination 1.2G + W with D_{XYZ} displacement contour.

For the curved model, however, buckling occurs at the top of the structure, where there should be the least amount of axial force. For both models, the linear buckling failure factor is well above the load factors outlined in Table 7. The maximum load factor for the load combination 1.2G + W is therefore 3.94, from nonlinear static analysis of the curved member model.

The designed steel–glass façade of the Phoenix International Medica Center structure performed well under the load combinations proposed in AS1170.1 [61]. All members were

within the elastic yield range, meaning that deformations were small and non-permanent. According to the results, the critical load combination was 1.2G + 1.5Q, which resulted in a load factor of 3.07 for the curved member model. The curvature of members plays a significant role in the performance outcome, as at best, this change in geometry makes for a minimum 15% difference in experienced fibre stress, and at worst, a 20% difference in experienced load.

5.2. Kazakhstan Pavilion

The Kazakhstan Pavilion and Science Museum was modelled in Strand7 with full restraint at its base, with C350LO 457.0x12.7 CHS beam members being used. The curved modelled has 20 times more nodes along beam paths than the straight model, effectively making curved beam members.

The Kazakhstan Pavilion models for both straight and curved members perform well under the strength limit states outlined in AS1170.0 [64], with the fibre stress of members never exceeding the yield limit of 350 MPa. The maximum fibre stress was 297 MPa, experienced by the curved member model under the load combination 1.2G + 1.5Q using nonlinear static analysis. The ultimate load factor was 1.18, experienced by the curved member model under nonlinear static analysis and the load combination 1.2G + 1.5Q. The results are highly dependent on the accuracy of the model, with the straight and curved member model performance deviating as much as nearly 50% under the load condition 1.2G + W.

5.2.1. Load Combination 1.2G + 1.5Q

Table 9 summarises the total fibres stress in beams for both the straight and curved models for both linear and nonlinear analysis, under the load combination 1.2G + 1.5Q, while Table 10 summarises their displacements.

Table 9. Fibre stresses under 1.2G + 1.5Q load combination.

Solver	Maximum Fibre Stress (MPa)		Difference (%)
	Straight Members	Curved Members	
Linear Static	−193.13	294.59	34.4
Nonlinear Static	−193.52	297.17	34.9
Nonlinear Static Load Factor	1.81	1.18	34.8

Table 10. Displacements under 1.2G + 1.5Q load combination.

Solver	Straight Member Model Maximum Displacements (mm)			
	D _X	D _Y	D _Z	D _{XYZ}
Linear Static	26.84	39.88	−146.51	146.51
Nonlinear Static	27.17	39.85	−147.57	147.57
Solver	Curved Member Model Maximum Displacements (mm)			
	D _X	D _Y	D _Z	D _{XYZ}
Linear Static	42.66	57.37	−212.60	212.60
Nonlinear Static	43.10	57.41	−215.52	215.52

As shown in Table 9, the maximum fibre stress was 297 MPa, which came from nonlinear static analysis of the curved model and was less than the 350 MPa yield limit. The difference in maximum fibre stress experienced by the 2 models was as much as 35 percent, suggesting that the outcome is highly dependent on the accuracy with which the structure is modelled. The maximum displacements in Table 10 are relatively small compared to the span, suggesting that the linear and nonlinear static analysis results are valid with the assumptions made.

Figure 83 depicts the fibre stresses experienced by the members for the straight and curved models. It is important to note that the members shown are represented by a line, and thus, the fibre stress of each member cannot be fully shown. The lateral supports experience significantly more fibre stress than the rest of the members. This could be due to lateral loads on the local axis of these members, creating moments that induce large individual fibre stresses, which skew the average shown. This phenomenon seemingly only occurs in the straight member model, as the curved model exhibits little of this behaviour, except for one lateral support near the bottom of the model.

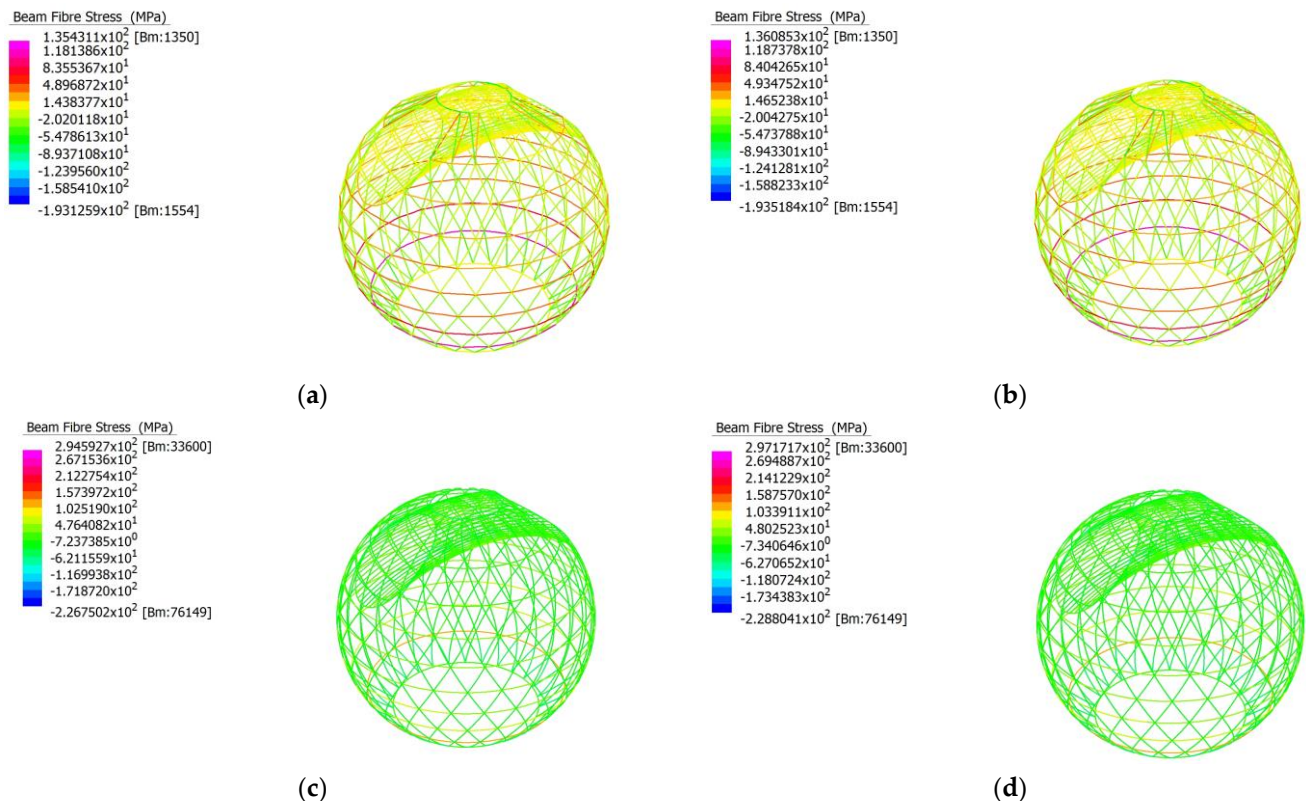
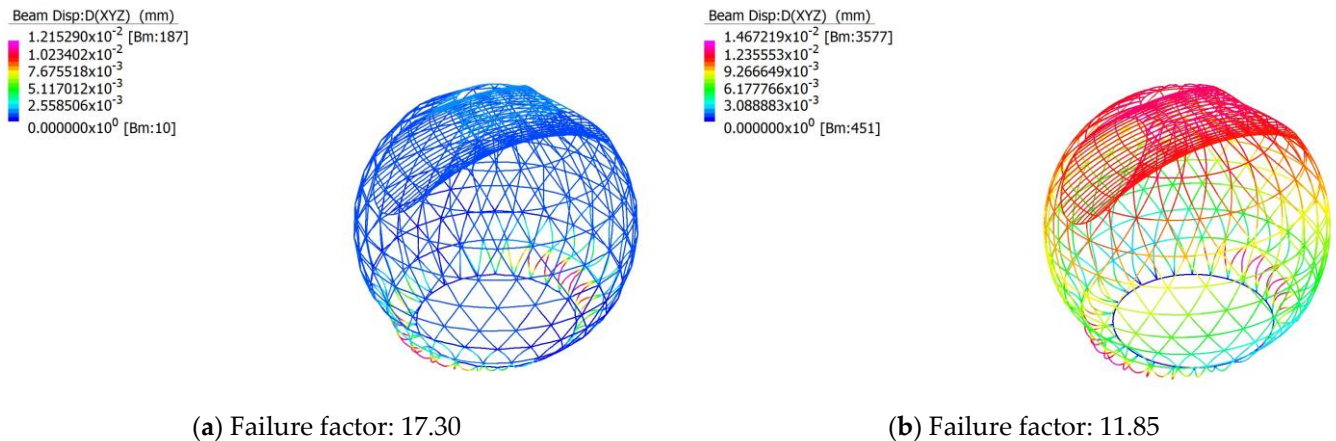


Figure 83. (a) Linear analysis of straight member model under load combination 1.2G + 1.5Q; (b) Nonlinear analysis of straight member model under load combination 1.2G + 1.5Q; (c) Linear analysis of curved member model under load combination 1.2G + 1.5Q; (d) Nonlinear analysis of curved member model under load combination 1.2G + 1.5Q.

Figure 84 depicts the difference in linear buckling behaviour of the straight and curved models. For the straight model, the first mode of buckling failure occurs at the bottom supporting members located beneath where the tube section connects to the rest of the structure. This is most likely due to these members experiencing a higher axial and lateral load, as these members support the exterior frames of the sphere and the interior members of the tube. The curved model behaves similar to the straight model, except that there is a colour gradient up the model. This is most likely an artifact of the high subdividing performed to approximate a curved member. For both models, the linear buckling failure factor is well above the load factors outlined in Table 9. The maximum load factor for the load combination 1.2G + 1.5Q is therefore 1.18, from nonlinear static analysis of the curved member model.



(a) Failure factor: 17.30

(b) Failure factor: 11.85

Figure 84. (a) Linear buckling analysis of the straight member model under load combination 1.2G + 1.5Q with D_{XYZ} displacement contour; (b) Linear buckling analysis of the curved member model under load combination 1.2G + 1.5Q with D_{XYZ} displacement contour.

5.2.2. Load Combination 1.35G

Table 11 summarises the total fibres stress in beams for both the straight and curved models for both linear and nonlinear analysis, under load combination 1.35G, while Table 12 summarises their displacements.

Table 11. Fibre stresses under 1.35G load combination.

Solver	Maximum Fibre Stress (MPa)		Difference (%)
	Straight Members	Curved Members	
Linear Static	−171.75	216.77	20.8
Nonlinear Static	−172.02	218.09	21.1
Nonlinear Static Load Factor	2.03	1.60	21.2

Table 12. Displacements under 1.35G load combination.

Solver	Straight Member Model Maximum Displacements (mm)			
	D_X	D_Y	D_Z	D_{XYZ}
Linear Static	24.77	36.38	−128.65	128.65
Nonlinear Static	25.04	36.35	−129.44	129.44
Solver	Curved Member Model Maximum Displacements (mm)			
	D_X	D_Y	D_Z	D_{XYZ}
Linear Static	39.37	53.10	−186.99	186.99
Nonlinear Static	39.69	53.11	−188.88	188.88

As shown in Table 11, the maximum fibre stress was 218 MPa, which came from nonlinear static analysis of the curved model and was less than the 350 MPa yield limit. The difference in maximum fibre stress experienced by the 2 models was as much as 21 percent, which supports the idea that the outcome is highly dependent on the accuracy with which the structure is modelled. The maximum displacements in Table 12 are relatively small compared to the span, suggesting that the linear and nonlinear static analysis results are valid with the assumptions made. From Figure 85, the structure exhibits similar behaviour when under the load combination 1.2G + 1.5Q.

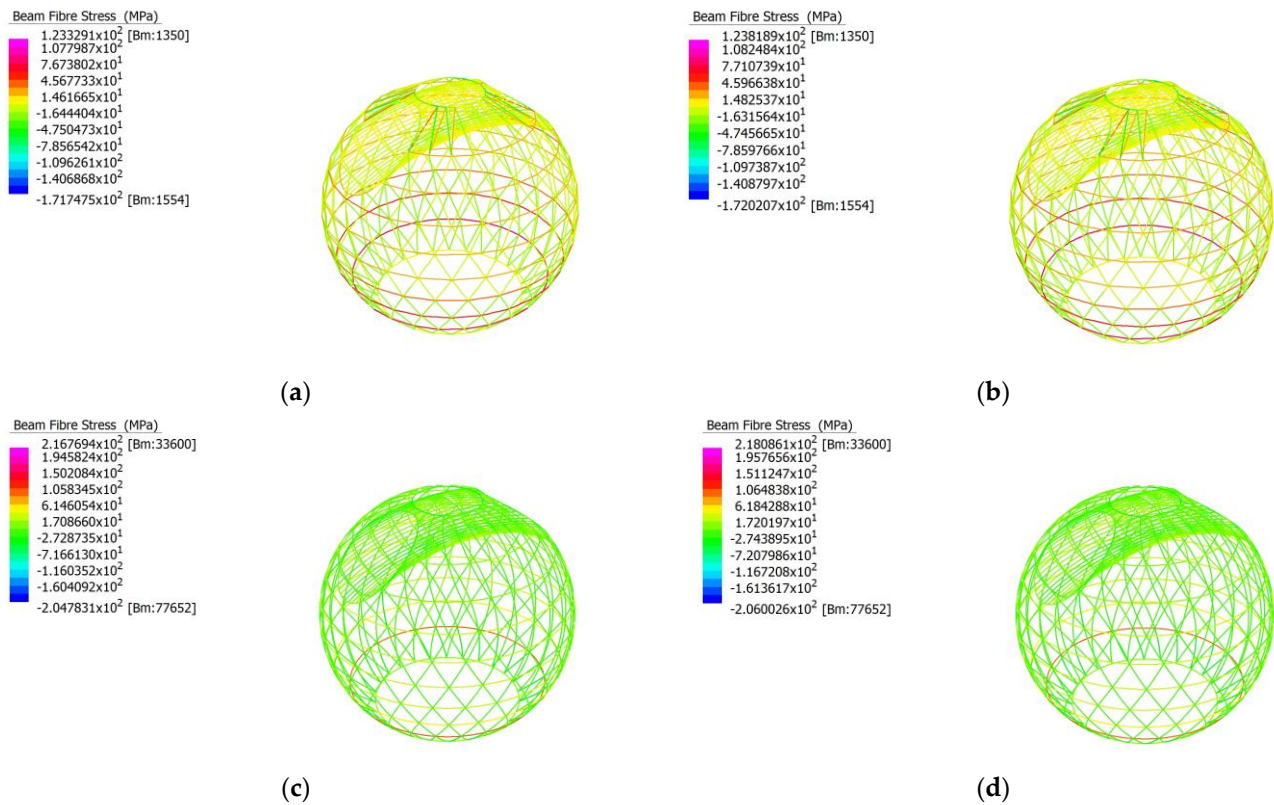


Figure 85. (a) Linear analysis of straight member model under load combination 1.35G; (b) Nonlinear analysis of straight member model under load combination 1.35G; (c) Linear analysis of curved member model under load combination 1.35G; (d) Nonlinear analysis of curved member model under load combination 1.35G.

Figure 86 depicts a similar buckling failure behaviour when under the load combination 1.2G + 1.5Q. For both models, the linear buckling failure factor is well above the load factors outlined in Table 11. The maximum load factor for load combination 1.35G is therefore 1.60, from nonlinear static analysis of the curved member model.

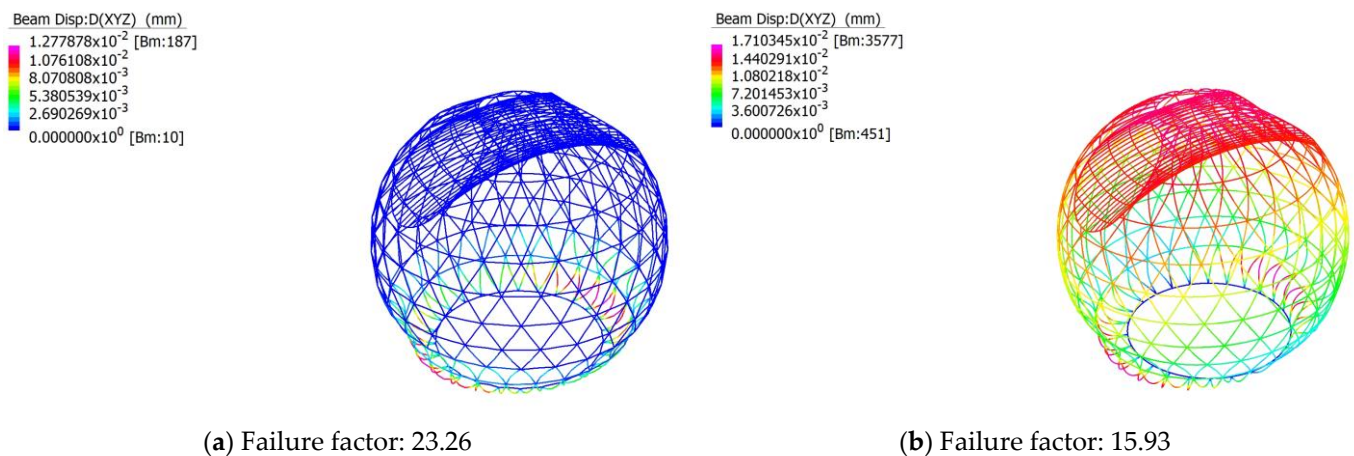


Figure 86. (a) Linear buckling analysis of the straight member model under load combination 1.35G with D_{xyz} displacement contour; (b) Linear buckling analysis of the curved member model under load combination 1.35G with D_{xyz} displacement contour.

5.2.3. Load Combination 1.2G + W

Table 13 summarises the total fibres stress in beams for both the straight and curved models for both linear and nonlinear analysis, under the load combination 1.2G + W, while Table 14 summarises their displacements.

Table 13. Fibre stresses under 1.2G + W load combination.

Solver	Maximum Fibre Stress (MPa)		Difference (%)
	Straight Members	Curved Members	
Linear Static	−132.23	253.26	47.8
Nonlinear Static	−132.58	257.52	48.5
Nonlinear Static Load Factor	2.63	1.33	49.4

Table 14. Displacements under 1.2G + W load combination.

Solver	Straight Member Model Maximum Displacements (mm)			
	D _X	D _Y	D _Z	D _{XYZ}
Linear Static	17.05	60.81	−101.74	109.60
Nonlinear Static	17.21	62.13	−102.32	110.28
Solver	Curved Member Model Maximum Displacements (mm)			
	D _X	D _Y	D _Z	D _{XYZ}
Linear Static	29.96	97.39	−141.08	158.70
Nonlinear Static	31.87	101.95	−142.91	162.78

As shown in Table 13, the maximum fibre stress was 258 MPa, which came from non-linear static analysis of the curved model and was less than the 350 MPa yield limit. The difference in maximum fibre stress experienced by the 2 models was as much as 49 percent, which supports the idea that the outcome is highly dependent on the accuracy with which the structure is modelled. The maximum displacements in Table 14 are relatively small compared to the span, suggesting that the linear and nonlinear static analysis results are valid with the assumptions made.

From Figure 87, the structure exhibits similar behaviour when under the load combination 1.2G + 1.5Q. Upon closer inspection, it is noticeable that for the linear and nonlinear results for the curved member model, one side of the bottom lateral support experiences more fibre stress than the norm. This is most likely due to the increase in axial loading due to wind actions.

Figure 88 depicts a similar buckling failure behaviour when under the load combination 1.2G + 1.5Q; however, only one side experiences buckling. This is most likely due to one side experiencing more axial loading due to wind actions. For both models, the linear buckling failure factor is well above the load factors outlined in Table 13. The maximum load factor for the load combination 1.2G + W is therefore 1.33, from nonlinear static analysis of the curved member model.

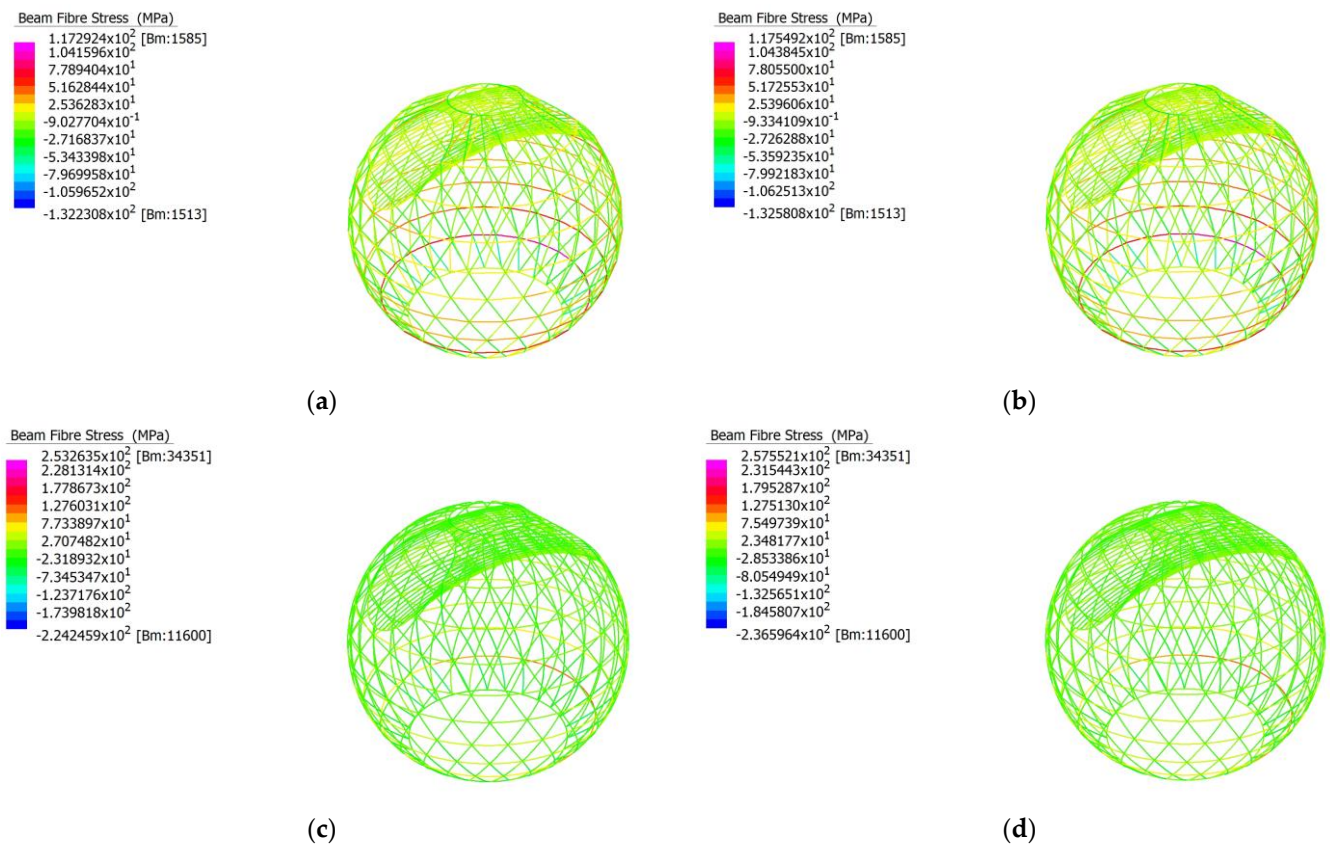


Figure 87. (a) Linear analysis of straight member model under load combination 1.35G; (b) Nonlinear analysis of straight member model under load combination 1.35G; (c) Linear analysis of curved member model under load combination 1.35G; (d) Nonlinear analysis of curved member model under load combination 1.35G.

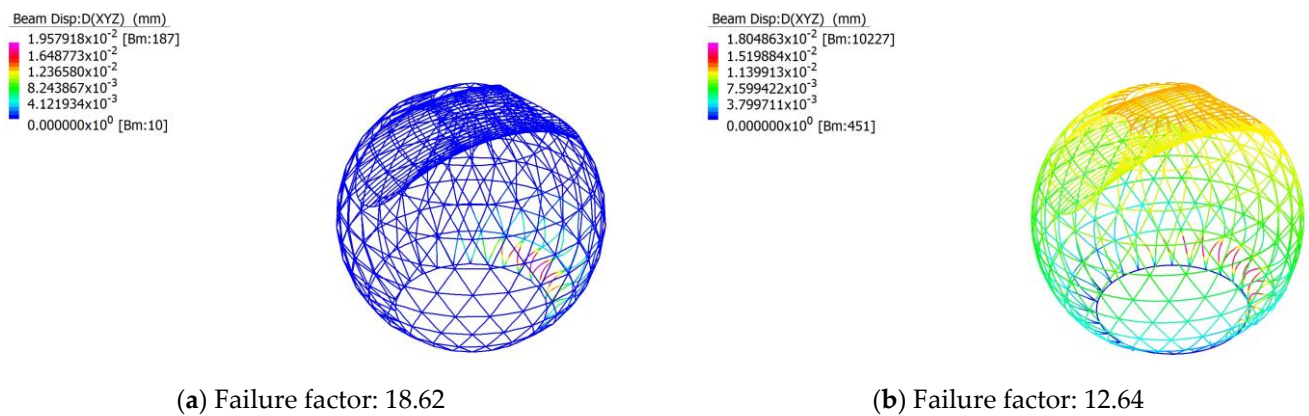


Figure 88. (a) Linear buckling analysis of the straight member model under load combination 1.35G with D_{XYZ} displacement contour; (b) Linear buckling analysis of the curved member model under load combination 1.35G with D_{XYZ} displacement contour.

5.3. Moynihan Train Hall

Moynihan Train Hall in New York City was modelled in Strand7 with full restraint at its base, with C350LO 100 × 50 × 4.0 RHS beam members being used. The curved modelled has 20 times more nodes along beam paths than the straight model, effectively making curved beam members.

Moynihan Train Hall models for both straight and curved members perform well under the strength limit states outlined in AS1170.0 [64], with the fibre stress of members

never exceeding the yield limit of 350 MPa. The maximum fibre stress was 70 MPa, experienced by the curved member model under the load combination 1.2G + 1W using linear static analysis. The ultimate load factor was 5.54, experienced by the curved member model under nonlinear static analysis for the load combination 1.2G + 1.5Q. The results are highly dependent on the accuracy of the model, with the straight and curved member model performance deviating as much as nearly 11% under the load condition 1.2G + W.

5.3.1. Load Combination 1.2G + 1.5Q

Table 15 summarises the total fibres stress in beams for both the straight and curved models for both linear and nonlinear analysis, under the load combination 1.2G + 1.5Q, while Table 16 summarises their displacements.

Table 15. Fibre stresses under 1.2G + 1.5Q load combination.

Solver	Maximum Fibre Stress (MPa)		Difference (%)
	Straight Members	Curved Members	
Linear Static	−43.12	−48.33	10.8
Nonlinear Static	−44.92	−50.18	10.5
Nonlinear Static Load Factor	5.93	5.54	6.68

Table 16. Displacement under 1.2G + 1.5Q load combination.

Solver	Straight Member Model Maximum Displacements (mm)			
	D _X	D _Y	D _Z	D _{XYZ}
Linear Static	1.68	2.28	−4.69	5.21
Nonlinear Static	1.74	2.42	−4.99	5.54
Solver	Curved Member Model Maximum Displacements (mm)			
	D _X	D _Y	D _Z	D _{XYZ}
Linear Static	1.72	2.32	−4.78	5.32
Nonlinear Static	1.78	2.48	−5.10	5.68

As shown in Table 15, the maximum fibre stress was 50 MPa, which came from non-linear static analysis of the curved model and was less than the 350 MPa yield limit. The difference in maximum fibre stress experienced by the 2 models was as much as 10 percent, suggesting that the outcome is dependent on the accuracy with which the structure is modelled. The maximum displacements in Table 16 are relatively small compared to the span, suggesting that the linear and nonlinear static analysis results are valid with the assumptions made.

Figure 89 depicts the fibre stresses experienced by the members for the straight and curved models. It is important to note that the members shown are represented by a line, and thus, the fibre stress of each member cannot be fully shown. There is no significant difference between the straight and curved, and linear and nonlinear static analysis results.

Figure 90 depicts the difference in linear buckling behaviour of the straight and curved models. For both the straight and curved models, the first buckling mode occurs in the same location. For both models, the linear buckling failure factor is well above the load factors outlined in Table 15. The maximum load factor for the load combination 1.2G + 1.5Q is therefore 5.54, from nonlinear static analysis of the curved member model.

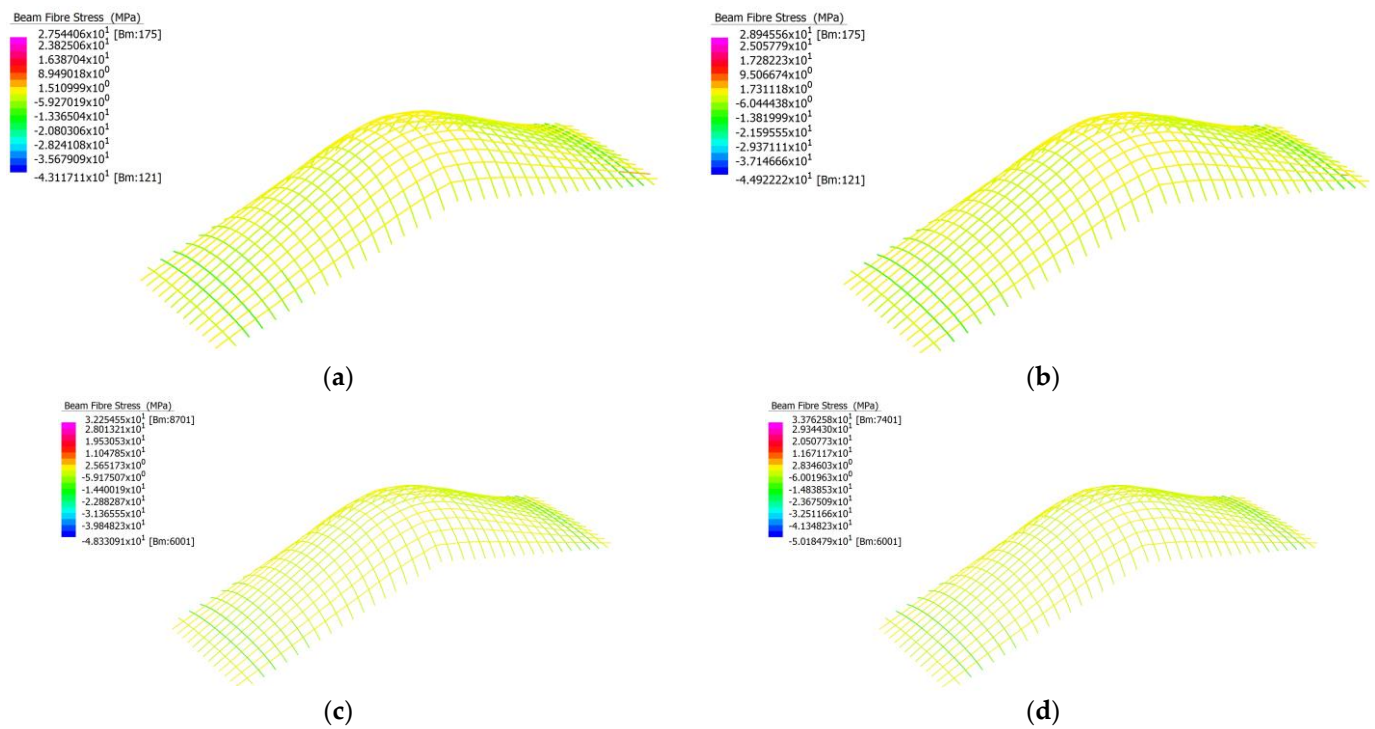


Figure 89. (a) Linear analysis of straight member model under load combination 1.2G + 1.5Q; (b) Nonlinear analysis of straight member model under load combination 1.2G + 1.5Q; (c) Linear analysis of curved member model under load combination 1.2G + 1.5Q; (d) Nonlinear analysis of curved member model under load combination 1.2G + 1.5Q.

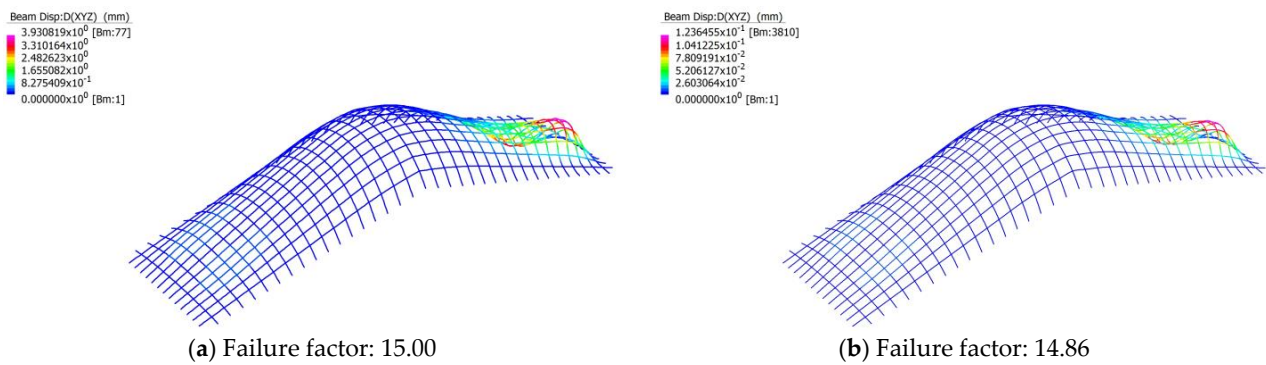


Figure 90. (a) Linear buckling analysis of the straight member model under load combination 1.2G + 1.5Q with D_{XYZ} displacement contour; (b) Linear buckling analysis of the curved member model under load combination 1.2G + 1.5Q with D_{XYZ} displacement contour.

5.3.2. Load Combination 1.35G

Table 17 summarises the total fibres stress in beams for both the straight and curved models for both linear and nonlinear analysis, under the load combination 1.35G, while Table 18 summarises their displacements.

Table 17. Fibre stresses under 1.35G load combination.

Solver	Maximum Fibre Stress (MPa)		Difference (%)
	Straight Members	Curved Members	
Linear Static	−19.38	−21.72	10.8
Nonlinear Static	−19.73	−22.08	10.6
Nonlinear Static Load Factor	13.20	12.32	6.67

Table 18. Displacement under 1.35G load combination.

Solver	Straight Member Model Maximum Displacements (mm)			
	D_X	D_Y	D_Z	D_{XYZ}
Linear Static	0.76	1.02	−2.11	2.34
Nonlinear Static	0.77	1.05	−2.16	2.41
Solver	Curved Member Model Maximum Displacements (mm)			
	D_X	D_Y	D_Z	D_{XYZ}
Linear Static	0.77	1.04	−2.15	2.39
Nonlinear Static	0.79	1.07	−0.21	2.46

As shown in Table 17, the maximum fibre stress was 22 MPa, which came from non-linear static analysis of the curved model and was less than the 350 MPa yield limit. The difference in maximum fibre stress experienced by the 2 models was as much as 10 percent, which supports the idea that the outcome is dependent on the accuracy with which the structure is modelled. The maximum displacements in Table 18 are relatively small compared to the span, suggesting that the linear and nonlinear static analysis results are valid with the assumptions made. From Figure 91, the structure exhibits similar behaviour when under the load combination 1.2G + 1.5Q.

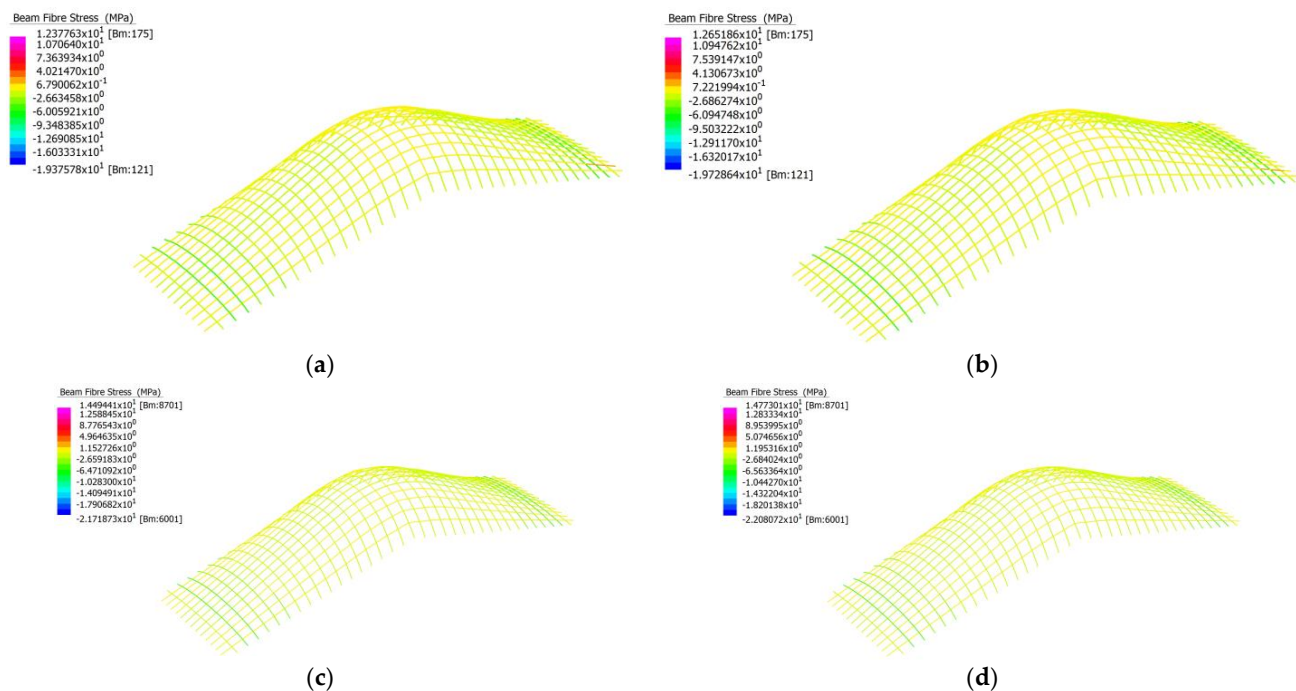


Figure 91. (a) Linear analysis of straight member model under load combination 1.35G; (b) Nonlinear analysis of straight member model under load combination 1.35G; (c) Linear analysis of curved member model under load combination 1.35G; (d) Nonlinear analysis of curved member model under load combination 1.35G.

Figure 92 depicts a similar buckling failure behaviour when under the load combination 1.2G + 1.5Q. For both models, the linear buckling failure factor is well above the load factors outlined in Table 17. The maximum load factor for the load combination 1.35G is therefore 12.32, from nonlinear static analysis of the curved member model.

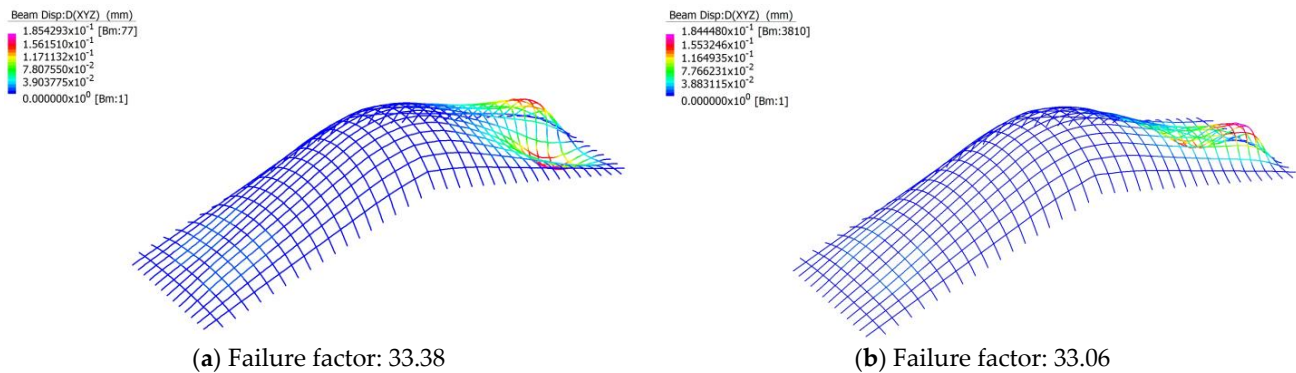


Figure 92. (a) Linear buckling analysis of the straight member model under load combination 1.35G with D_{XYZ} displacement contour; (b) Linear buckling analysis of the curved member model under load combination 1.35G with D_{XYZ} displacement contour.

5.3.3. Load Combination 1.2G + W

Table 19 summarises the total fibres stress in beams for both the straight and curved models for both linear and nonlinear analysis, under the load combination 1.2G + W, while Table 20 summarises their displacements.

Table 19. Fibre stresses under 1.2G + W load combination.

Solver	Maximum Fibre Stress (MPa)		Difference (%)
	Straight Members	Curved Members	
Linear Static	62.77	70.40	10.8
Nonlinear Static	59.53	67.07	11.2
Nonlinear Static Load Factor	7.36	6.43	12.6

Table 20. Displacement under 1.2G + W load combination.

Solver	Straight Member Model Maximum Displacements (mm)			
	D_X	D_Y	D_Z	D_{XYZ}
Linear Static	2.14	3.56	7.03	7.88
Nonlinear Static	2.04	3.40	6.58	7.38
Solver	Curved Member Model Maximum Displacements (mm)			
	D_X	D_Y	D_Z	D_{XYZ}
Linear Static	2.20	3.62	7.17	8.04
Nonlinear Static	2.08	3.38	6.67	7.48

As shown in Table 19, the maximum fibre stress was 70 MPa, which came from linear static analysis of the curved model and was less than the 350 MPa yield limit. The difference in maximum fibre stress experienced by the 2 models was as much as 12 percent, which supports the idea that the outcome is dependent on the accuracy with which the structure is modelled. The maximum displacements in Table 20 are relatively small compared to the span, suggesting that the linear and nonlinear static analysis results are valid with the assumptions made. From Figure 93, the structure exhibits similar behaviour when under the load combination 1.2G + 1.5Q.

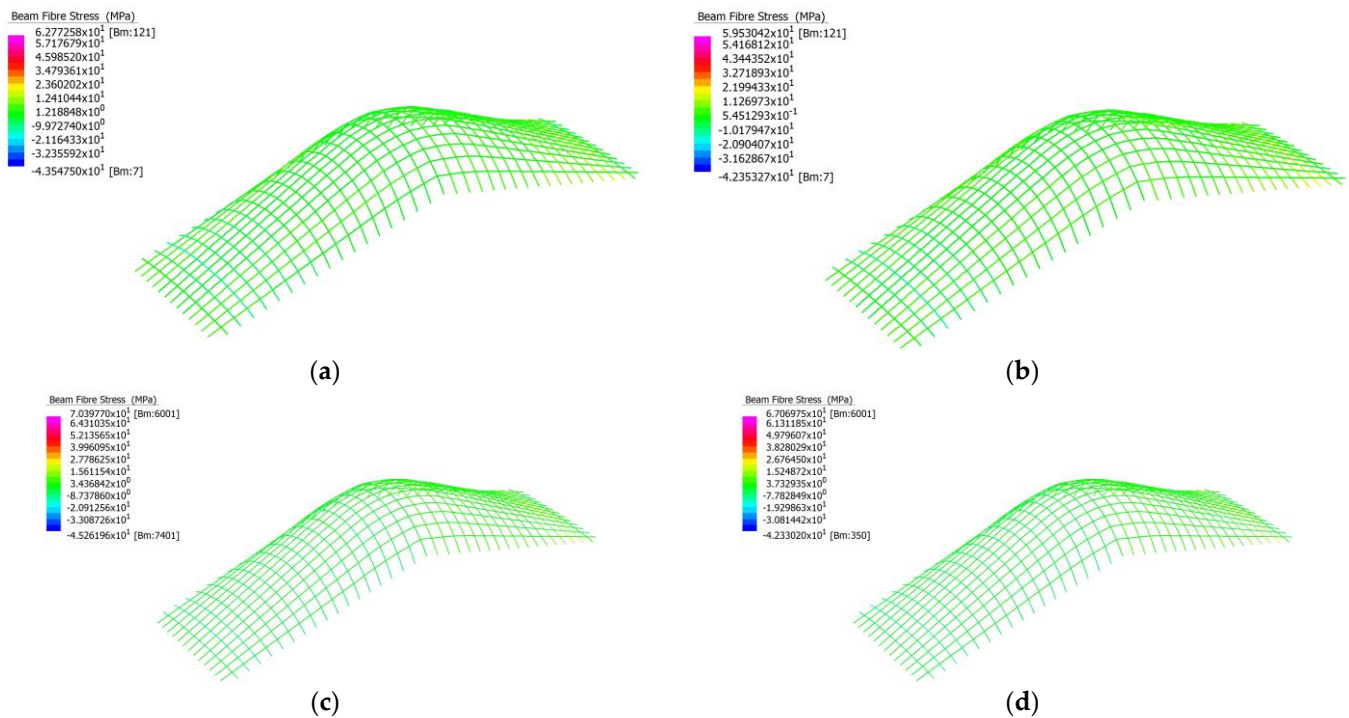
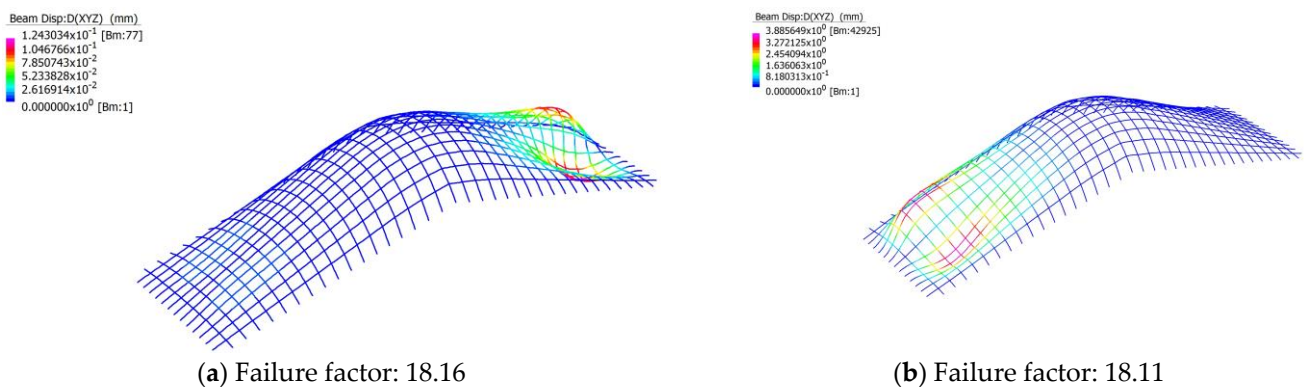


Figure 93. (a) Linear analysis of straight member model under load combination 1.2G + W; (b) Nonlinear analysis of straight member model under load combination 1.2G + W; (c) Linear analysis of curved member model under load combination 1.2G + W; (d) Nonlinear analysis of curved member model under load combination 1.2G + W.

Figure 94 depicts a similar buckling failure behaviour when under the load combination 1.2G + 1.5Q. For both models, the linear buckling failure factor is well above the load factors outlined in Table 19. The maximum load factor for the load combination 1.2G + W is therefore 6.43, from nonlinear static analysis of the curved member model.



(a) Failure factor: 18.16

(b) Failure factor: 18.11

Figure 94. (a) Linear buckling analysis of the straight member model under load combination 1.2G + W with D_{XYZ} displacement contour; (b) Linear buckling analysis of the curved member model under load combination 1.2G + W with D_{XYZ} displacement contour.

5.4. Chadstone Shopping Centre

The Chadstone Shopping Centre was modelled in Strand7 with full restraint at its base, with C350LO 150 × 100 × 5.0 RHS beam members being used. The curved modelled has 20 times more nodes along beam paths than the straight model, effectively making curved beam members.

The Chadstone Shopping Centre models for both the straight and curved members perform well under the strength limit states outlined in AS1170.0 [64], with the fibre stress of members never exceeding the yield limit of 350 MPa. The maximum fibre stress was 190 MPa, experienced by the straight member model under the load combination 1.2G + 1W using nonlinear static analysis. The ultimate load factor was 1.81, experienced by the straight member model under nonlinear static analysis for the load combination 1.2G + 1.5Q. The results are highly dependent on the accuracy of the model, with the straight and curved member model performance deviating as much as nearly 26% under the load condition 1.2G + W.

5.4.1. Load Combination 1.2G + 1.5Q

Table 21 summarises the total fibres stress in beams for both the straight and curved models for both linear and nonlinear analysis, under the load combination 1.2G + 1.5Q, while Table 22 summarises their displacements.

Table 21. Fibre stresses under 1.2G + 1.5Q load combination.

Solver	Maximum Fibre Stress (MPa)		Difference (%)
	Straight Members	Curved Members	
Linear Static	185.72	−137.35	26.0
Nonlinear Static	189.99	−142.99	24.7
Nonlinear Static Load Factor	1.81	2.27	20.3

Table 22. Displacement under 1.2G + 1.5Q load combination.

Solver	Straight Member Model Maximum Displacements (mm)			
	D _X	D _Y	D _Z	D _{XYZ}
Linear Static	27.79	24.56	−22.86	43.57
Nonlinear Static	27.93	24.71	−23.17	43.90
Solver	Curved Member Model Maximum Displacements (mm)			
	D _X	D _Y	D _Z	D _{XYZ}
Linear Static	24.65	21.74	−45.19	45.55
Nonlinear Static	26.46	25.22	−50.10	50.54

As shown in Table 21, the maximum fibre stress was 190 MPa, which came from non-linear static analysis of the straight model and was less than the 350 MPa yield limit. The difference in maximum fibre stress experienced by the 2 models was as much as 26 percent, suggesting that the outcome is highly dependent on the accuracy with which the structure is modelled. Interestingly, the maximum fibre stress changes from compressive to tensile between the straight and curved member models. The maximum displacements in Table 22 are relatively small compared to the span, suggesting that the linear and nonlinear static analysis results are valid with the assumptions made.

Figure 95a depicts the fibre stresses experienced by the members for the straight and curved models. It is important to note that the members shown are represented by a line, and thus the fibre stress of each member cannot be fully shown. The curved member model shows significant loading of the major span across the midsection of the structure, which abruptly starts and ends. The reason for this is not entirely clear. It could be an artifact of the high subdivision performed to approximate the curved members.

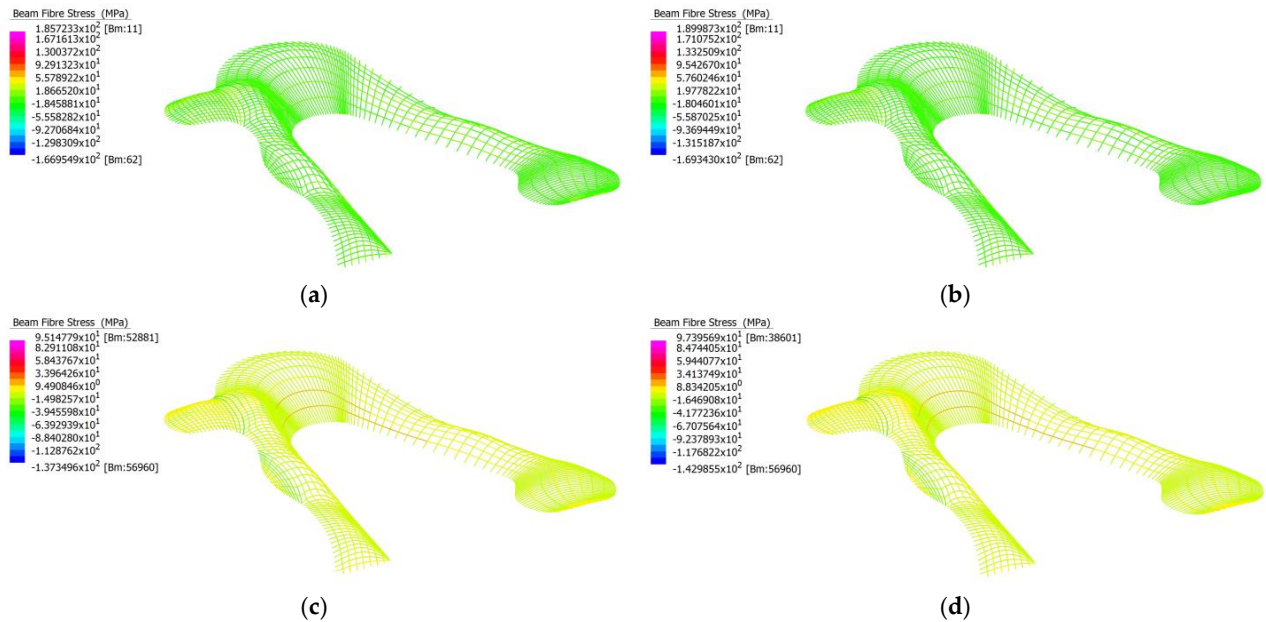


Figure 95. (a) Linear analysis of straight member model under load combination 1.2G + 1.5Q; (b) Nonlinear analysis of straight member model under load combination 1.2G + 1.5Q; (c) Linear analysis of curved member model under load combination 1.2G + 1.5Q; (d) Nonlinear analysis of curved member model under load combination 1.2G + 1.5Q.

Figure 96 depicts the difference in linear buckling behaviour of the straight and curved models. There is a significant difference between the two models, as they depict first the buckling failure at separate locations and with very different failure load factors. For both models, the linear buckling failure factor is well above the load factors outlined in Table 21. The maximum load factor for the load combination 1.2G + 1.5Q is therefore 1.81, from nonlinear static analysis of the straight member model.

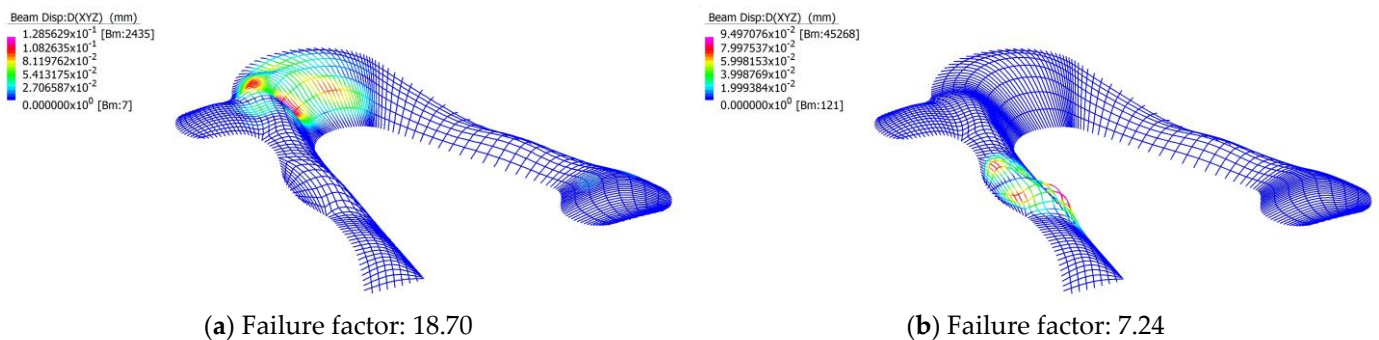


Figure 96. (a) Linear buckling analysis of the straight member model under load combination 1.2G + 1.5Q with D_{XYZ} displacement contour; (b) Linear buckling analysis of the curved member model under load combination 1.2G + 1.5Q with D_{XYZ} displacement contour.

5.4.2. Load Combination 1.35G

Table 23 summarises the total fibres stress in beams for both the straight and curved models for both linear and nonlinear analysis, under the load combination 1.35G, while Table 24 summarises their displacements.

Table 23. Fibre stresses under 1.35G load combination.

Solver	Maximum Fibre Stress (MPa)		Difference (%)
	Straight Members	Curved Members	
Linear Static	−51.82	−56.04	7.5
Nonlinear Static	−53.14	−56.94	6.7
Nonlinear Static Load Factor	5.74	5.56	3.1

Table 24. Displacement under 1.35G load combination.

Solver	Straight Member Model Maximum Displacements (mm)			
	D _X	D _Y	D _Z	D _{XYZ}
Linear Static	9.11	7.71	−17.55	17.70
Nonlinear Static	9.33	8.16	−18.26	18.41
Solver	Curved Member Model Maximum Displacements (mm)			
	D _X	D _Y	D _Z	D _{XYZ}
Linear Static	10.06	8.87	−18.44	18.58
Nonlinear Static	10.35	9.40	−19.18	19.34

As shown in Table 23, the maximum fibre stress was 57 MPa, which came from non-linear static analysis of the curved model and was less than the 350 MPa yield limit. The difference in maximum fibre stress experienced by the two models was as much as seven percent, which supports the idea that the outcome is dependent on the accuracy with which the structure is modelled. The maximum displacements in Table 24 are relatively small compared to the span, suggesting that the linear and nonlinear static analysis results are valid with the assumptions made.

From Figure 97, the structure exhibits similar behaviour when under the load combination 1.2G + 1.5Q, but now the straight member model exhibits the same behaviour as the curved model. This could be an effect of additional loading of these members, as they support a larger portion of area than the average member.

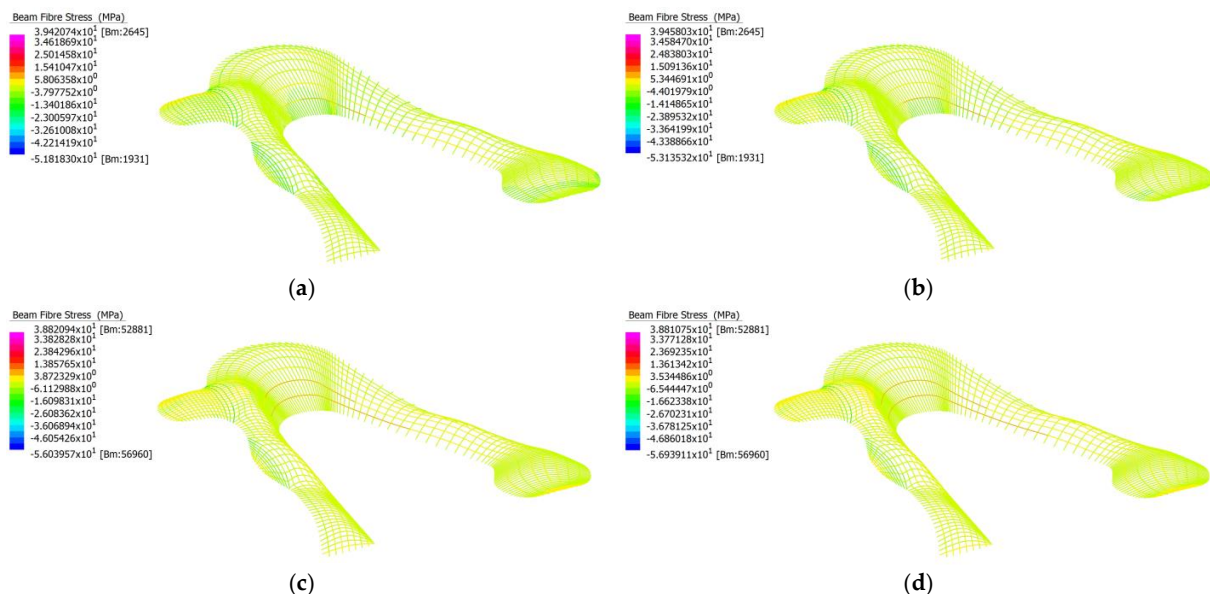


Figure 97. (a) Linear analysis of straight member model under load combination 1.35G; (b) Nonlinear analysis of straight member model under load combination 1.35G; (c) Linear analysis of curved member model under load combination 1.35G; (d) Nonlinear analysis of curved member model under load combination 1.35G.

From Figure 98, the straight and curved member models are shown as having the same mode of buckling failure at the same location. For both models, the linear buckling failure factor is well above the load factors outlined in Table 23. The maximum load factor for the load combination 1.35G is therefore 5.74, from nonlinear static analysis of the straight member model.

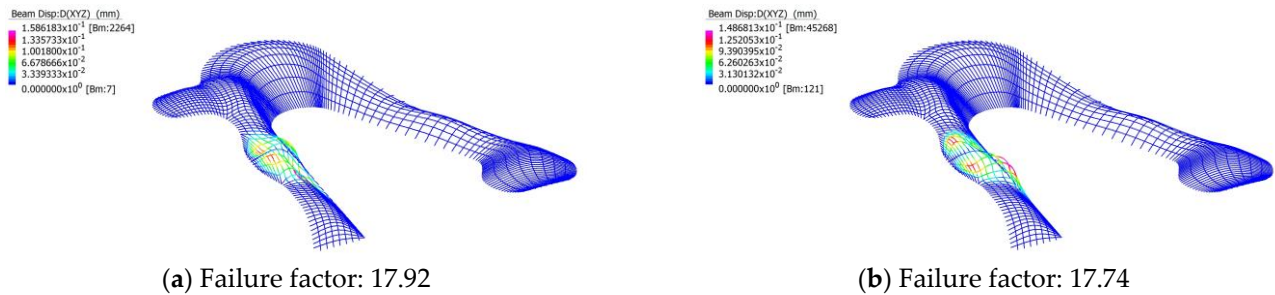


Figure 98. (a) Linear buckling analysis of the straight member model under load combination 1.35G with D_{XYZ} displacement contour; (b) Linear buckling analysis of the curved member model under load combination 1.35G with D_{XYZ} displacement contour.

5.4.3. Load Combination 1.2G + W

Table 25 summarises the total fibres stress in beams for both the straight and curved models for both linear and nonlinear analysis, under the load combination 1.2G + W, while Table 26 summarises their displacements.

Table 25. Fibre stresses under 1.2G + W load combination.

Solver	Maximum Fibre Stress (MPa)		Difference (%)
	Straight Members	Curved Members	
Linear Static	170.20	172.68	1.4
Nonlinear Static	166.83	164.57	1.7
Nonlinear Static Load Factor	2.30	2.25	2.2

Table 26. Displacement under 1.2G + W load combination.

Solver	Straight Member Model Maximum Displacements (mm)			
	D_X	D_Y	D_Z	D_{XYZ}
Linear Static	51.32	50.71	41.61	79.47
Nonlinear Static	49.95	46.21	39.34	72.84
Solver	Curved Member Model Maximum Displacements (mm)			
	D_X	D_Y	D_Z	D_{XYZ}
Linear Static	53.36	52.53	42.84	82.02
Nonlinear Static	51.73	47.48	40.48	75.59

As shown in Table 25, the maximum fibre stress was 172 MPa, which came from linear static analysis of the curved model and was less than the 350 MPa yield limit. The difference in maximum fibre stress experienced by the two models was as little as two percent, which discourages the idea that the outcome is dependent on the accuracy with which the structure is modelled. The maximum displacements in Table 26 are relatively small compared to the span, suggesting that the linear and nonlinear static analysis results are valid with the assumptions made. From Figure 99, the structural behaviours present in previous load conditions disappears.

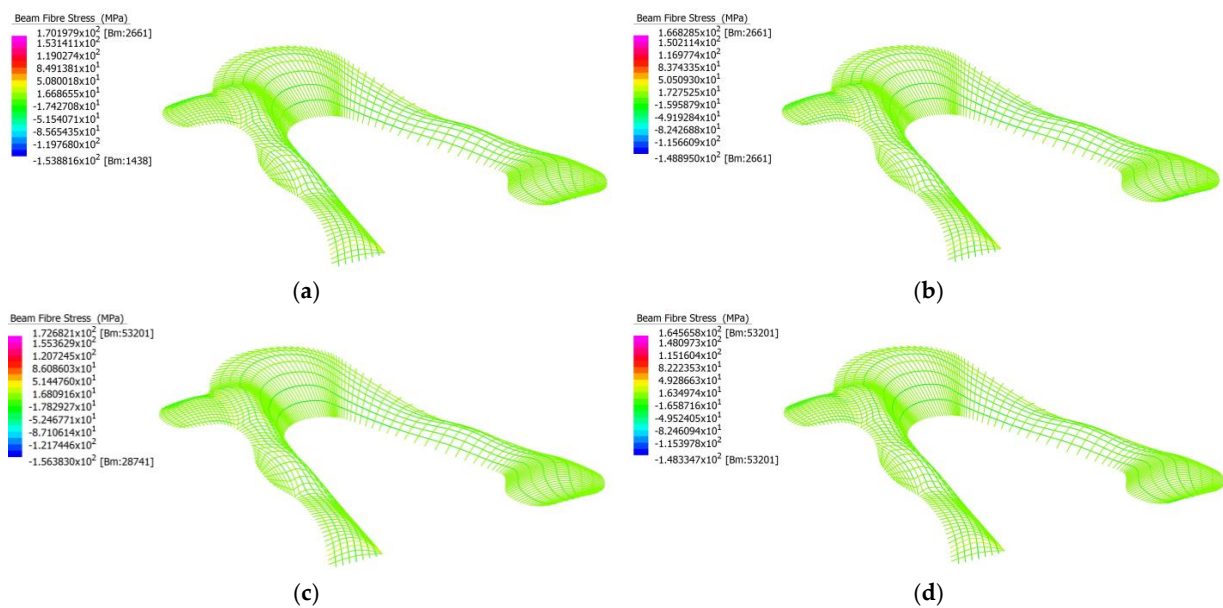


Figure 99. (a) Linear analysis of straight member model under load combination 1.2G + W; (b) Nonlinear analysis of straight member model under load combination 1.2G + W; (c) Linear analysis of curved member model under load combination 1.2G + W; (d) Nonlinear analysis of curved member model under load combination 1.2G + W.

Figure 100 depicts a different buckling failure behaviour when under the load combination 1.2G + 1.5Q. For both models, the linear buckling failure factor is well above the load factors outlined in Table 25. The maximum load factor for the load combination 1.2G + W is therefore 2.25, from nonlinear static analysis of the curved member model.

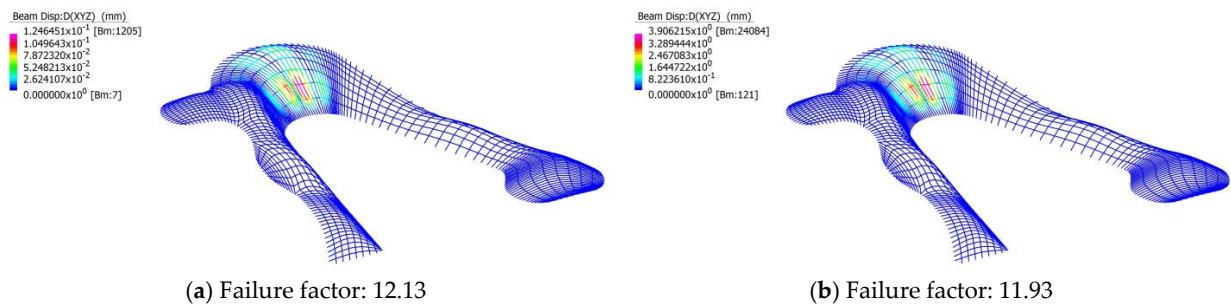


Figure 100. (a) Linear buckling analysis of the straight member model under load combination 1.2G + W with D_{XYZ} displacement contour; (b) Linear buckling analysis of the curved member model under load combination 1.2G + W with D_{XYZ} displacement contour.

5.5. The Hague Central Station Light Rail Station

The Hague Central Station light rail station was modelled in Strand7 with full restraint at its base, with C350LO 125 × 125 × 9.0 SHS beam members being used. The curved modelled has 20 times more nodes along beam paths than the straight model, effectively making curved beam members.

The Chadstone Shopping Centre models for both the straight and curved members perform well under the strength limit states outlined in AS1170.0 [64], with the fibre stress of members never exceeding the yield limit of 350 MPa. The maximum fibre stress was 136 MPa, experienced by the curved member model under the load combination 1.2G + W using nonlinear static analysis. The ultimate load factor was 2.47, experienced by the curved member model under nonlinear static analysis for the load combination 1.2G + W. The results are highly dependent on the accuracy of the model, with the straight and curved member model performance deviating as much as nearly 45% under the load condition 1.2G + W.

5.5.1. Load Combination 1.2G + 1.5Q

Table 27 summarises the total fibres stress in beams for both the straight and curved models for both linear and nonlinear analysis, under the load combination 1.2G + 1.5Q, while Table 28 summarises their displacements.

Table 27. Fibre stresses under 1.2G + 1.5Q load combination.

Solver	Maximum Fibre Stress (MPa)		Difference (%)
	Straight Members	Curved Members	
Linear Static	−84.75	−96.67	12.3
Nonlinear Static	−87.99	−98.54	10.7
Nonlinear Static Load Factor	3.58	3.38	5.59

Table 28. Displacement under 1.2G + 1.5Q load combination.

Solver	Straight Member Model Maximum Displacements (mm)			
	D _X	D _Y	D _Z	D _{XYZ}
Linear Static	5.16	25.07	−54.41	54.41
Nonlinear Static	5.33	26.06	−57.68	57.68
Solver	Curved Member Model Maximum Displacements (mm)			
	D _X	D _Y	D _Z	D _{XYZ}
Linear Static	5.04	29.11	−60.92	60.92
Nonlinear Static	5.26	30.28	−64.76	64.76

As shown in Table 27, the maximum fibre stress was 98 MPa, which came from non-linear static analysis of the curved model and was less than the 350 MPa yield limit. The difference in maximum fibre stress experienced by the 2 models was as much as 12 percent, suggesting that the outcome is dependent on the accuracy with which the structure is modelled. The maximum displacements in Table 28 are relatively small compared to the span, suggesting that the linear and nonlinear static analysis results are valid with the assumptions made.

Figure 101 depicts the fibre stresses experienced by the members for the straight and curved models. It is important to note that the members shown are represented by a line, and thus the fibre stress of each member cannot be fully shown. There appears to be no significant difference between the straight and curved, and linear and nonlinear static analysis results.

Figure 102 depicts the difference in linear buckling behaviour of the straight and curved models. There is a significant difference between the two models, as although they depict a similar buckling behaviour at the same location, the magnitude and area of effect is widely different. For both models, the linear buckling failure factor is well above the load factors outlined in Table 27. The maximum load factor for the load combination 1.2G + 1.5Q is therefore 3.38, from nonlinear static analysis of the straight member model.

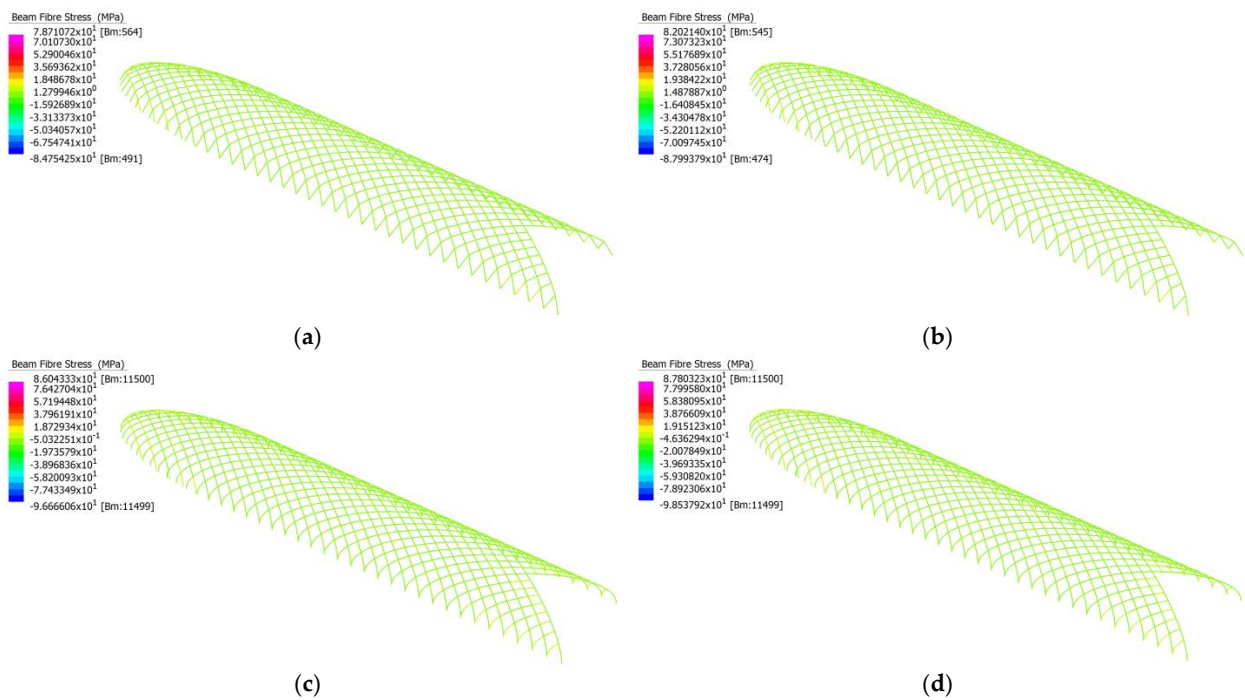


Figure 101. (a) Linear analysis of straight member model under load combination 1.2G + 1.5Q; (b) Nonlinear analysis of straight member model under load combination 1.2G + 1.5Q; (c) Linear analysis of curved member model under load combination 1.2G + 1.5Q; (d) Nonlinear analysis of curved member model under load combination 1.2G + 1.5Q.

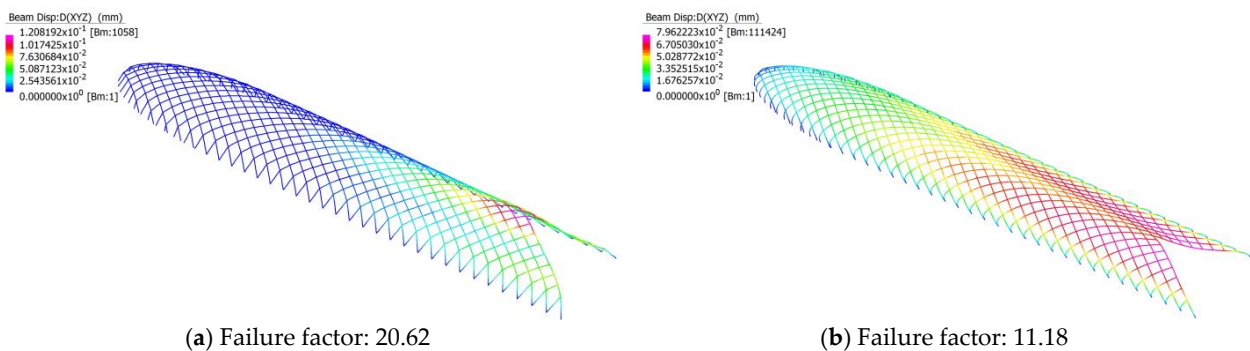


Figure 102. (a) Linear buckling analysis of the straight member model under load combination 1.2G + 1.5Q with D_{XYZ} displacement contour; (b) Linear buckling analysis of the curved member model under load combination 1.2G + 1.5Q with D_{XYZ} displacement contour.

5.5.2. Load Combination 1.35G

Table 29 summarises the total fibres stress in beams for both the straight and curved models for both linear and nonlinear analysis, under the load combination 1.35G, while Table 30 summarises their displacements.

Table 29. Fibre stresses under 1.35G load combination.

Solver	Maximum Fibre Stress (MPa)		Difference (%)
	Straight Members	Curved Members	
Linear Static	−50.42	−57.51	12.3
Nonlinear Static	−51.55	−58.17	11.4
Nonlinear Static Load Factor	6.01	5.69	5.3

Table 30. Displacement under 1.35G load combination.

Solver	Straight Member Model Maximum Displacements (mm)			
	D_X	D_Y	D_Z	D_{XYZ}
Linear Static	3.07	14.92	−32.37	32.37
Nonlinear Static	3.13	15.26	−33.50	33.50
Solver	Curved Member Model Maximum Displacements (mm)			
	D_X	D_Y	D_Z	D_{XYZ}
Linear Static	3.00	17.32	−36.24	36.24
Nonlinear Static	3.07	30.28	−64.76	64.76

As shown in Table 29, the maximum fibre stress was 58 MPa, which came from non-linear static analysis of the curved model and was less than the 350 MPa yield limit. The difference in maximum fibre stress experienced by the 2 models was as much as 12 percent, which supports the idea that the outcome is dependent on the accuracy with which the structure is modelled. The maximum displacements in Table 30 are relatively small compared to the span, suggesting that the linear and nonlinear static analysis results are valid with the assumptions made. From Figure 103, the structure exhibits similar behaviour when under the load combination 1.2G + 1.5Q.

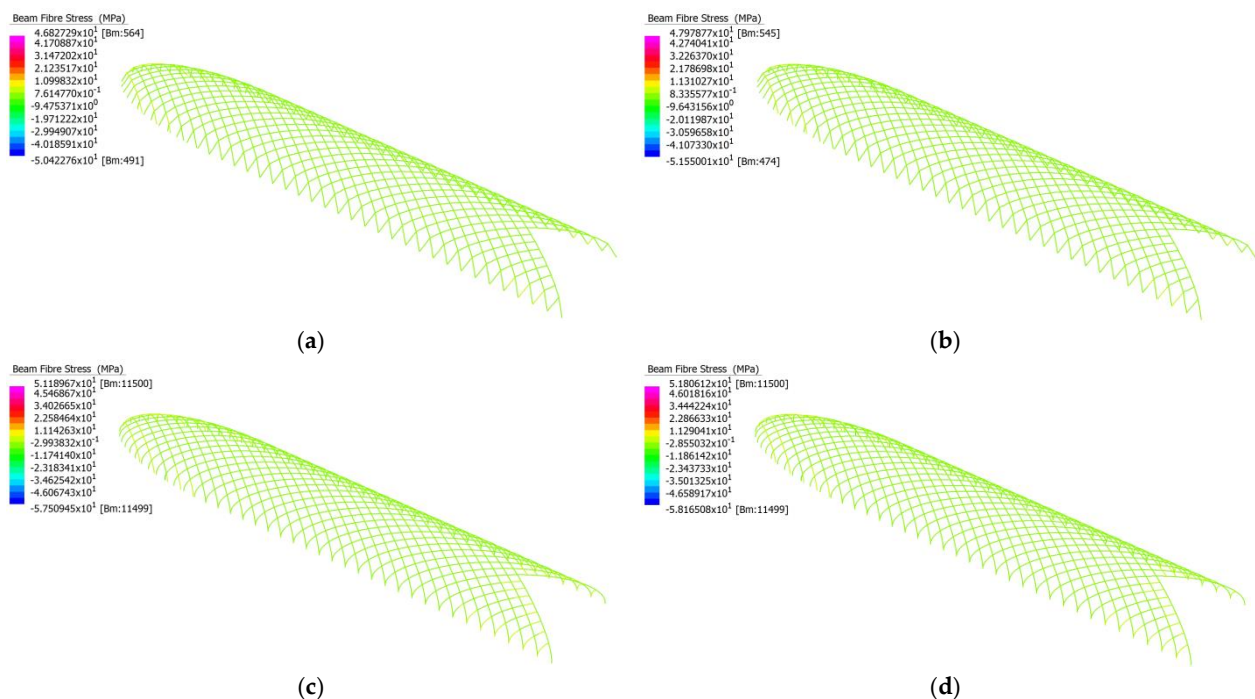
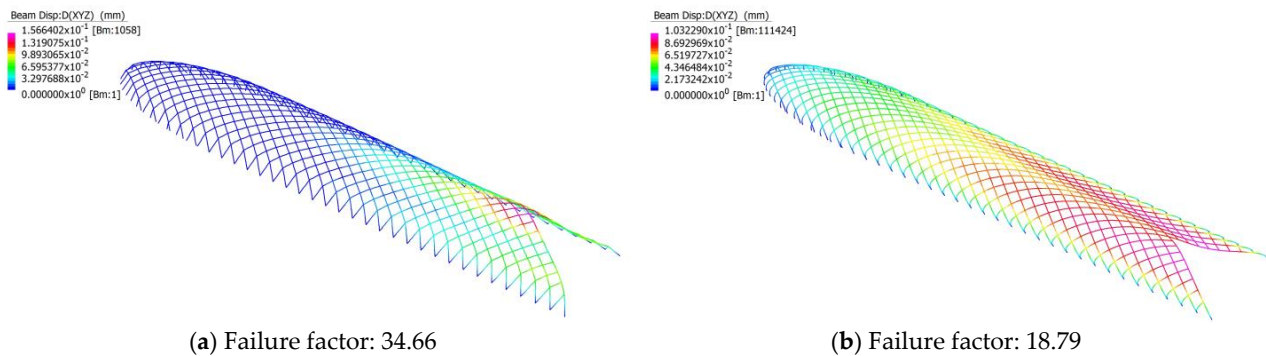


Figure 103. (a) Linear analysis of straight member model under load combination 1.35G; (b) Nonlinear analysis of straight member model under load combination 1.35G; (c) Linear analysis of curved member model under load combination 1.35G; (d) Nonlinear analysis of curved member model under load combination 1.35G.

From Figure 104, the straight and curved member models depict the same buckling failure as if under the load combination 1.2G + 1.5Q. For both models, the linear buckling failure factor is well above the load factors outlined in Table 29. The maximum load factor for the load combination 1.35G is therefore 5.69, from nonlinear static analysis of the curved member model.



(a) Failure factor: 34.66

(b) Failure factor: 18.79

Figure 104. (a) Linear buckling analysis of the straight member model under load combination 1.35G with D_{XYZ} displacement contour; (b) Linear buckling analysis of the curved member model under load combination 1.35G with D_{XYZ} displacement contour.

5.5.3. Load Combination 1.2G + W

Table 31 summarises the total fibres stress in beams for both the straight and curved models for both linear and nonlinear analysis, under the load combination 1.2G + W, while Table 32 summarises their displacements.

Table 31. Fibre stresses under 1.2G + W load combination.

Solver	Maximum Fibre Stress (MPa)		Difference (%)
	Straight Members	Curved Members	
Linear Static	−74.20	−133.58	44.45
Nonlinear Static	−75.22	−136.76	45.00
Nonlinear Static Load Factor	4.44	2.47	44.37

Table 32. Displacement under 1.2G + W load combination.

Solver	Straight Member Model Maximum Displacements (mm)			
	D_X	D_Y	D_Z	D_{XYZ}
Linear Static	3.92	25.20	−31.74	34.74
Nonlinear Static	3.98	25.54	−32.71	35.72
Solver	Curved Member Model Maximum Displacements (mm)			
	D_X	D_Y	D_Z	D_{XYZ}
Linear Static	5.85	48.53	−43.37	60.51
Nonlinear Static	6.02	50.15	−45.21	63.08

As shown in Table 31, the maximum fibre stress was 136 MPa, which came from linear static analysis of the curved model and was less than the 350 MPa yield limit. The difference in maximum fibre stress experienced by the 2 models was as much as 45 percent, which supports the idea that the outcome is highly dependent on the accuracy with which the structure is modelled. The maximum displacements in Table 32 are relatively small compared to the span, suggesting that the linear and nonlinear static analysis results are valid with the assumptions made.

From Figure 105, the structure exhibits similar behaviour when under the load combination 1.2G + 1.5Q, expect that for the straight model, the members at the rounded end experience more fibre stress.

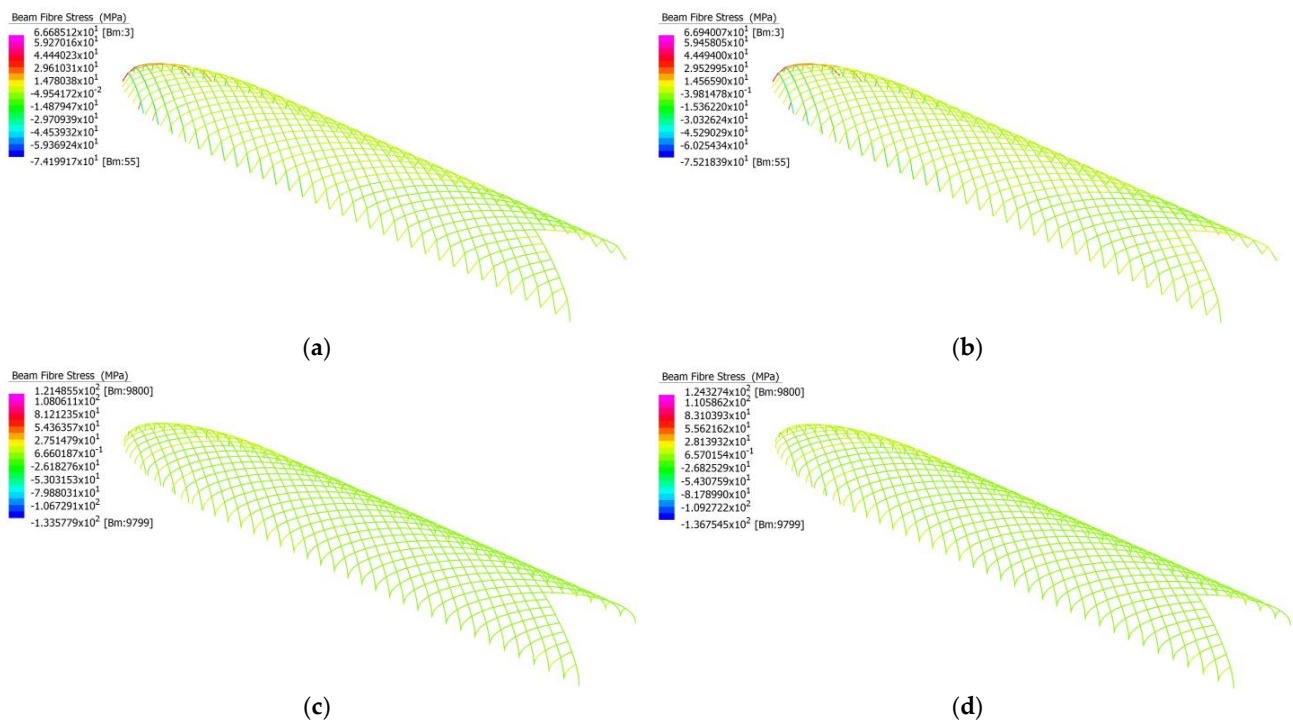


Figure 105. (a) Linear analysis of straight member model under load combination 1.2G + W; (b) Nonlinear analysis of straight member model under load combination 1.2G + W; (c) Linear analysis of curved member model under load combination 1.2G + W; (d) Nonlinear analysis of curved member model under load combination 1.2G + W.

Figure 106 depicts a similar buckling failure behaviour when under the load combination 1.2G + 1.5Q. For both models, the linear buckling failure factor is well above the load factors outlined in Table 31. The maximum load factor for the load combination 1.2G + W is therefore 2.47, from nonlinear static analysis of the curved member model.

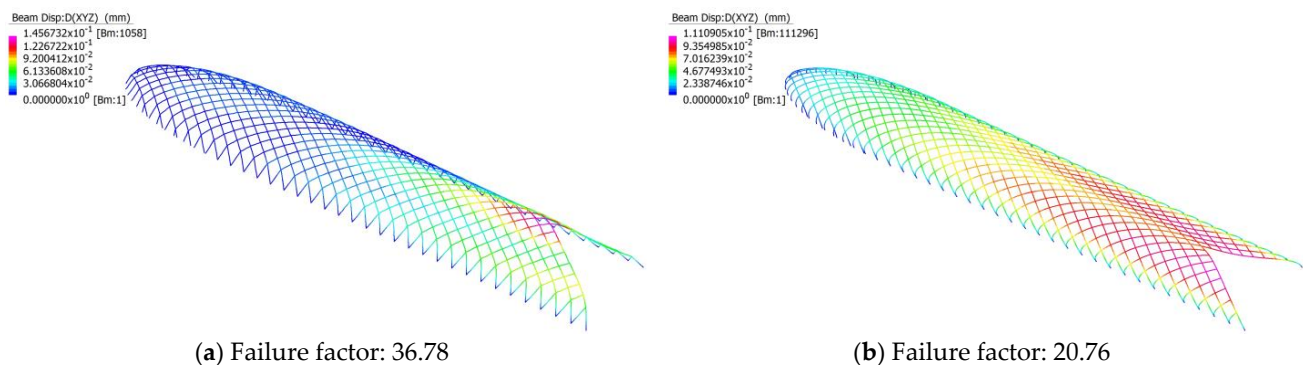


Figure 106. (a) Linear buckling analysis of the straight member model under load combination 1.2G + W with D_{XYZ} displacement contour; (b) Linear buckling analysis of the curved member model under load combination 1.2G + W with D_{XYZ} displacement contour.

6. Structural Behaviours under Serviceability Limit State

Each of the five models' performance is analysed under the serviceability limit state for each load combination case described in Table 33, for both the straight and curved member modes. To reiterate, according to AS1170.1 [61], the load combinations considered are $G + 0.7Q$ and $G + 0.7Q + W$. It is assumed that the glass on the surface is smooth enough to ignore the effects of wind friction. With the estimated dead load, live load, and wind load, the structural performance of each model and their straight and curved variations are tested using Strand7's Linear Static and Non-linear Static solvers.

Table 33. Phoenix International Media Center, Maximum structural displacement under serviceability limit state with results from linear static analysis.

Load Combination	Straight Member Model Maximum Displacements (mm)				
	D _X	D _Y	D _Z	D _{XY}	D _{XYZ}
G + 0.7Q	9.96	11.42	−28.18	11.81	28.53
G + 0.7Q + W	8.95	12.22	−30.25	12.71	30.69
Load Combination	Curved Member Model Maximum Displacements (mm)				
	D _X	D _Y	D _Z	D _{XY}	D _{XYZ}
G + 0.7Q	15.88	17.39	−43.64	17.91	44.18
G + 0.7Q + W	14.20	18.36	−46.13	19.13	46.76

6.1. Phoenix International Media Center in Beijing

6.1.1. Maximum Structural Displacement Using Linear Static Analysis

Table 33 summarises the maximum structural displacement in each load combination from linear static analysis of both straight and curved models. The structural displacement along the z-axis is significantly higher than the structural displacements along the x and y-axes, meaning that the serviceability limit state is governed by gravitational loads, indicating an over-reinforcement of the structure. This difference between the maximum x and y-axes displacements and the maximum displacement along the xy plane are negligible. For load combination **G + 0.7Q + W**, this indicates that the wind action only acts parallel to the axial directions. This is due to the way in which these wind actions are applied to the model described in Section 4.1.3. With a more rigorous application of wind actions, the maximum displacements within the xy plane are expected to increase significantly beyond the maximal displacements along the x and y-axes.

According to AS1170.0 [64], Table C1, the maximum deflection for *roof elements supporting brittle claddings* should be no greater than the span of the element divided by 400. The average continuous element within the structure was calculated from Grasshopper to be 108 m. Given this span, the maximum displacement tolerable is calculated in Equation (1):

$$v_{max} = \frac{108}{400} = 0.27 \text{ m} = 270 \text{ mm} \quad (1)$$

Under the serviceability limit state, the maximum total deflection $D_{XYZ, \max}$ was observed in the curved member model under the load combination **G + 0.7Q + W**, equal to 46.76 mm. The maximum total deflection was significantly smaller than the allowable displacement shown in Equation (1); hence, the structure is feasible in design. The total displacement in each beam is shown in Figure 107 for both straight and curved members. There is no visually discernible difference between the straight and curved member models, or between the two load combinations.

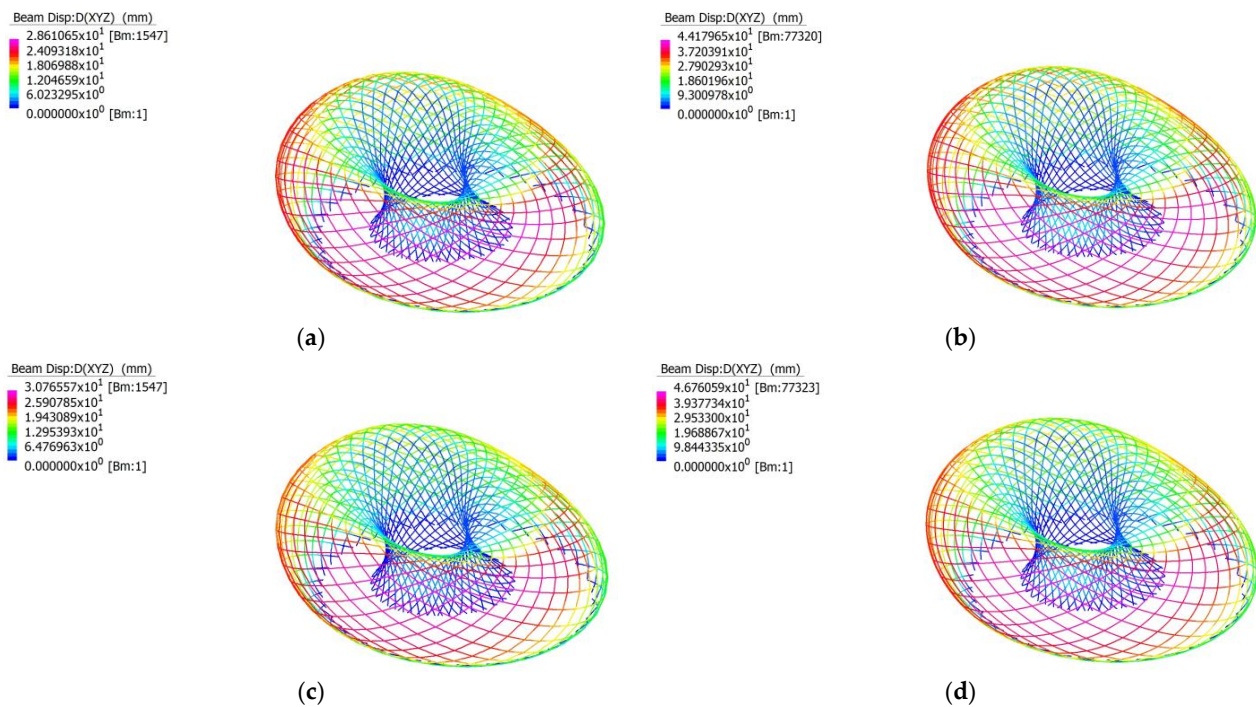


Figure 107. (a) Total beam displacement in the straight member model using linear static analysis, under load combination $G + 0.7Q$; (b) Total beam displacement in the curved member model using linear static analysis, under load combination $G + 0.7Q$; (c) Total beam displacement in the straight member model using linear static analysis, under load combination $G + 0.7Q + W$; (d) Total beam displacement in the curved member model using linear static analysis, under load combination $G + 0.7Q + W$.

6.1.2. Maximum Structural Displacement Using Non-Linear Static Analysis

Table 34 summarises the maximum structural displacement in each load combination from nonlinear static analysis of both straight and curved models. These results reinforce the findings discussed in Table 33, with the displacement along the z -axis significantly higher than the displacements along the x and y -axes, meaning that under serviceability load combinations, the critical load are gravitational forces. There is very little deviation between the maximum total displacement between the linear and nonlinear static analysis results. Both linear and nonlinear static analysis of straight and curved models reveal that the accuracy with which the beam elements are modelled are a determining factor in the performance of the structure, with the curved model experiencing significantly high maximum total displacement.

Table 34. Phoenix International Media Center, Maximum structural displacement under serviceability limit state with results from nonlinear static analysis.

Load Combination	Straight Member Model Maximum Displacements (mm)				
	D_X	D_Y	D_Z	D_{XY}	D_{XYZ}
$G + 0.7Q$	9.98	11.44	−28.26	11.83	28.61
$G + 0.7Q + W$	8.98	12.23	−30.31	12.73	30.75
Load Combination	Curved Member Model Maximum Displacements (mm)				
	D_X	D_Y	D_Z	D_{XY}	D_{XYZ}
$G + 0.7Q$	15.94	17.44	−43.83	17.97	44.37
$G + 0.7Q + W$	14.26	18.39	−46.29	19.17	46.91

According to AS1170.0 [64], Table C1, the maximum deflection for *roof elements supporting brittle claddings* should be no greater than the span of the element divided by 400.

The average continuous element within the structure was calculated to be 108 m. Given this span, the maximum displacement tolerable is calculated in Equation (2):

$$v_{max} = \frac{108}{400} = 0.27 \text{ m} = 270 \text{ mm} \quad (2)$$

Under the serviceability limit state, the maximum total deflection $D_{XYZ, \max}$ was observed in the curved member model under the load combination $G + 0.7Q + W$, equal to 46.91 mm. The maximum total deflection was significantly smaller than the allowable displacement shown in Equation (1); hence, the structure is feasible in design. The total displacement in each beam is shown in Figure 108 for both straight and curved members. There is no visually discernible difference between the straight and curved member models, or between the two load combinations.

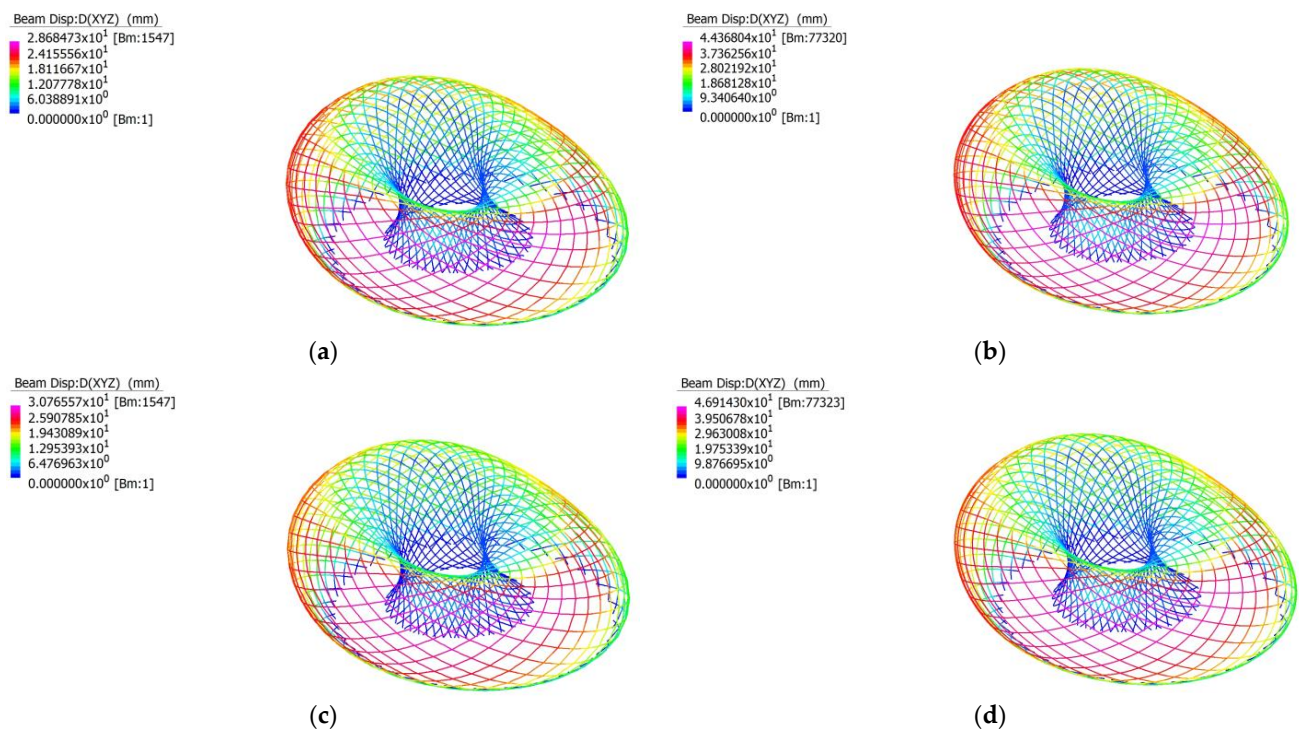


Figure 108. (a) Total beam displacement in the straight member model using nonlinear static analysis, under load combination $G + 0.7Q$; (b) Total beam displacement in the curved member model using nonlinear static analysis, under load combination $G + 0.7Q$; (c) Total beam displacement in the straight member model using nonlinear static analysis, under load combination $G + 0.7Q + W$; (d) Total beam displacement in the curved member model using nonlinear static analysis, under load combination $G + 0.7Q + W$.

6.1.3. Maximum Axial Stress in Members under Serviceability Limit State

The linear and nonlinear static results for the maximum axial stress in both straight and curved models under the two serviceability load combinations are shown in Table 35. Under the serviceability limit state, the maximum axial stress was -13.21 MPa, which is significantly less than the yield stress of 350 MPa. Hence, the designed structure is stable and will not experience plastic deformation under the serviceability limit state.

Table 35. Phoenix International Media Center, Maximum axial stress using both linear and non-linear static analysis.

Straight Member Model Using Straight Beam Elements		
Load Combination	Solver	Axial Stress (MPa)
G + 0.7Q	Linear Static	−12.90
G + 0.7Q	Non-linear Static	−12.90
G + 0.7Q + W	Linear Static	−10.60
G + 0.7Q + W	Non-linear Static	−10.07
Curved Member Model Using Straight Beam Elements		
Load Combination	Solver	Axial Stress (MPa)
G + 0.7Q	Linear Static	−13.11
G + 0.7Q	Non-linear Static	−13.21
G + 0.7Q + W	Linear Static	−10.68
G + 0.7Q + W	Non-linear Static	−10.71

6.2. Kazakhstan Pavilion and Science Museum

6.2.1. Maximum Structural Displacement Using Linear Static Analysis

Table 36 summarises the maximum structural displacement in each load combination from linear static analysis of both straight and curved models. The structural displacement along the *z*-axis is significantly higher than the structural displacements along the *x* and *y*-axes, meaning that the serviceability limit state is governed by gravitational loads, indicating an over-reinforcement of the structure. This difference between the maximum *x* and *y*-axes displacements and the maximum displacement along the *xy* plane are negligible. For load combination **G + 0.7Q + W**, this indicates that the wind action only acts parallel to the axial directions. This is due to the way in which these wind actions are applied to the model described in Section 4.1.3. With a more rigorous application of wind actions, the maximum displacements within the *xy* plane are expected to increase significantly beyond the maximal displacements along the *x* and *y*-axes. It should also be noted that there is a significant difference between the lateral maximum displacement in the *xy* plane between the two load combinations, meaning that the lateral deflections of the structure are highly dependent on wind load.

Table 36. Kazakhstan Pavilion and Science Museum, Maximum structural displacement under serviceability limit state with results from linear static analysis.

Load Combination	Straight Member Model Maximum Displacements (mm)				
	D _X	D _Y	D _Z	D _{XY}	D _{XYZ}
G + 0.7Q	20.60	30.46	−110.30	30.46	110.30
G + 0.7Q + W	15.63	58.94	−97.69	58.94	105.85
Load Combination	Curved Member Model Maximum Displacements (mm)				
	D _X	D _Y	D _Z	D _{XY}	D _{XYZ}
G + 0.7Q	32.74	44.07	−160.16	44.07	160.16
G + 0.7Q + W	32.33	94.52	−135.10	94.52	153.40

According to AS1170.0 [64], Table C1, the maximum deflection for *roof elements supporting brittle claddings* should be no greater than the span of the element divided by 400. The length of the continuous element within this section was calculated from Grasshopper to be 69 m. Given this span, the maximum displacement tolerable is calculated in Equation (3):

$$v_{max} = \frac{69}{400} = 0.17 \text{ m} = 170 \text{ mm} \quad (3)$$

Under the serviceability limit state, the maximum total deflection $D_{XYZ, \max}$ was observed in the curved member model under load combination $G + 0.7Q$, equal to 160.16 mm. The maximum total deflection is smaller than the allowable displacement shown in Equation (2); hence, the structure is feasible in design. The total displacement in each beam is shown in Figure 109 for both straight and curved members. From visual inspection, the wind load can be seen acting on the structure in such a way that it produces more total deflection on one side of the structure.

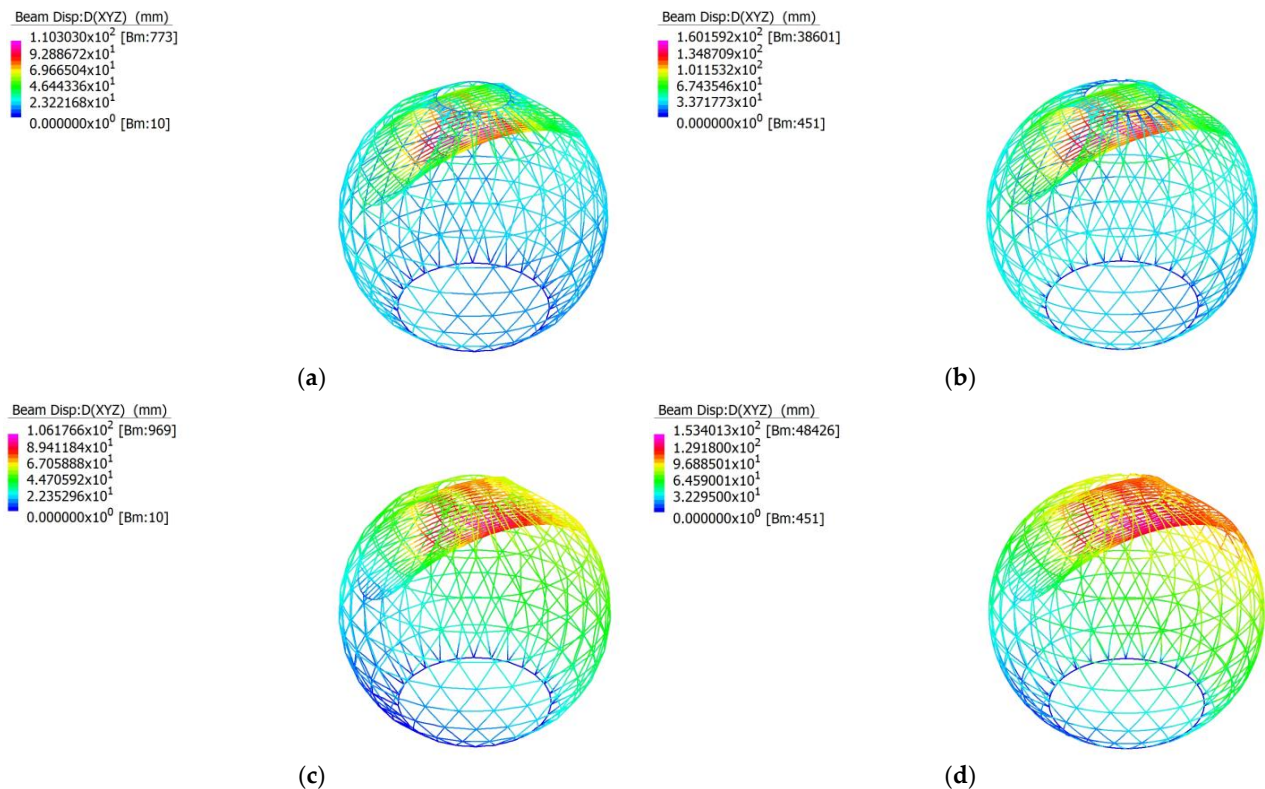


Figure 109. (a) Total beam displacement in the straight member model using linear static analysis, under load combination $G + 0.7Q$; (b) Total beam displacement in the curved member model using linear static analysis, under load combination $G + 0.7Q$; (c) Total beam displacement in the straight member model using linear static analysis, under load combination $G + 0.7Q + W$; (d) Total beam displacement in the curved member model using linear static analysis, under load combination $G + 0.7Q + W$.

6.2.2. Maximum Structural Displacement Using Non-Linear Static Analysis

Table 37 summarises the maximum structural displacement in each load combination from nonlinear static analysis of both straight and curved models. These results reinforce the findings discussed in Table 36. The displacement along the z -axis is significantly higher than the displacements along the x and y -axes, meaning that under serviceability load combinations, the critical load are gravitational forces. There is very little deviation between the maximum total displacement between linear and nonlinear static analysis results. Both linear and nonlinear static analysis of straight and curved models reveal that the accuracy with which the beam elements are modelled are a determining factor in the performance of the structure, with the curved model experiencing significantly high maximum total displacement.

Table 37. Kazakhstan Pavilion and Science Museum, Maximum structural displacement under serviceability limit state with results from nonlinear static analysis.

Load Combination	Straight Member Model Maximum Displacements (mm)				
	D _X	D _Y	D _Z	D _{XY}	D _{XYZ}
G + 0.7Q	20.79	30.44	−110.89	30.44	110.89
G + 0.7Q + W	15.77	59.30	−98.24	59.30	106.52
Load Combination	Curved Member Model Maximum Displacements (mm)				
	D _X	D _Y	D _Z	D _{XY}	D _{XYZ}
G + 0.7Q	32.98	44.09	−161.69	44.09	161.69
G + 0.7Q + W	34.46	99.55	−137.01	99.55	157.87

According to AS1170.0 [64], Table C1, the maximum deflection for *roof elements supporting brittle claddings* should be no greater than the span of the element divided by 400. The length of the continuous element within this section was calculated from Grasshopper to be 69 m. Given this span, the maximum displacement tolerable is calculated in Equation (4):

$$v_{max} = \frac{69}{400} = 0.17 \text{ m} = 170 \text{ mm} \quad (4)$$

Under the serviceability limit state, the maximum total deflection $D_{XYZ, \max}$ was observed in the curved member model under load combination G + 0.7Q + W, equal to 161.69 mm. The maximum total deflection was significantly smaller than the allowable displacement shown in Equation (1); hence, the structure is feasible in design. The total displacement in each beam is shown in Figure 110 for both straight and curved members. From visual inspection, the wind load can be seen acting on the structure in such a way that it produces more total deflection on one side of the structure.

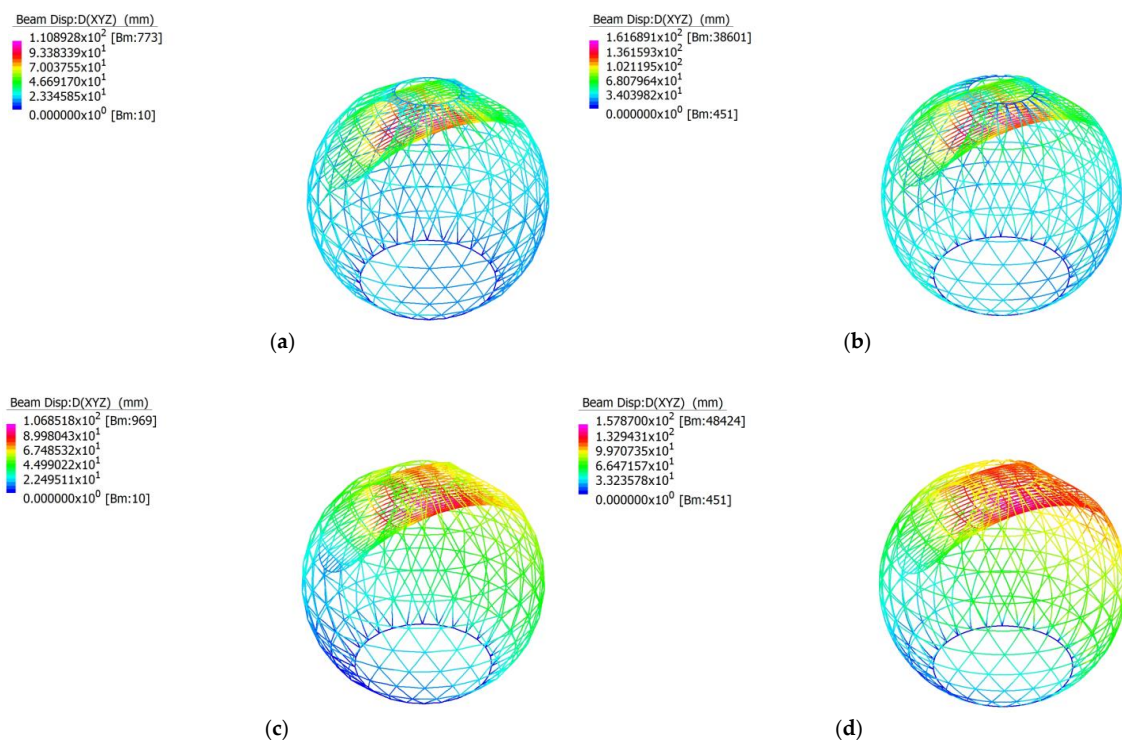


Figure 110. (a) Total beam displacement in the straight member model using nonlinear static analysis, under load combination G + 0.7Q; (b) Total beam displacement in the curved member model using nonlinear static analysis, under load combination G + 0.7Q; (c) Total beam displacement in the straight member model using nonlinear static analysis, under load combination G + 0.7Q + W; (d) Total beam displacement in the curved member model using nonlinear static analysis, under load combination G + 0.7Q + W.

6.2.3. Maximum Axial Stress in Members under Serviceability Limit State

The linear and nonlinear static results for the maximum axial stress in both straight and curved models under the two serviceability load combinations are shown in Table 38. Under the serviceability limit state the maximum axial stress was 114.47 MPa, which is less than the yield stress of 350 MPa. Hence, the designed structure is stable and will not experience plastic deformation under the serviceability limit state.

Table 38. Kazakhstan Pavilion and Science Museum, Maximum axial stress using both linear and non-linear static analysis.

Straight Member Model Using Straight Beam Elements		
Load Combination	Solver	Axial Stress (MPa)
G + 0.7Q	Linear Static	74.69
G + 0.7Q	Non-linear Static	75.19
G + 0.7Q + W	Linear Static	95.81
G + 0.7Q + W	Non-linear Static	99.96
Curved Member Model Using Straight Beam Elements		
Load Combination	Solver	Axial Stress (MPa)
G + 0.7Q	Linear Static	85.80
G + 0.7Q	Non-linear Static	87.26
G + 0.7Q + W	Linear Static	111.33
G + 0.7Q + W	Non-linear Static	114.47

6.3. Moynihan Train Hall

6.3.1. Maximum Structural Displacement Using Linear Static Analysis

Table 39 summarises the maximum structural displacement in each load combination from linear static analysis of both straight and curved models. The structural displacement along the z-axis is significantly higher than the structural displacements along the x and y-axes, meaning that the serviceability limit state is governed by gravitational loads, indicating an over-reinforcement of the structure. This difference between the maximum x and y-axes displacements and the maximum displacement along the xy plane are negligible. For load combination G + 0.7Q + W, this indicates that the wind action only acts parallel to the axial directions. This is due to the way in which these wind actions are applied to the model described in Section 4.1.3. With a more rigorous application of wind actions, the maximum displacements within the xy plane may increase significantly beyond the maximal displacements along the x and y-axes. It should also be noted that there is a significant difference between the lateral maximum displacement in the xy plane between the two load combinations, meaning that the lateral deflections of the structure are highly dependent on wind load.

Table 39. Moynihan Train Hall, Maximum structural displacement under serviceability limit state with results from linear static analysis.

Load Combination	Straight Member Model Maximum Displacements (mm)				
	D _X	D _Y	D _Z	D _{XY}	D _{XYZ}
G + 0.7Q	1.03	1.40	−2.87	1.40	3.20
G + 0.7Q + W	1.78	3.07	6.04	3.07	6.78
Load Combination	Curved Member Model Maximum Displacements (mm)				
	D _X	D _Y	D _Z	D _{XY}	D _{XYZ}
G + 0.7Q	1.06	1.42	−2.93	1.43	3.26
G + 0.7Q + W	1.83	3.13	6.16	3.13	6.91

According to AS1170.0 [64], Table C1, the maximum deflection for *roof elements supporting brittle claddings* should be no greater than the span of the element divided by 400. The length

of the continuous element within this section was calculated from Grasshopper to be 11 m. Given this span, the maximum displacement tolerable is calculated in Equation (5):

$$v_{max} = \frac{11}{400} = 0.028 \text{ m} = 28 \text{ mm} \quad (5)$$

Under the serviceability limit state, the maximum total deflection $D_{XYZ, \max}$ was observed in the curved member model under load combination $G + 0.7Q$, equal to 6.91 mm. The maximum total deflection is smaller than the allowable displacement shown in Equation (2); hence, the structure is feasible in design. The total displacement in each beam is shown in Figure 111 for both straight and curved members. There is no visually discernible difference between straight and curved member models, or between the two load combinations.

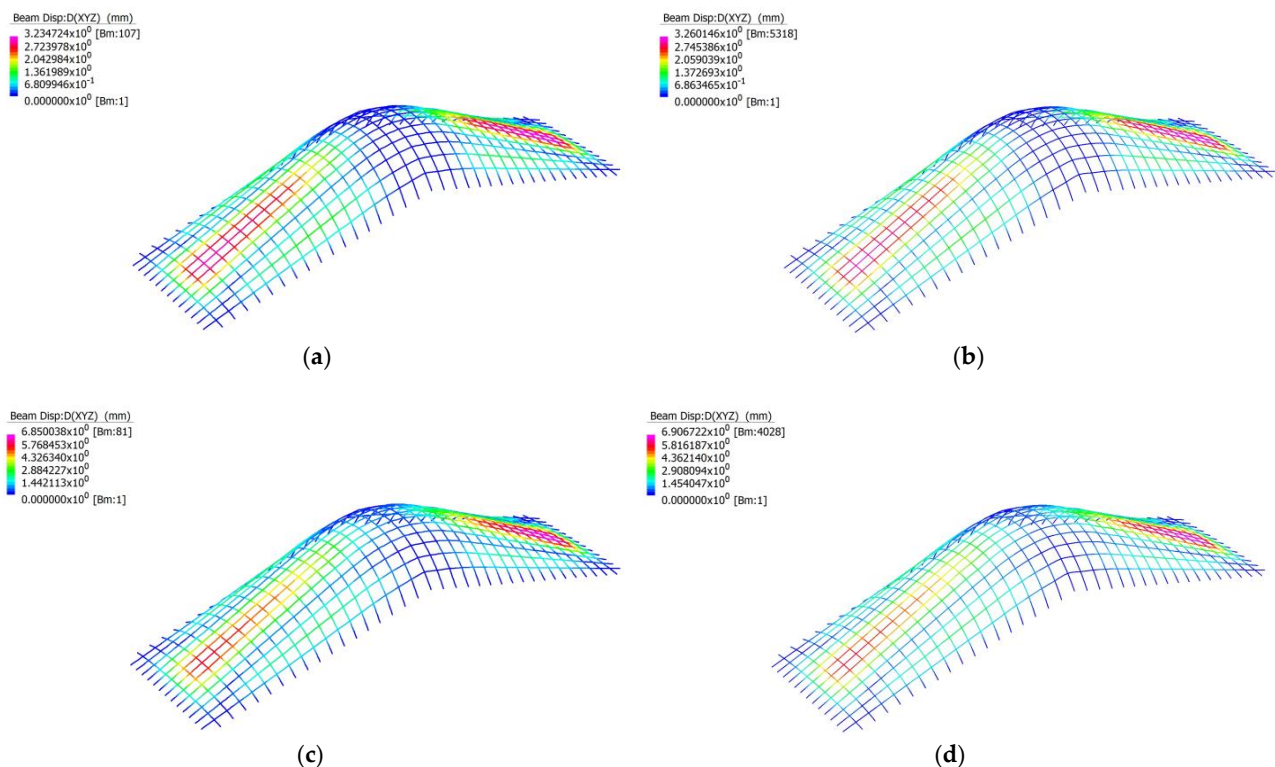


Figure 111. (a) Total beam displacement in the straight member model using linear static analysis, under load combination $G + 0.7Q$; (b) Total beam displacement in the curved member model using linear static analysis, under load combination $G + 0.7Q$; (c) Total beam displacement in the straight member model using linear static analysis, under load combination $G + 0.7Q + W$; (d) Total beam displacement in the curved member model using linear static analysis, under load combination $G + 0.7Q + W$.

6.3.2. Maximum Structural Displacement Using Non-Linear Static Analysis

Table 40 summarises the maximum structural displacement in each load combination from nonlinear static analysis of both straight and curved models. These results reinforce the findings discussed in Table 39. The displacement along the z -axis is significantly higher than the displacements along the x and y -axes, meaning that under serviceability load combinations, the critical load are gravitational forces. There is very little deviation between the maximum total displacement between linear and nonlinear static analysis results. Both linear and nonlinear static analysis of straight and curved models reveal that the accuracy with which the beam elements are modelled are not a determining factor in the performance of the structure, with the curved model experiencing similar maximum total displacement to that of the straight model.

Table 40. Moynihan Train Hall, Maximum structural displacement under serviceability limit state with results from nonlinear static analysis.

Load Combination	Straight Member Model Maximum Displacements (mm)				
	D _X	D _Y	D _Z	D _{XY}	D _{XYZ}
G + 0.7Q	1.05	1.45	−2.98	1.45	3.32
G + 0.7Q + W	1.71	2.91	5.71	2.91	6.41
Load Combination	Curved Member Model Maximum Displacements (mm)				
	D _X	D _Y	D _Z	D _{XY}	D _{XYZ}
G + 0.7Q	1.08	1.48	−3.05	1.48	3.39
G + 0.7Q + W	1.75	2.95	5.79	2.96	6.50

According to AS1170.0 [64], Table C1, the maximum deflection for *roof elements supporting brittle claddings* should be no greater than the span of the element divided by 400. The length of the continuous element within this section was calculated from Grasshopper to be 11 m. Given this span, the maximum displacement tolerable is calculated in Equation (6):

$$v_{max} = \frac{11}{400} = 0.028 \text{ m} = 28 \text{ mm} \quad (6)$$

Under the serviceability limit state, the maximum total deflection $D_{XYZ, \max}$ was observed in the curved member model under the load combination G + 0.7Q + W, equal to 6.50 mm. The maximum total deflection was significantly smaller than the allowable displacement shown in Equation (1); hence, the structure is feasible in design. The total displacement in each beam is shown in Figure 112 for both straight and curved members. There is no visually discernible difference between straight and curved member models, or between the two load combinations.

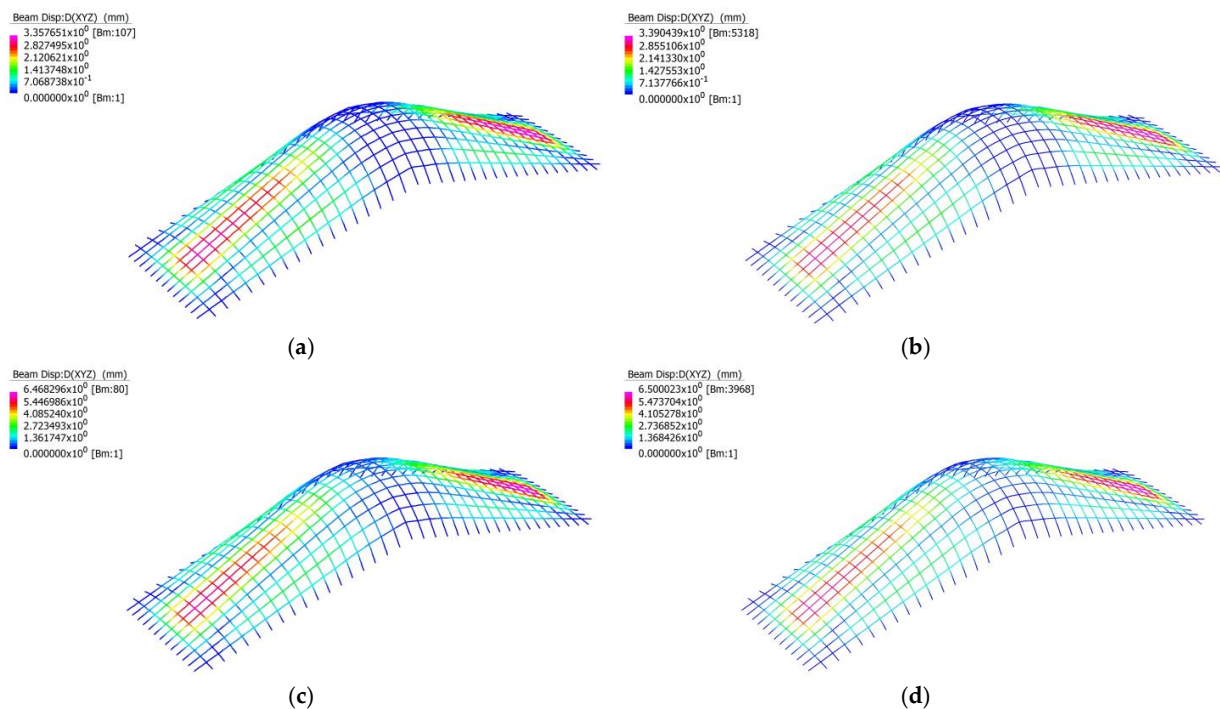


Figure 112. (a) Total beam displacement in the straight member model using nonlinear static analysis, under load combination G + 0.7Q; (b) Total beam displacement in the curved member model using nonlinear static analysis, under load combination G + 0.7Q; (c) Total beam displacement in the straight member model using nonlinear static analysis, under load combination G + 0.7Q + W; (d) Total beam displacement in the curved member model using nonlinear static analysis, under load combination G + 0.7Q + W.

6.3.3. Maximum Axial Stress in Members under Serviceability Limit State

The linear and nonlinear static results for the maximum axial stress in both straight and curved models under the two serviceability load combinations are shown in Table 41. Under serviceability limit state the maximum axial stress was 15.44 MPa, which is less than the yield stress of 350 MPa. Hence, the designed structure is stable and will not experience plastic deformation under the serviceability limit state.

Table 41. Moynihan Train Hall, Maximum axial stress using both linear and non-linear static analysis.

Straight Member Model Using Straight Beam Elements		
Load Combination	Solver	Axial Stress (MPa)
G + 0.7Q	Linear Static	−7.41
G + 0.7Q	Non-linear Static	−7.44
G + 0.7Q + W	Linear Static	15.35
G + 0.7Q + W	Non-linear Static	15.31
Curved Member Model Using Straight Beam Elements		
Load Combination	Solver	Axial Stress (MPa)
G + 0.7Q	Linear Static	−7.43
G + 0.7Q	Non-linear Static	−7.46
G + 0.7Q + W	Linear Static	15.44
G + 0.7Q + W	Non-linear Static	15.40

6.4. Chadstone Shopping Centre

6.4.1. Maximum Structural Displacement Using Linear Static Analysis

Table 42 summarises the maximum structural displacement in each load combination from linear static analysis of both straight and curved models. The structural displacement along the z-axis is similar to the structural displacements along the x and y-axes, meaning that the serviceability limit state is governed by both gravitational and wind loads. This difference between the maximum x and y-axes displacements and the maximum displacement along the xy plane are significant. For load combination **G + 0.7Q + W**, this indicates that the wind action acts across many directions. This is due to the way in which these wind actions are applied to the model described in Section 4.1.3. With a more rigorous application of wind actions, the maximum displacements within the xy plane may increase. It should also be noted that there is a significant difference between the lateral maximum displacement in the xy plane between the two load combinations, meaning that the lateral deflections of the structure are highly dependent on wind load. There is also a large difference between the z axial displacement, indicating that the wind uplifts the entire structure.

Table 42. Chadstone shopping mall, Maximum structural displacement under serviceability limit state with results from linear static analysis.

Load Combination	Straight Member Model Maximum Displacements (mm)				
	D _X	D _Y	D _Z	D _{XY}	D _{XYZ}
G + 0.7Q	14.52	12.58	−12.33	19.21	22.55
G + 0.7Q + W	46.89	54.15	42.27	68.42	80.43
Load Combination	Curved Member Model Maximum Displacements (mm)				
	D _X	D _Y	D _Z	D _{XY}	D _{XYZ}
G + 0.7Q	14.78	13.04	−27.10	17.30	27.31
G + 0.7Q + W	49.67	47.75	39.09	63.64	74.62

According to AS1170.0 [64], Table C1, the maximum deflection for *roof elements supporting brittle claddings* should be no greater than the span of the element divided by 400. At the location of greatest total displacement, the shortest continuous span was calculated

from Grasshopper to be 40 m. Given this span, the maximum displacement tolerable is calculated in Equation (7):

$$v_{max} = \frac{40}{400} = 0.1 \text{ m} = 100 \text{ mm} \quad (7)$$

Under serviceability limit state, the maximum total deflection $D_{XYZ, \max}$ was observed in the straight member model under load combination $G + 0.7Q + W$, equal to 80.43 mm. The maximum total deflection is smaller than the allowable displacement shown in Equation (2). Hence, the structure is feasible in design. The total displacement in each beam is shown in Figure 113 for both straight and curved members. Visually, there is a difference between the two load combinations, as the wind load results in more displacement on the inner side of the model. For load combination $G + 0.7Q$, the curved model displays more accuracy as too which sections of the model are under larger displacements.

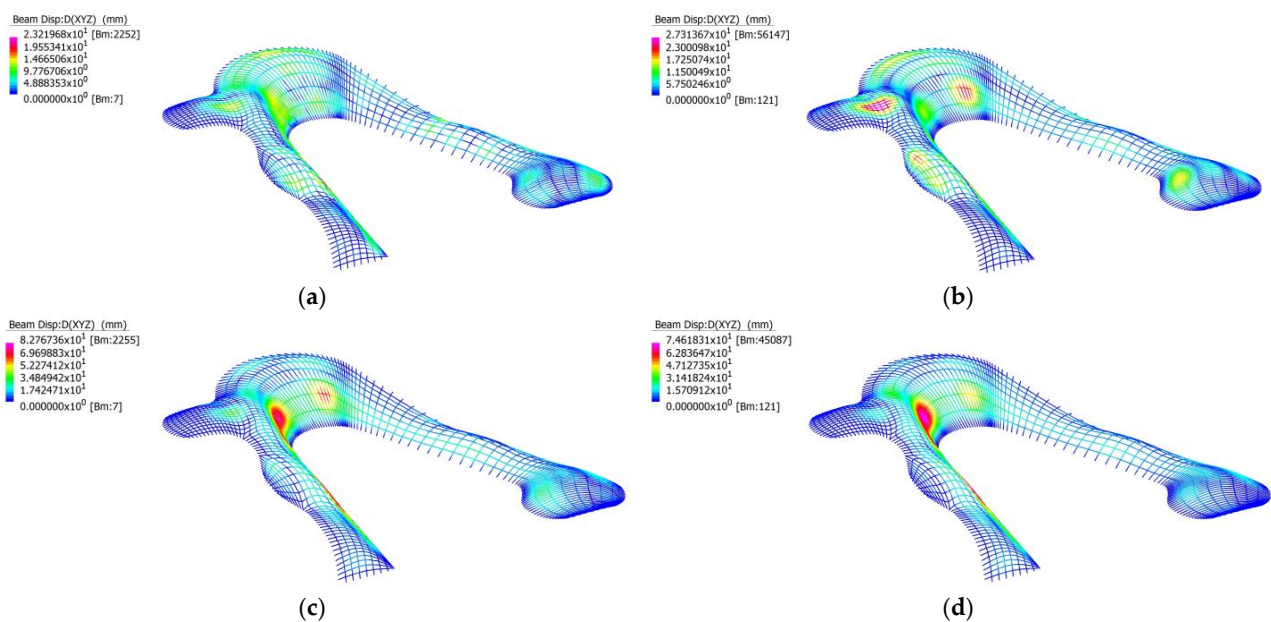


Figure 113. (a) Total beam displacement in the straight member model using linear static analysis, under load combination $G + 0.7Q$; (b) Total beam displacement in the curved member model using linear static analysis, under load combination $G + 0.7Q$; (c) Total beam displacement in the straight member model using linear static analysis, under load combination $G + 0.7Q + W$; (d) Total beam displacement in the curved member model using linear static analysis, under load combination $G + 0.7Q + W$.

6.4.2. Maximum Structural Displacement Using Non-Linear Static Analysis

Table 43 summarises the maximum structural displacement in each load combination from nonlinear static analysis of both straight and curved models. These results reinforce the findings discussed in Table 42. The displacement along the z-axis is significantly higher than the displacements along the x and y-axes for load combination $G + 0.7Q$, while under load combination $G + 0.7Q + W$, the maximum displacements across all 3 axes remains similar, meaning that under serviceability load combinations, gravitational and wind loads are critical. There is very little deviation between the maximum total displacement between linear and nonlinear static analysis results. Both linear and nonlinear static analysis of straight and curved models reveal that the accuracy with which the beam elements are modelled are not a determining factor in the performance of the structure, with the curved model experiencing similar maximum total displacement to that of the straight model.

Table 43. Chadstone shopping mall, Maximum structural displacement under serviceability limit state with results from nonlinear static analysis.

Load Combination	Straight Member Model Maximum Displacements (mm)				
	D _X	D _Y	D _Z	D _{XY}	D _{XYZ}
G + 0.7Q	14.67	12.76	−12.68	19.44	22.86
G + 0.7Q + W	23.56	49.65	40.34	62.97	73.80
Load Combination	Curved Member Model Maximum Displacements (mm)				
	D _X	D _Y	D _Z	D _{XY}	D _{XYZ}
G + 0.7Q	15.41	14.22	−28.76	18.74	29.00
G + 0.7Q + W	48.78	44.49	38.32	61.82	71.81

According to AS1170.0 [64], Table C1, the maximum deflection for *roof elements supporting brittle claddings* should be no greater than the span of the element divided by 400. At the location of greatest total displacement, the shortest continuous span was calculated from Grasshopper to be 40 m. Given this span, the maximum displacement tolerable is calculated in Equation (8):

$$v_{max} = \frac{40}{400} = 0.1 \text{ m} = 100 \text{ mm} \quad (8)$$

Under the serviceability limit state, the maximum total deflection $D_{XYZ, \max}$ was observed in the straight member model under load combination G + 0.7Q + W, equal to 73.80 mm. The maximum total deflection is smaller than the allowable displacement shown in Equation (2); hence, the structure is feasible in design. The total displacement in each beam is shown in Figure 114 for both straight and curved members. Visually, there is a difference between the two load combinations, as the wind load results in more displacement on the inner side of the model. For load combination G + 0.7Q, the curved model displays more accuracy as too which sections of the model are under larger displacements.

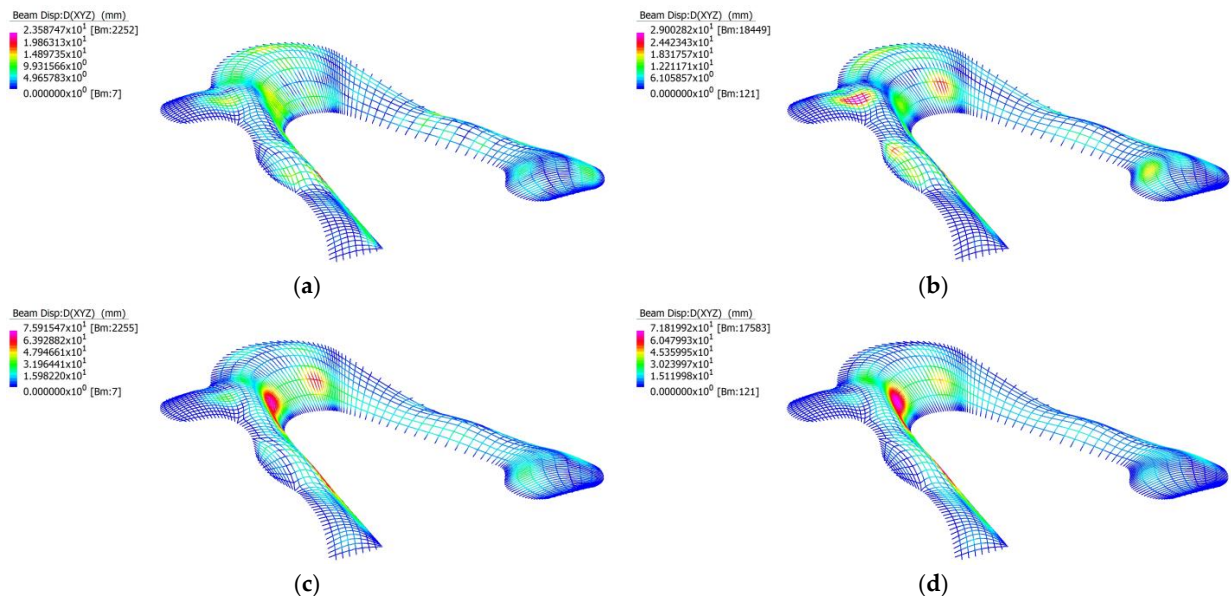


Figure 114. (a) Total beam displacement in the straight member model using nonlinear static analysis, under load combination G + 0.7Q; (b) Total beam displacement in the curved member model using nonlinear static analysis, under load combination G + 0.7Q; (c) Total beam displacement in the straight member model using nonlinear static analysis, under load combination G + 0.7Q + W; (d) Total beam displacement in the curved member model using nonlinear static analysis, under load combination G + 0.7Q + W.

6.4.3. Maximum Axial Stress in Members under Serviceability Limit State

The linear and nonlinear static results for the maximum axial stress in both straight and curved models under the two serviceability load combinations are shown in Table 44. Under the serviceability limit state the maximum axial stress was 36.37 MPa, which is less than the yield stress of 350 MPa. Hence, the designed structure is stable and will not experience plastic deformation under the serviceability limit state.

Table 44. Chadstone shopping mall, Maximum axial stress using both linear and non-linear static analysis.

Straight Member Model Using Straight Beam Elements		
Load Combination	Solver	Axial Stress (MPa)
G + 0.7Q	Linear Static	24.94
G + 0.7Q	Non-linear Static	25.20
G + 0.7Q + W	Linear Static	−36.37
G + 0.7Q + W	Non-linear Static	−35.79
Curved Member Model Using Straight Beam Elements		
Load Combination	Solver	Axial Stress (MPa)
G + 0.7Q	Linear Static	−21.63
G + 0.7Q	Non-linear Static	−21.59
G + 0.7Q + W	Linear Static	−26.99
G + 0.7Q + W	Non-linear Static	−26.71

6.5. The Hague Central Station Light Rail Station

6.5.1. Maximum Structural Displacement Using Linear Static Analysis

Table 45 summarises the maximum structural displacement in each load combination from linear static analysis of both straight and curved models. The structural displacement along the z -axis is similar to the structural displacements along the x and y -axes, meaning that the serviceability limit state is governed by both gravitational and wind loads. This difference between the maximum x and y -axes displacements and the maximum displacement along the xy plane are significant. For load combination $G + 0.7Q + W$, this indicates that the wind action only acts across many directions. This is due to the way in which these wind actions are applied to the model described in Section 4.1.3. With a more rigorous application of wind actions, the maximum displacements within the xy plane may increase. It should also be noted that there is a significant difference between the lateral maximum displacement in the xy plane between the two load combinations, meaning that the lateral deflections of the structure are highly dependent on wind load. There is also a large difference between the z axial displacements, indicating that the wind uplifts the entire structure.

Table 45. The Hague Central Station light rail station, Maximum structural displacement under serviceability limit state with results from linear static analysis.

Load Combination	Straight Member Model Maximum Displacements (mm)				
	D_x	D_y	D_z	D_{xy}	D_{xyz}
G + 0.7Q	3.41	16.56	−35.94	16.56	35.94
G + 0.7Q + W	4.37	28.40	−38.60	28.40	41.12
Load Combination	Curved Member Model Maximum Displacements (mm)				
	D_x	D_y	D_z	D_{xy}	D_{xyz}
G + 0.7Q	3.33	19.23	−40.24	19.23	40.24
G + 0.7Q + W	6.06	51.23	−48.09	51.23	63.84

According to AS1170.0 [64], Table C1, the maximum deflection for *roof elements supporting brittle claddings* should be no greater than the span of the element divided by 400.

At the location of greatest total displacement, the shortest continuous span was calculated from Grasshopper to be 32 m. Given this span, the maximum displacement tolerable is calculated in Equation (9):

$$v_{max} = \frac{32}{400} = 0.08m = 80mm \quad (9)$$

Under the serviceability limit state, the maximum total deflection $D_{XYZ, max}$ was observed in the straight member model under load combination $G + 0.7Q + W$, equal to 63.84 mm. The maximum total deflection is smaller than the allowable displacement shown in Equation (2); hence, the structure is feasible in design. The total displacement in each beam is shown in Figure 115 for both straight and curved members. Visually, there is a difference between the two load combinations, as the wind load results in more displacement on one side of the model. There appears to be no difference between straight and curved models.

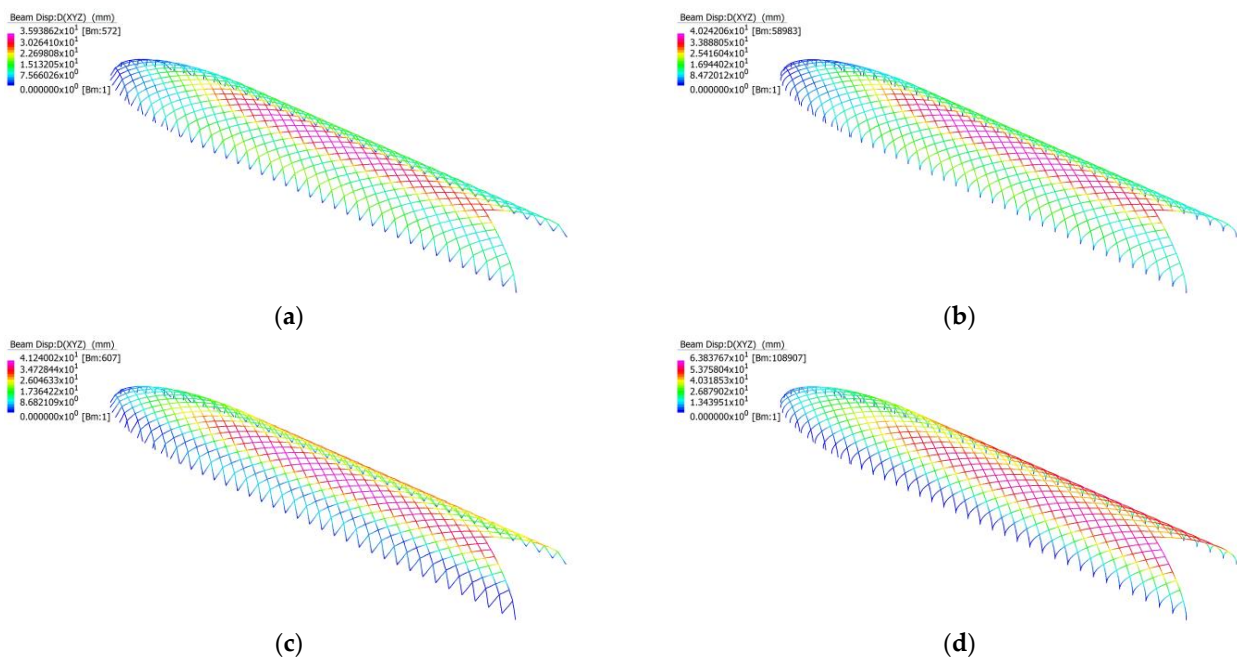


Figure 115. (a) Total beam displacement in the straight member model using linear static analysis, under load combination $G + 0.7Q$; (b) Total beam displacement in the curved member model using linear static analysis, under load combination $G + 0.7Q$; (c) Total beam displacement in the straight member model using linear static analysis, under load combination $G + 0.7Q + W$; (d) Total beam displacement in the curved member model using linear static analysis, under load combination $G + 0.7Q + W$.

6.5.2. Maximum Structural Displacement Using Non-Linear Static Analysis

Table 46 summarises the maximum structural displacement in each load combination from nonlinear static analysis of both straight and curved models. These results reinforce the findings discussed in Table 45. With the structural displacement along the z -axis being similar to the structural displacements along the x and y -axes. There is very little deviation between the maximum total displacement between linear and nonlinear static analysis results. Both linear and nonlinear static analysis of straight and curved models reveal that the accuracy with which the beam elements are modelled are a determining factor in the performance of the structure, with the curved model experiencing significantly high maximum total displacement.

Table 46. The Hague Central Station light rail station, Maximum structural displacement under serviceability limit state with results from nonlinear static analysis.

Load Combination	Straight Member Model Maximum Displacements (mm)				
	D _X	D _Y	D _Z	D _{XY}	D _{XYZ}
G + 0.7Q	3.48	16.99	−37.34	16.99	37.34
G + 0.7Q + W	4.46	28.92	−40.08	28.92	42.58
Load Combination	Curved Member Model Maximum Displacements (mm)				
	D _X	D _Y	D _Z	D _{XY}	D _{XYZ}
G + 0.7Q	3.42	19.74	−41.88	19.74	41.88
G + 0.7Q + W	6.27	53.33	−50.43	53.34	67.05

According to AS1170.0 [64], Table C1, the maximum deflection for *roof elements supporting brittle claddings* should be no greater than the span of the element divided by 400. The average continuous element within the structure was calculated to be 32 m. Given this span, the maximum displacement tolerable is calculated in Equation (10):

$$v_{max} = \frac{32}{400} = 0.08 \text{ m} = 80 \text{ mm} \quad (10)$$

Under the serviceability limit state, the maximum total deflection $D_{XYZ, \max}$ was observed in the curved member model under load combination G + 0.7Q + W, equal to 67.05 mm. The maximum total deflection was significantly smaller than the allowable displacement shown in Equation (1); hence, the structure is feasible in design. The total displacement in each beam is shown in Figure 116 for both straight and curved members. Visually, there is a difference between the two load combinations, as the wind load results in more displacement on one side of the model. There appears to be no difference between straight and curved models.

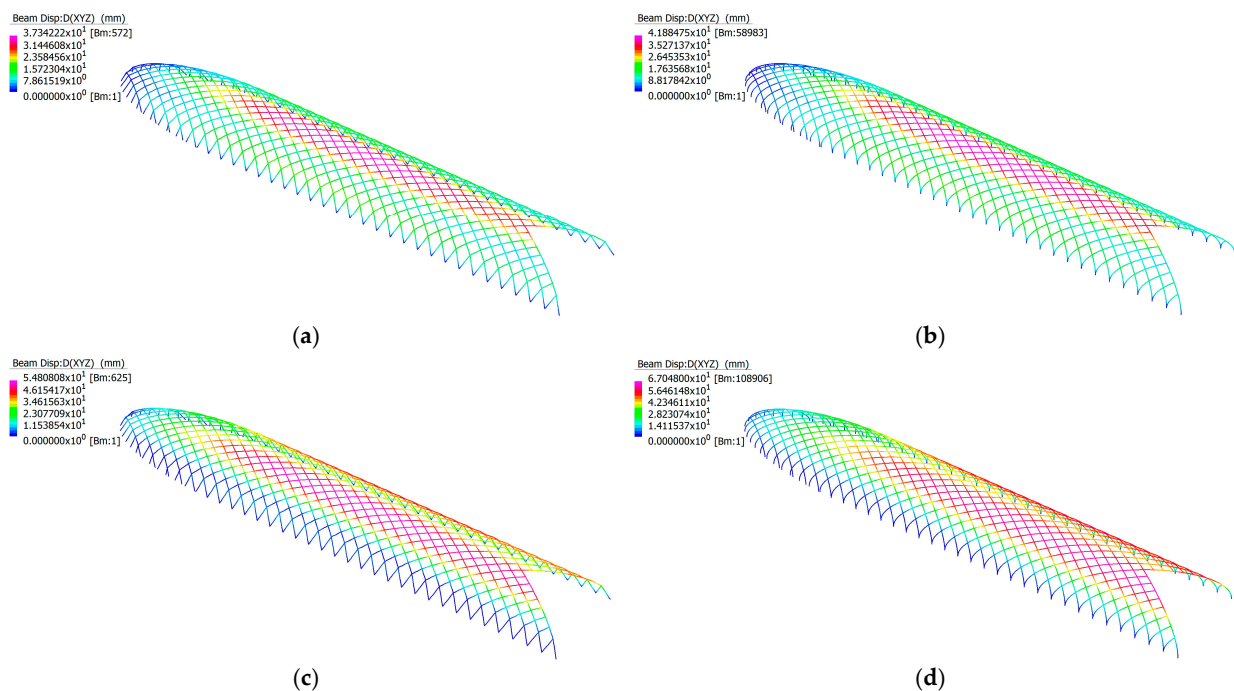


Figure 116. (a) Total beam displacement in the straight member model using nonlinear static analysis, under load combination G + 0.7Q; (b) Total beam displacement in the curved member model using nonlinear static analysis, under load combination G + 0.7Q; (c) Total beam displacement in the straight member model using nonlinear static analysis, under load combination G + 0.7Q + W; (d) Total beam displacement in the curved member model using nonlinear static analysis, under load combination G + 0.7Q + W.

6.5.3. Maximum Axial Stress in Members under Serviceability Limit State

The linear and nonlinear static results for the maximum axial stress in both straight and curved models under the two serviceability load combinations are shown in Table 47. Under the serviceability limit state the maximum axial stress was 43.05 MPa, which is less than the yield stress of 350 MPa. Hence, the designed structure is stable and will not experience plastic deformation under the serviceability limit state.

Table 47. The Hague Central Station light rail station, Maximum axial stress using both linear and non-linear static analysis.

Straight Member Model Using Straight Beam Elements		
Load Combination	Solver	Axial Stress (MPa)
G + 0.7Q	Linear Static	−4.73
G + 0.7Q	Non-linear Static	−4.73
G + 0.7Q + W	Linear Static	42.55
G + 0.7Q + W	Non-linear Static	43.05
Curved Member Model Using Straight Beam Elements		
Load Combination	Solver	Axial Stress (MPa)
G + 0.7Q	Linear Static	−7.29
G + 0.7Q	Non-linear Static	−7.34
G + 0.7Q + W	Linear Static	−21.66
G + 0.7Q + W	Non-linear Static	−22.38

7. Conclusions

7.1. Main Findings

This paper describes a technique for developing models that would be well suited for conducting additional research on curved steel–glass façades. In each case study, an approximate model was created using Rhino 7’s Grasshopper visual programming editor and then exported to Strand7 for analysis under both strength and serviceability loads per AS1170.0. Rhino 7’s Grasshopper and its community-made plugins facilitate parametric structures modelling by allowing design choices to be made throughout the modelling process. A numerical analysis of curved steel–glass façades can be challenging using Strand7’s internal modelling tools, which is why this method is applicable.

From the results of all the case studies discussed in this paper, it is evident that the proposed method is well-suited for the analysis of the effects of beam curvature on the global behaviour of curved steel–glass structures. The study found that in every case, the curve member model was more critical than its straight member counterpart, indicating that beam curvature significantly affects a structure’s overall performance. It should be noted that although all models performed well under the specified loads in this study, the wind loads applied were relatively simplistic due to the limitations of the software and the availability of data at the locations of the case study. Consequently, the results may only partially reflect the structures’ actual behaviour when subjected to more complex and realistic wind conditions. Under load combinations, 1.2G + W, the Kazakhstan Pavilion and The Hague Central Station light rail station showed the most significant differences in performance between the straight and curved member models, where wind loads played an important role. Evidence indicates that curved members may be more susceptible to lateral loads, underlining the importance of considering wind loads when designing curved steel–glass structures.

7.2. Further Research

The paper presents a clear workflow for analysing steel–glass structural members using Rhino 7, Grasshopper, and Strand7, in addition to introducing several relevant disciplines relating to real-world engineering challenges, such as structural design and

architectural design. The proposed integrated workflow offers additional research opportunities in advanced structural analysis, parametric design (complex curved structural design), and Building Information Modelling (BIM). As a result, multiple possible directions for future research are suggested in this paper.

7.3. For Advanced Structural Analysis Aspect

The analysis presented in [1] investigates the local buckling behaviour of straight and curved members. It is recommended that the proposed workflow be enhanced by including another finite element analysis software, such as Abaqus, to improve further the ability to analyse local member behaviour. By integrating these two systems, we will be able to examine the structural behaviour of the entire system in a more comprehensive manner, which will lead to a better understanding of member loading performance and optimisation potential.

The effect of different boundary conditions on the behaviour of light steel curve members could also be investigated under different load combinations. Research can be improved by modifying the type and location of the supports and loads applied to the structure to understand better how boundary conditions affect the overall behaviour of the member. Additionally, it is also possible to investigate the effects of different types of loads, including static, dynamic, and impact loads, on the behaviour of light steel curve members. The results of this research provide insight into potential failure modes and may lead to the development of designs that can withstand a more comprehensive range of loading conditions.

A digital model in this paper has been designed to facilitate the numerical analysis process, and the goal is to study global structural behaviour; however, specific details, such as glass panels and steel–glass and steel connections, have been simplified. As part of future research, we would like to investigate the modelling of curved plates (glass panels) as well as joints (steel–glass and –steel), in addition to the curved beams. Using this method will allow for a more comprehensive and accurate representation of the structural system, leading to more accurate analysis results and a better understanding of the global and local behaviour of the system under a variety of loading conditions.

Furthermore, advanced FEA techniques, such as nonlinear and dynamic analyses, may be used to design light steel curve members subjected to extreme loads such as earthquakes or windstorms.

It would be beneficial to investigate the effects of temperature on the behaviour of light steel curve members under different combinations of loads in the future. Research concerning this topic could guide the design and material properties of light steel curve members exposed to high or low temperatures.

Likewise, the paper can suggest researching the fatigue behaviour of light steel curve members under different loading combinations. Identifying potential fatigue failure modes could assist in developing fatigue-resistant designs that can withstand prolonged exposure to cyclic loads. Some of the dynamic development of the continuous improvement of thin-walled energy-absorbing components are also suggested by Rogala et al. [64]. The same approach can be applied for design purposes.

7.4. For Parametric Design Aspect

Although Rhino 7 and Strand7 are robust applications for designing 3D models and analysing structural elements, their need for interoperability poses a significant challenge. Several challenges have been identified during our research, including maintaining a consistent orientation of local beam axes between Rhino 7 and Strand7. If this consistency cannot be achieved, the adjusted beams could have incongruent beam orientations and be subjected to hindered wind effects, compromising their accuracy as a result of structural analysis. Therefore, a method for maintaining local beam axis orientation is imperative for obtaining reliable and accurate structural analysis results.

Improvement in the form-finding method can significantly impact the automation of the digital modelling process. A script employing a form-finding algorithm was proposed to

optimise light steel curve members using Rhino 7 Grasshopper and Strand7. Implementing the suggested approach will make the modelling process more efficient, accurate and require less manual adjustment.

As a result, this method is capable of varying the size and shape of elements used in FEA simulations, improving accuracy and efficiency. In this way, researchers can identify optimal conditions for accurate and efficient simulations by testing different shapes and sizes of elements.

A further suggestion would be to evaluate the feasibility of integrating FEA simulations with experimental testing to improve the accuracy and reliability of the curve member design for light steel. Combining simulation and testing would enable the validation of simulation accuracy and design optimisation necessary to achieve optimal performance and safety. By employing this approach, one can gain valuable insight into the design and engineering industry, which in turn can result in more efficient and practical designs.

In the analysis of simulation data for light steel curve members, machine learning and artificial intelligence techniques can be highly beneficial. This advanced technology enables the examination of extensive collections of simulation data and the identification of patterns or trends that may not be quickly apparent through traditional methods. By conducting this investigation, we will gain new insights and discoveries regarding the behaviour of light steel curve members in different load combinations, allowing us to develop simulation methods that are more efficient and effective.

Machine learning and artificial intelligence can be applied to simulation data analysis to develop more accurate and reliable structural designs. With these advanced techniques, researchers can identify potential design weaknesses and enhance performance, resulting in improved safety and the overall effectiveness of the invention.

In summary, when applied to simulation data analysis, machine learning, and artificial intelligence are poised to revolutionise the design and engineering industry. These techniques can significantly enhance light steel curve member design by unlocking new insights and providing a basis for more accurate, reliable, and efficient design decisions.

For Building Information Modelling Aspect

Another potential improvement area is the investigation of construction design and management techniques. Integrating the proposed method with BIM workflows makes it possible to output technical drawings from Rhino 7 Grasshopper, streamlining the construction process and facilitating accurate fabrication of curved structural members and crucial joints on site. Additionally, the parametric information of the digital model can be reinterpreted to provide construction management instructions, enabling more efficient and effective construction management.

By exploring these possibilities, the construction process is likely to be enhanced in efficiency and accuracy, reducing errors and delays and enhancing the finished structure's safety and reliability. Incorporating digital technologies into construction management has already demonstrated promising results in reducing construction costs, schedules, and resource requirements. Therefore, the proposed method has the potential to revolutionise the construction industry, paving the way for more innovative and advanced building design methods.

Author Contributions: Conceptualization, F.T., S.J., S.S., L.M. and S.M.E.S.; Methodology, F.T., S.J., S.S., L.M. and S.M.E.S.; Software, F.T., S.J. and L.M.; Validation, F.T., S.J., S.S., L.M. and S.M.E.S.; Formal analysis, F.T., S.J. and L.M.; Investigation, F.T., S.J., S.S., L.M. and S.M.E.S.; Resources, F.T. and S.M.E.S.; Data curation, F.T. and S.M.E.S.; Writing—original draft, F.T., S.J. and L.M.; Writing—review & editing, F.T. and S.M.E.S.; Supervision, F.T. and S.M.E.S.; Project administration, S.M.E.S. All authors have read and agreed to the published version of the manuscript.

Funding: This research received no external funding.

Data Availability Statement: Not applicable.

Conflicts of Interest: The authors declare no conflict of interest.

References

1. Tahmasebinia, F.; Wang, Y.; Wu, S.; Ho, J.; Shen, W.; Ma, H.; Sepasgozar, S.M.E.; Marroquin, F.A. Advanced Structural Analysis of Innovative Steel–Glass Structures with Respect to the Architectural Design. *Buildings* **2021**, *11*, 208. [[CrossRef](#)]
2. King, C.; Brown, D. *Design of Curved Steel*; The Steel Construction Institute: Ascot, UK, 2001; p. 281.
3. Dowswell, B. *Curved Member Design*; American Institute of Steel Construction: Chicago, IL, USA, 2018.
4. Kido, E.M.; Cywinski, Z.; Kawaguchi, H. Tradition and modernity in the structural art of steel-glass structures in Japan. *Steel Constr.-Des. Res.* **2021**, *14*, 55–63. [[CrossRef](#)]
5. Kido, E.M.; Cywinski, Z. The steel-glass art of railway stations in Japan. *Stahlbau* **2018**, *87*, 611–621. [[CrossRef](#)]
6. Kido, E.M.; Cywinski, Z. The new steel-glass architecture of passenger service centres on expressways in Japan. *Steel Constr.-Des. Res.* **2015**, *8*, 210–215. [[CrossRef](#)]
7. Kido, E.M.; Cywin, Z. The new steel-glass architecture of air terminals in Japan. *Steel Constr.-Des. Res.* **2014**, *7*, 246-U150. [[CrossRef](#)]
8. Kido, E.M.; Cywinski, Z. The new steel-glass architecture of buildings in Japan. *Steel Constr.-Des. Res.* **2013**, *6*, 229–237. [[CrossRef](#)]
9. Kido, E.M.; Cywinski, Z. Aesthetic perception of steel-glass architecture in Japan. *Stahlbau* **2017**, *86*, 515–526. [[CrossRef](#)]
10. Helbig, T.; Oppe, M. Roofs and facades of United States Institute of Peace, Washington D.C. Free-form steel-glass grid-shell symbolizing a white dove of peace in flight. *Steel Constr.-Des. Res.* **2012**, *5*, 232–237. [[CrossRef](#)]
11. Hess, R. Material glass. *Struct. Eng. Int. J. Int. Assoc. Bridge Struct. Eng. IABSE* **2004**, *14*, 76–79. [[CrossRef](#)]
12. Pariafsai, F. A review of design considerations in glass buildings. *Front. Archit. Res.* **2016**, *5*, 171–193. [[CrossRef](#)]
13. Hoffmeister, B.; Di Biase, P.; Richter, C.; Feldmann, M. Innovative steel-glass components for high-performance building skins: Testing of full-scale prototypes. *Glas. Struct. Eng.* **2016**, *2*, 57–78. [[CrossRef](#)]
14. Segura, C.C.; Feldmann, M. Characterisation of the Dynamic Behaviour of Laminated Sheet Glass in Steel-Glass Facades. In Proceedings of the 10th Biennial International Conference on Vibration Problems (ICOVP), Prague, Czech Republic, 5–8 September 2011; Springer: Berlin, Germany, 2011.
15. Netušil, M.; Eliasova, M. Structural Design of Composite Steel-Glass Elements. In Proceedings of the 3rd Conference on Architectural and Structural Applications of Glass—Challenging Glass, Delft, The Netherlands, 28–29 June 2012.
16. Abeln, B.; Preckwinkel, E.; Yandzio, E.; Heywood, M.; Eliášová, M.; Netušil, M.; Grenier, C. *Development of Innovative Steel-Glass Structures in Respect to Structural and Architectural Design (Innoglast)*; Publications Office of the European Union: Luxembourg, 2013.
17. Rao, N.V.; Rajasekhar, M.; Vijayalakshmi, K.; Vamshykrishna, M. The Future of Civil Engineering with the Influence and Impact of Nanotechnology on Properties of Materials. In Proceedings of the 2nd international Conference on Nanomaterials and Technologies, Hyderabad, India, 17–18 October 2014; Elsevier Science Bv: Mumbai, India, 2014.
18. Netušil, M.; Eliasova, M. Design and evaluation of bonded composite glass beams. *Proc. Inst. Civ. Eng. -Struct. Build.* **2015**, *168*, 490–499. [[CrossRef](#)]
19. Pravdova, I.; Eliasova, M. Influence of An Intial Imperfection on the Lateral And Torsional Buckling of A Hybrid Beam. In Proceedings of the 23rd International Conference on Engineering Mechanics, Svatka, Czech Republic, 15–18 May 2017; Acad Sci Czech Republic, Inst Thermomechanics: Svatka, Czech Republic, 2017.
20. Kruijs, R. Designing a Glass Bearing Connection with a Probability to EN1990 CC2. In Proceedings of the 3rd Conference on Architectural and Structural Applications of Glass—Challenging Glass, Delft, The Netherlands, 28–29 June 2012; Ios Press: Amsterdam, The Netherlands, 2012.
21. Nhamoinesu, S.; Overend, M. The Mechanical Performance of Adhesives for a Steel-Glass Composite Facade System. In Proceedings of the 3rd Conference on Architectural and Structural Applications of Glass—Challenging Glass, Delft, The Netherlands, 28–29 June 2012; Delft Univ Technol, Ios Press: Amsterdam, The Netherlands, 2012.
22. Richter, C.; Abeln, B.; Geßler, A.; Feldmann, M. Structural steel–glass facade panels with multi-side bonding—Nonlinear stress–strain behaviour under complex loading situations. *Int. J. Adhes. Adhes.* **2014**, *55*, 18–28. [[CrossRef](#)]
23. Richter, C.; Abeln, B.; Geßler, A.; Feldmann, M. The Use of Structural Adhesives for Steel–Glass Facade Panels With Multi-Axial Stress–Strain Behavior—Experimental and Numerical Investigations. *Durab. Build. Constr. Sealants Adhes.* **2015**, *5*, 1–27.
24. Muzalev, V.N.; Semukhin, B.S.; Danilov, V.I. The Structure and Mechanical Properties of Bridge Steel Weldings With Glass-Steel Liners. In Proceedings of the International Scientific and Practical Conference on Urgent Problems of Modern Mechanical Engineering, Yurga, Russia, 17–18 December 2015; Natl Res Tomsk Polytechn Univ, Yurga Inst Technol, Iop Publishing Ltd.: Bristol, UK, 2015.
25. Tutunchi, A.; Kamali, R.; Kianvash, A. Effect of Al₂O₃ nanoparticles on the steel-glass/epoxy composite joint bonded by a two-component structural acrylic adhesive. *Soft Mater.* **2015**, *14*, 1–8. [[CrossRef](#)]
26. Tutunchi, A.; Kamali, R.; Kianvash, A. Adhesive strength of steel–epoxy composite joints bonded with structural acrylic adhesives filled with silica nanoparticles. *J. Adhes. Sci. Technol.* **2014**, *29*, 195–206. [[CrossRef](#)]
27. Van Lancker, B.; De Corte, W.; Belis, J. Durability of linear adhesive cold-formed steel-glass connections. In Proceedings of the 3rd International Conference On Structures And Architecture (ICSA), Guimaraes, Portugal, 27–29 July 2016; CRC Press-Balkema: Boca Raton, FL, USA, 2016.
28. Odenbreit, C.; Dias, V. Investigation of hybrid steel-glass beams with adhesive silicone shear connection. *Steel Constr. -Des. Res.* **2016**, *9*, 207–221.

29. Ligaj, B.; Wirwicki, M.; Karolewska, K.; Jasińska, A. Experimental studies of glued Aluminum-glass joints. In Proceedings of the 3rd International Conference on Science, Technology, and Interdisciplinary Research (IC-STAR), Bandar Lampung, Indonesia, 18–20 September 2017; Iop Publishing Ltd.: Bristol, UK, 2017.
30. Chavooshian, M.; Kamali, R.; Tutunchi, A.; Kianvash, A. Effect of silicon carbide nanoparticles on the adhesion strength of steel-epoxy composite joints bonded with acrylic adhesives. *J. Adhes. Sci. Technol.* **2017**, *31*, 345–357. [[CrossRef](#)]
31. Wang, Z.-Y.; Shi, Y.; Wu, Y.; Wang, Q.; Luo, S. Shear behaviour of structural silicone adhesively bonded steel-glass orthogonal lap joints. *J. Adhes. Sci. Technol.* **2018**, *32*, 2693–2708. [[CrossRef](#)]
32. Amstutz, C.; Burgi, M.; Jousset, P. Characterisation and FE simulation of polyurethane elastic bonded joints under multiaxial loading conditions. *Int. J. Adhes. Adhes.* **2018**, *83*, 103–115. [[CrossRef](#)]
33. Katsivalis, I.; Thomsen, O.T.; Feih, S.; Achintha, M. Failure prediction and optimal selection of adhesives for glass/steel adhesive joints. *Eng. Struct.* **2019**, *201*, 109646. [[CrossRef](#)]
34. Biolzi, L.; Morelli, F.; Panzera, I.; Salvatore, W. Silicone bonded steel-glass joints under high temperature. *Int. J. Adhes. Adhes.* **2021**, *108*, 18. [[CrossRef](#)]
35. Adriaenssens, S.; Ney, L.; Bodarwe, E.; Williams, C. Finding the Form of an Irregular Meshed Steel and Glass Shell Based on Construction Constraints. *J. Arch. Eng.* **2012**, *18*, 206–213. [[CrossRef](#)]
36. Dias, V.; Odenbreit, C.; Hechler, O.; Scholzen, F.; Ben Zineb, T. Development of a constitutive hyperelastic material law for numerical simulations of adhesive steel-glass connections using structural silicone. *Int. J. Adhes. Adhes.* **2014**, *48*, 194–209. [[CrossRef](#)]
37. Espinha, M.; Greiner, H.; Ziegler, R. Gateway to Baku—The steel and glass building envelope of the new airport terminal in Azerbaijan. *Stahlbau* **2015**, *84*, 374–379. [[CrossRef](#)]
38. Pravdova, I.; Eliasova, M. Lateral and torsional stability of hybrid steel-glass beams. In Proceedings of the 3rd International Conference On Structures And Architecture (ICSA), Guimaraes, Portugal, 27–29 July 2016; CRC Press-Balkema: Boca Raton, FL, USA, 2016.
39. Wang, Z.-Y.; Shi, Y.; Wang, Q.-Y.; Wu, Y.; He, M. In-plane shear compression behaviour of steel-glass composite beams with laminated glass webs. *Eng. Struct.* **2017**, *150*, 892–904. [[CrossRef](#)]
40. Adriaenssens, S. Mike Barnes’s legacy: The emergence of form finding and analysis approaches for bending active and elastic gridshell structures. In Proceedings of the 60th Anniversary Symposium of the International-Association-for-Shell-and-Spatial-Structures (IASS SYMPOSIUM)/9th International Conference on Textile Composites and Inflatable Structures (STRUCTURAL MEMBRANES), Barcelona, Spain, 7–10 October 2019.
41. Eliasova, M.; Pravdova, I. Lateral torsional buckling of hybrid steel-glass beams. In *International Colloquia on Stability and Ductility of Steel Structures (SDSS)*; Czech Tech Univ Prague, Routledge: Prague, Czech Republic, 2019.
42. Firmo, F.; Jordão, S.; Neves, L.C.; Bedon, C. Exploratory study on simple hybrid or pre-stressed steel-glass I-beams under short-term bending – Part 1: Experiments. *Compos. Struct.* **2020**, *234*, 16. [[CrossRef](#)]
43. Scoccia, C.; Carbonari, L.; Palmieri, G.; Callegari, M.; Rossi, M.; Munafó, P.; Marchione, F.; Chiappini, G. Design of a Tensegrity Servo-Actuated Structure for Civil Applications. *J. Mech. Des.* **2022**, *144*, 10. [[CrossRef](#)]
44. Marchione, F.; Chiappini, G.; Rossi, M.; Scoccia, C.; Munafó, P. Experimental assessment of the static mechanical behaviour of the steel-glass adhesive joint on a 1:2 scale tensegrity floor prototype. *J. Build. Eng.* **2022**, *53*, 19. [[CrossRef](#)]
45. Knippers, J.; Riederer, J.; Oppe, M. Lincoln Center Canopies-Performance in Glass. In Proceedings of the 3rd Conference on Architectural and Structural Applications of Glass-Challenging Glass, Delft, The Netherlands, 28–29 June 2012; Delft Univ Technol, Ios Press: Amsterdam, The Netherlands, 2012.
46. Silvestru, V.A.; Zellinger, M.; Enghardt, O. Hybrid glass structures for building skins-actions and requirements. In Proceedings of the Cost Action TU0905 Mid-Term Conference on Structural Glass, Porec, Croatia, 18–19 April 2013; CRC Press-Taylor & Francis Group: Boca Raton, FL, USA, 2013.
47. Helbig, T.; Giampellegrini, L.; Oppe, M. “Carioca Wave”—A free-form steel-and-glass canopy in Rio de Janeiro, Brazil. *Steel Constr. -Des. Res.* **2014**, *7*, 252–257. [[CrossRef](#)]
48. de Falco, A.; Froli, M.; Giresini, L.; Puppino, M.L.; Sassu, M. A proposal for the consolidation of a r.c. social housing by means of external hybrid steel-glass frameworks. In Proceedings of the 3rd International Conference on Civil, Architectural and Hydraulic Engineering (ICCAHE), Hangzhou, China, 30–31 July 2014; Trans Tech Publications Ltd.: Bäch, Switzerland, 2014.
49. Heinze, L.; Baitinger, M.; Wolkowicz, C. Calculation of spheric bended insulated glazing units for the Kazakhstan-pavilion, Expo 2017. *Stahlbau* **2016**, *85*, 75–86. [[CrossRef](#)]
50. Maier, M.; Fischer, M.; Pietro, M. Extension of the Central Refectory of the University of Kassel. *Stahlbau* **2018**, *87*, 9.
51. Mahl, F.; Hartl, G.; Kloft, H. The capricorn bridge at Dusseldorf Medienhafen. *Stahlbau* **2022**, *91*, 39–48. [[CrossRef](#)]
52. Poorbiazar, S.; Naeff, A.; Kusch, O.; Luenser, K. Atrium roof and steel spiral stairs at the scientific building D-BSSE of ETH Zurich in Basel. *Stahlbau* **2021**, *90*, 741–+. [[CrossRef](#)]
53. Adriaenssens, S. How and Why Laurent Ney Finds Steel Structural Forms. *J. Int. Assoc. Shell Spat. Struct.* **2020**, *61*, 39–49. [[CrossRef](#)]
54. Nazar, K.; Slyk, J. Algorithmically aided management of structure modularity at the design and execution stage. *Arch. Civ. Eng.* **2021**, *67*, 643–657.
55. Schmid, F.; Eisert, P.; Feldmann, I. Situation-based use of extended reality technologies for steel-glass structures—A report from the DigitalTWIN research project. *Stahlbau* **2022**, *91*, 385–396. [[CrossRef](#)]

56. Han, S. Moynihan Train Hall/SOM. 2021. Available online: <https://www.archdaily.com/954941/moynihan-train-hall-som> (accessed on 15 February 2023).
57. Moynihan Train Hall. Available online: <https://www.sbp.de/en/project/moynihan-train-hall/> (accessed on 15 February 2023).
58. Chadstone Shopping Centre/CallisonRTKL + The Buchan Group. 2017. Available online: <https://www.archdaily.com/804275/chadstone-shopping-centre-callisonrtkl-plus-the-buchan-group> (accessed on 20 February 2023).
59. Chadwick, A.; Matthews, C.; Villafane, M.E.; Williams, C.J.K. PLATO—Gridshell Design Method for Chadstone Shopping Mall Roof. *IABSE Symp. Rep.* **2017**, *108*, 159–160.
60. AS/NZS 1170.1:2002; Standards Australia International, (Including Amendments Nos.1 and 2). Structural Design Actions. Part 1: Permanent, Im-posed and Other Actions. Standards Australia: Sydney, Australia, 2009.
61. AS/NZS 1170.2:2011; Standards Australia International, (Including Amendments Nos.1 and 2). Structural Design Actions. Part 2: Wind Actions. Standards Australia: Sydney, Australia, 2012.
62. The European Committee for Standardisation. The European Committee for Standardisation, Eurocode 1: Actions on Structures—Part 1–4: General Actions—Wind Actions. The European Committee for Standardisation: Brussels, Belgium, 2005.
63. AS/NZS 1170.0:2002; Standards Australia International, (Including Amendments Nos.1,2,4 and 5). Structural Design Actions. Part 0: General Principles. Standards Australia: Sydney, Australia, 2011.
64. Rogala, M.; Gajewski, J.; Gawdzińska, K. Crashworthiness analysis of thin-walled aluminium columns filled with aluminium–silicon carbide composite foam. *Compos. Struct.* **2022**, *229*, 116102. [[CrossRef](#)]

Disclaimer/Publisher’s Note: The statements, opinions and data contained in all publications are solely those of the individual author(s) and contributor(s) and not of MDPI and/or the editor(s). MDPI and/or the editor(s) disclaim responsibility for any injury to people or property resulting from any ideas, methods, instructions or products referred to in the content.